# Track Impact Parameter Resolution in the *BABAR* Detector

by

David J. Asgeirsson

B.Sc., Simon Fraser University, 1998

A THESIS SUBMITTED IN PARTIAL FULFILMENT OF
THE REQUIREMENTS FOR THE DEGREE OF

MASTER OF SCIENCE

in

The Faculty of Graduate Studies

(Physics)

THE UNIVERSITY OF BRITISH COLUMBIA

April 21, 2005

# Abstract

This thesis contains a study of track impact parameter resolution in the *BABAR* detector using lepton pair events from $e^+e^- \to l^+l^-(\gamma)$ and from $\gamma^*\gamma^* \to l^+l^-$ where $l$ is either $e$ or $\mu$. The high number of these events in the data set and Monte Carlo simulations allows the tails of the resolution to be studied in detail. The Gaussian core of the resolution is consistent within 20% with the track-by-track errors returned by the track fitting software for both data and Monte-Carlo simulations. Beyond about three standard deviations ($\sigma$) the non-Gaussian tail approximately obeys power laws. A simple parametrization is presented which fits the data well to beyond $10\sigma$. The tail shape is consistent with that expected from a large-angle Coulomb scattering Toy Monte-Carlo. The GEANT4-based *BABAR* Monte Carlo software reproduces the core out to approximately $2\sigma$ but the behaviour of the tails further out disagrees with the data and the predictions of Moliere theory.

# Contents

# List of Tables

# List of Figures

# Acknowledgements

I would first like to thank my supervisor, Thomas Mattison, whose guidance and support made this research possible. I look forward to continuing to work with him in the future.

I would also like to thank all of the other members of the *BABAR* group at UBC, Janis, Chris, Neil, Nasim, Song, Bryan and Doug. Thanks to all of you for your comments and advice during the past two years. Special thanks to Doug Maas for supporting the computing resources that were essential for this work.

Finally, I want to thank Elissa for all of her love and support. This work would have been so much more difficult without you.

# Chapter 1

# Introduction

## 1.1 CP violation in the Standard Model

The primary motivation of the *BABAR* Experiment is the measurement of CP-violation phenomena in $B$-mesons - mesons containing at least one $b$ (bottom or beauty) quark [1]. CP is a quantum-mechanical operator, corresponding to changing the sign of the charge, and applying the 3-dimensional parity or mirror-reversal operator. We know that if a symmetry is respected in nature, there must be a corresponding quantity which is conserved; a result proved by Emmy Noether in 1918 [2]. It was believed that both C and P should be good symmetries of nature, until Madame Wu [3] observed parity violation in 1957. After this discovery, it was seen that the nuclear weak force is maximally parity violating, or that parity is never conserved in a purely weak interaction. The subsequently developed V-A theory of the weak interaction restored CP as a good (unbroken) symmetry, but CP-violation was observed experimentally at a level of 2 parts in 1000 in Kaon decay by Cronin and Fitch in 1964 [4]. Since that time, CP-violation has been one of the most heavily studied topics in particle physics, particularly due to Sakharov's realization that it is a necessary ingredient in any explanation of the matter-antimatter asymmetry of the universe [5].

It was later shown by the theorists Kobayashi and Moskawa that CP violation is allowed in the Standard Model of particle physics if there are at least three generations of quarks that are mixed through the weak interaction [6]. If there are exactly three generations of quarks, then this weak mixing between quark flavours can be described mathematically by a 3x3 matrix normally written as:

$$V = \begin{pmatrix} V_{ud} & V_{us} & V_{ub} \\ V_{cd} & V_{cs} & V_{cb} \\ V_{td} & V_{ts} & V_{tb} \end{pmatrix} \tag{1.1}$$

where the subscripts $u$, $d$, $s$, $c$, $t$, $b$ stand for the "up", "down", "strange", "charm", "top" and "bottom" species of quarks, respectively. In principle each element of the so-called CKM (Cabibbo, Kobayashi, Moskawa) matrix can be complex, but the matrix must be unitary if there are only three generations of quarks in nature. Requiring $V$ to be unitary reduces the number of free parameters from 18 (9 real and 9 imaginary numbers) to 9 real and imaginary numbers. With six flavours of quarks in the Standard Model, there are five relative phases between the wavefunctions of the quarks. These five phases reduce the number of free parameters in $V$ from 9 to 4. A 3x3 matrix containing

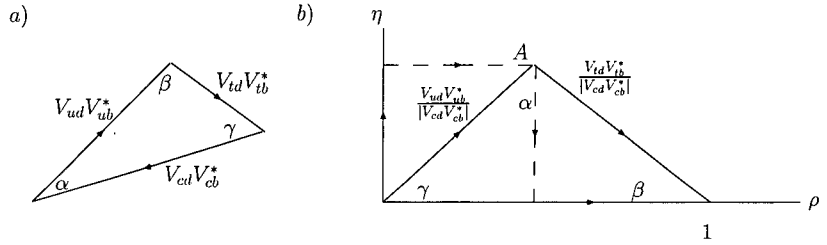


Figure 1.1: Unitarity triangles constructed from the CKM matrix in a) standard quark-mixing parameters and b) Wolfenstein parameterization.

four parameters can always be written as the product of three rotations plus a phase. It is this imaginary phase that is responsible for the phenomena of CP-violation.

The parameterization of Wolfenstein [7], which is based on experimental measurements, is frequently used when discussing the latest results of tests on the unitarity of the CKM matrix. His parametrization is given by:

$$V = \begin{pmatrix} 1-\lambda^2/2 & \lambda & \lambda^3 A(\rho - i\eta) \\ -\lambda & 1-\lambda^2/2 & \lambda^2 A \\ \lambda^3 A(1-\rho-i\eta) & -\lambda^2 A & 1 \end{pmatrix} \tag{1.2}$$

where $\lambda$ is the Cabibbo angle and $A$, $\rho$ and $\eta$ may be experimentally measured. In this parameterization, all experimentally observed CP-violation is related to the imaginary phase $\eta$ in the bottom-left and top-right elements. It is also clear that as written, this form of the CKM matrix is not unitary at the level of $\lambda^4$, but it still provides a convenient method of comparison for experimental results.

By measuring whether or not the CKM matrix is truly unitary, we can test for new particles beyond the three generations of quarks thus far observed, or physics beyond the laws of the ElectroWeak interaction. One convenient way of testing unitarity is by multiplying one column by a row of the conjugate matrix to obtain an equation with 6 elements:

$$V_{ud}V_{ub}^* + V_{cd}V_{cb}^* + V_{td}V_{tb}^* = 0 \tag{1.3}$$

which can also be interpreted as the requirement that the sum of three complex quantities vanishes. This can be represented in the Argand plane as the so-called Unitarity Triangle, shown in Figure 1.1a. If the three sides are divided by $V_{cd}V_{cb}^*$, the triangle can also be expressed in terms of the Wolfenstein parameters, as shown in Figure 1.1b.

## 1.2 $B^0 - \overline{B^0}$ Mixing and the CKM Matrix

In any system in which the mass(energy) eigenstates are not identical to the flavour eigenstates of the particles, mixing between the different flavour states

will occur. For example, the kaons $K_s$ and $K_L$ are mass eigenstates, while the $K^0$ and $\overline{K^0}$ are flavour eigenstates. In the case of the neutral $B$ mesons, the mass eigenstates are not the same as the flavour eigenstates so the $B^0$ and $\overline{B^0}$ also mix quantum mechanically. Unlike the kaon system, however, the mass difference is large and the lifetime difference is negligible. The oscillation amplitude, $A(t)$, has the same time-dependence in any two-level system:

$$A(t) \propto \cos(\Delta m\ t) \tag{1.4}$$

where $\Delta m$ is the mass difference between the two flavour eigenstates.

The mixing parameter for the $B_d$ mesons (consisting of a $b$ and $d$ quark-antiquark pair) is then $\Delta m_d$. In the absence of CP-violation in mixing, the mass difference $\Delta m_d = 2|M_{12}|$ where $M_{12}$ is the off-diagonal matrix element of the mass and decay matrix for the neutral $B$ system. This matrix element is directly related to the CKM matrix elements $V_{td}$ and $V_{tb}$ by the following equation:

$$M_{12} = \frac{G_F^2 m_W^2 \eta_B m_{B_d} f_{B_d}^2 B_{B_d}}{12\pi^2} S_0(m_t^2/m_W^2)(V_{td}^* V_{tb})^2 \tag{1.5}$$

where $G_F$ is the Fermi constant of the weak interaction, $m_W$ is the W boson mass, $m_{B_d}$, $f_{B_d}$ and $B_{B_d}$ are the mass, weak decay constant and QCD bag parameter of the $B_d$ meson. The QCD bag parameter is proportional to the ratio between the nonperturbative coupling of the neutral $B$-mesons and the weak decay constant, and it is calculated using lattice QCD. The function $S_0(x_t)$ can be approximated quite well by $0.784 x_t^{0.76}$. For more details on this relation, please consult references [8] or [9].

By carefully measuring the time-dependent distribution of neutral $B$ decays, physicists can determine these values of $\Delta m$ and $M_{12}$ and thereby test the CKM matrix and the Standard Model.

## 1.3 Measuring CP Violation in $B$ decays

The *BABAR* experiment is using the physics of $B$-decays and $D$-decays to measure the angles $\alpha$, $\beta$ and $\gamma$ of the Unitarity Triangle. More details on the physics objectives of the *BABAR* experiment are given in reference [1].

The cleanest possible process for producing pairs of $B$ mesons is to collide electron-positron pairs at the right energy to produce the $\Upsilon(4s)$ meson. The $\Upsilon(4s)$ decays into a pair of $B$ mesons, either $B^0$,$\overline{B^0}$, or $B^+$,$B^-$. In the *BABAR* experiment electrons and positrons are annihilated to produce the $\Upsilon(4s)$ meson, which decays almost instantly into a pair of $B$-mesons. The two $B$ mesons are very nearly at rest in the centre-of-mass frame of the $\Upsilon(4s)$. If the beam energies were symmetric, and the $\Upsilon(4s)$ was at rest in the lab frame, time-dependent analyses would not be feasible because the $B$ lifetime is too short, approximately $10^{-12}$ seconds. At PEP-II, however, electrons are accelerated to an energy of 9 GeV, and positrons are accelerated to an energy of 3.1 GeV,

before they collide. The collision creates a system with a CM (centre-of-mass) energy of $\sqrt{s} = 10.58$ GeV, corresponding to the mass of the $\Upsilon(4s)$ meson, and a Lorentz boost in the lab frame of $\beta\gamma = 0.58$ because of the asymmetric beam energies. This means that the $\Upsilon(4s)$ is moving along the beam axis, in the direction of the $e^-$ beam, with a velocity of roughly one-half the speed of light.

This Lorentz boost converts timescales of order $10^{-12}$ seconds into distances on the order of $10^{-4}$ metres, or roughly 100 $\mu$m. Clearly, excellent position resolution along the beam axis of the detector is crucial to any time-dependent analysis. Furthermore, knowledge of this resolution often constitutes one of the dominant sources of systematic uncertainty in time-dependent *BABAR* results.

The cleanest measurement of CP violation in $B$ decays is the measurement of interference between direct and mixed decays to CP eigenstates. As an example, consider the neutral $B$ decay to $J/\psi K_s$, where the decay can proceed through two channels, either $B^0 \to J/\psi K_s$, or $\overline{B^0} \to J/\psi K_s$. The initial state of the $B$ can be "tagged" by identifying the flavour of the other $B$ meson. By looking for a decay to a non CP-eigenstate, for example $B \to Dl\nu$, the flavour of the products, (or charge of the primary lepton) can be used to identify the parent $B$ as either a $B^0$ or $\overline{B^0}$. The time-independent asymmetry between the two channels (direct and mixed) vanishes because the "tag" $B$ meson will decay before the signal $B$ roughly half the time. If the tag is before the signal, the sign of the asymmetry switches, and the time-integrated asymmetry will cancel to zero. If, however, the decay vertices of the $B$'s are reconstructed, then the time-dependent asymmetry can be measured, and CP violation can be observed. In this way, knowledge of the position resolution of the *BABAR* detector is crucial for precise measurements of CP violation in $B$ decays.

The BELLE experiment [10], which is nearly identical to *BABAR* provides an important source of competition as well as an important check for the consistency of physics quantities which are being measured for the first time in these $B$-factory experiments.

## 1.4 Motivation for Track Impact Parameter Resolution Study

Track impact parameter measurement is central to studies of both CP violation and neutral $B$ mixing. Both are dependent on fitting to a time-dependent asymmetry, where the times have been determined by the difference in position along the beam direction between the particle tracks or the vertices formed by the particle tracks. The fit to an asymmetry includes models of the track impact parameter resolution. The resolution model parameters are in turn determined by the application of the model to "control samples", where the physics is known. For example, the track resolution in the *BABAR* dilepton $B$-mixing analysis is taken from a fit to the track impact parameter difference in $J/\psi \to l^+l^-$ decays, where both tracks must come from a single point in space [11]. These events provide a relatively small sample for fitting, concentrating only on the central

part of the distribution.

Finite resolution moves events from the true $\Delta t$ between the $B$ decay times to a different $\Delta t$ value. This increases the statistical error in the measurements. If the measurements are not compensated for the resolution it can also introduce systematic shifts in the results. Typically, the fits are repeated with several different models for the resolution, and the difference between them is taken as the systematic error.

The tails of the resolution can be particularly difficult to deal with. Events with large reconstructed $\Delta t$ values are very important for CP, mixing and lifetime measurements, but a significant fraction of such events are actually events with small values of $\Delta t$ and large systematic errors.

The goal of this thesis is to measure the track impact parameter resolution. A high-statistics control sample of *BABAR* data events is selected. A parametrization of the resolution is developed that works well out into the tails of the distribution. The resolution is comparable between data and the fully reconstructed *BABAR* Monte-Carlo simulations. The theory of Multiple Coulomb Scattering, its effects on track impact parameter resolution, and a corresponding resolution model are developed in Chapter 2. The physics processes responsible for creation of the lepton-pair events selected for this analysis are explained in Chapter 3. The *BABAR* detector is described in Chapter 4. The *BABAR* data-acquisition electronics and software are described in Chapter 5. The process through which our control sample is selected from all of the *BABAR* data is documented in Chapter 6. The analysis of the track impact parameter resolution for this control sample is detailed in Chapter 7. Finally, a summary of the findings of this thesis is presented in Chapter 8.

# Chapter 2

# Multiple Coulomb Scattering

## 2.1 Theory of Multiple Coulomb Scattering

Coulomb scattering is the scattering of a charged particle by an atomic nucleus through the electrostatic force, or in the language of quantum field theory, through the exchange of a virtual photon. Scattering from an exponentially-screened Coulomb potential is given by the screened Rutherford cross-section:

$$\frac{d\sigma}{d\Omega} = 2\pi \left(\frac{2Zze^2}{pv}\right)^2 \frac{1}{(\sin^2(\theta) + \chi_\alpha^2)^2} \tag{2.1}$$

where $Z$ is the atomic number of the target material, $z$ is the charge in units of $e$ the electron charge, $p$ is the 3-momentum magnitude, and $v$ is the velocity magnitude of the incident particle. The parameter $\chi_\alpha$ is known as the screening angle. Equation 2.1 does not include the relativistic spin-dependence, but this effect is washed out after many small-angle scatters. After integrating over the azimuthal angle $\phi$, and making the small-angle approximation ($\sin(\theta) \simeq \theta$), we arrive at the following relation:

$$\frac{d\sigma}{d\theta} \propto \frac{\theta}{(\theta^2 + \chi_\alpha^2)^2} \propto \frac{1}{\theta^3} \tag{2.2}$$

in which we can clearly see that the cross-section is proportional to $\theta^{-3}$. By repeatedly applying the above cross-section, for each atomic layer, it is possible to calculate the distribution of final angles after an arbitrary path-length has been traversed. Williams [12], [13] was able to qualitatively describe the scattering distribution successfully with the sum of a central Gaussian and a single-scatter tail function. Several years later, Moliere [14] was able to give more exact analytical results, for a wide range of angles, although for practical applications this required the tabulation of numerical values. In the limit of small angles the resultant distribution for the angle of deviation $\theta$ can be described by three separate terms to better than 1% accuracy [15]. The first term is a Gaussian core. Simply using this Gaussian term alone is accurate to better than 1% when considering relatively modest angles, $\theta < 2\sigma$, and material thicknesses of more than 1000 atomic layers (which describes all practical experiments). The second term oscillates in the core and asymptotically approaches the Rutherford distribution at large angles. The third term is a higher-order correction.

The width of the central Gaussian peak scales roughly as the square-root of the thickness traversed, but there is an additional logarithmic dependence. The tabulated values calculated using the theory of Moliere have been fit to the following empirical relation:

$$\theta_0 = \frac{13.6 \text{ MeV}}{\beta cp} z\sqrt{x/X_0}\,[1 + 0.038\ln(x/X_0)] \tag{2.3}$$

in which $x$ is the thickness in terms of the radiation length of the material, $X_0$. The Particle Data Group [9] recommends the use of this formula as an approximation to the width of the central Gaussian of the Moliere distribution. As the angle $\theta$ increases, the distribution approaches that of the single scatter, i.e. $\propto \theta^{-3}$. The popular detector simulation software package, GEANT, used the Moliere formulation of Multiple Coulomb Scattering in Version 3 [16].

Version 4 of GEANT [17] is based on the theory of Lewis [18]. This theory is formulated in terms of the moments of the distributions rather than the distributions themselves. Approximate distributions are chosen which have the correct moments to within certain tolerances. This is identical in the core to the Moliere theory but is not necessarily the same in the far tails. The *BABAR* collaboration uses GEANT 4 for all detector simulations.

When simulating Multiple Coulomb Scattering (MCS), it is much more efficient to select the final angle from the complicated Moliere or Lewis distributions rather than to simulate single scatters millions or billions of times. Using the Moliere distribution directly to describe experimental data is rather awkward, but it is possible to create a parametrization that describes the distribution reasonably well out into the tails.

## 2.2 Monte-Carlo Generation of MCS Distribution

In order to generate a sample of events having the correct distribution, we repeatedly sample angles from a simple distribution. This is more time consuming than using the Moliere or Lewis distributions, but is certain to provide us with the correct distribution far out into the tails.

Figure 2.1 shows the distribution of scattering angles generated by a single throw of a random number following the simple $\theta^{-3}$ distribution, in the range $0.005 < \theta < \infty$. A second uniform random number $\cos(\phi)$, is selected from a flat distribution between -1 and 1. The original value of $\theta$ is then multiplied by $\cos(\phi)$ to give a displacement centered on zero. Twenty thousand of these individual displacements were then added together to give the final deflection for a single particle. The entire process was repeated for 100,000 particles and the resultant distribution is shown in Figure 2.2. The Gaussian core of Multiple Coulomb Scattering is clearly visible, along with the power-law tail corresponding to the original $\theta^{-3}$ distribution used. This simple "Toy" Monte-Carlo model can be employed later to compare to the track impact parameter resolution dis-

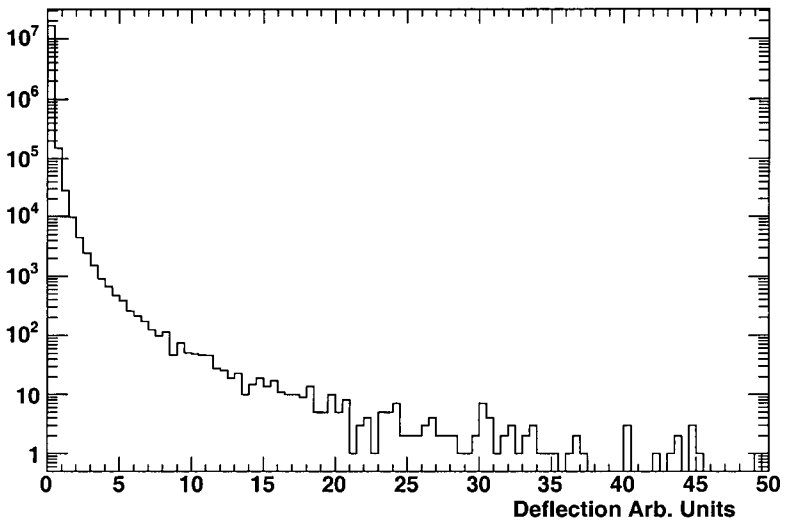


Figure 2.1: Angles generated from $\theta^{-3}$ distribution in the range $0.005 < \theta < \infty$.

tributions in the experimental and GEANT-simulated data, as well as to help choose an appropriate parameterization of the resolution distribution.

## 2.3 Parametrization of the Resolution Distribution

In order to help us determine the best lineshape for describing the track impact parameter resolution we look more closely at the power-law behaviour of the tails of the distribution. We know that the inner $2\sigma$ of the distribution is reasonably described by a Gaussian, and we will concentrate on the outer portions of the tail. Far enough out in the tails, the shape must asymptotically approach that of the Rutherford differential cross-section, a power-law of the form $\theta^{-3}$. The transition between the Gaussian core and the $\theta^{-3}$ power-law tail is usually described only approximately.

The resolution due to MCS can be accurately described by a Gaussian core and a tail function which eventually becomes a power-law tail at large deflections [15]. We will choose a tail which contains two separate power-laws. We construct a general formulation of this type of function using the following equation:

$$y(x) = N(1-f)G(x) + Nf\frac{T(x)}{A_T} \qquad (2.4)$$

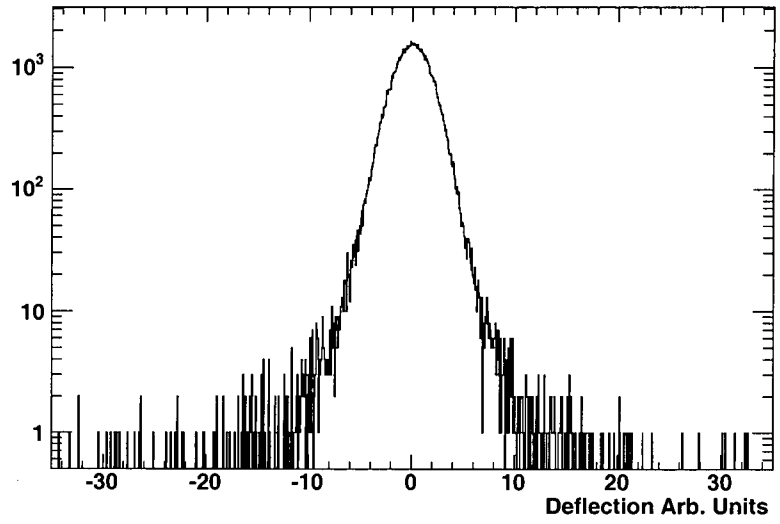


Figure 2.2: Distribution of final deflections caused by scattering 20,000 times according to the screened Rutherford cross-section.

$$G(x) = \frac{e^{\frac{-(x-\mu)^2}{2\sigma^2}}}{\sqrt{2\pi}\sigma} \tag{2.5}$$

$$T(x) = a^{-p_a} \qquad |x-\mu| \leq a\sigma \tag{2.6}$$

$$T(x) = \left(\frac{x-\mu}{\sigma}\right)^{-p_a} \qquad a\sigma < |x-\mu| < b\sigma \tag{2.7}$$

$$T(x) = \left(\frac{x-\mu}{\sigma b}\right)^{-p_b} \qquad |x-\mu| \geq b\sigma \tag{2.8}$$

$$A_T = 2\left((\sigma a)^{(1-p_a)} + \frac{b^{(1-p_a)} - a^{(1-p_a)}}{1-p_a}\right) + 2\left(b^{(p_b-p_a)}\frac{b^{(1-p_b)}}{1-p_b}\right) \tag{2.9}$$

where $N$ is the total number of events in the histogram, $G(x)$ is the Gaussian core, $T(x)$ is the tail function, $A_T$ is the area under the tail, and $f$ is the fraction of the total events under the tail function. The parameters for the Gaussian core $G(x)$ are the mean of the distribution $\mu$, and the width of the Gaussian $\sigma$. The parameters for the tail function $T(x)$ are: the inner breakpoint between the Gaussian core and the first power-law tail $a$, the power in the first power-law tail $p_a$, the outer breakpoint between the first power-law tail and the second $b$, and the power in the second power-law tail $p_b$.

Figure 2.3 is a plot of the function with the following values used to generate the plot, $N = 10^6$, $\mu = 0.0$, $\sigma = 1.0$, $a = 3.0$, $b = 5.0$, $p_a = 5.0$ and $p_b = 3.0$.

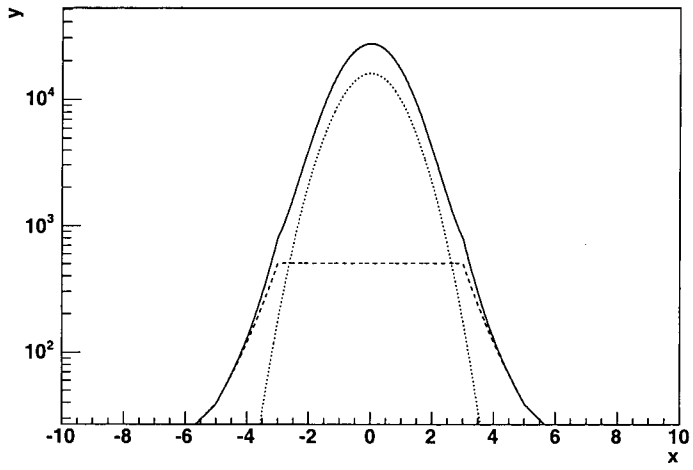


Figure 2.3: Plot of the function (Equation 2.4) used to describe the track vertex resolution in this study. The solid line is the function value, the dashed line is the tail function $T(x)$, and the dotted line is the Gaussian core $G(x)$.

The function is dominated by the Gaussian core (dotted line in the Figure) in the range -2< $x$ <2. We see that the tail function (dashed line in the Figure) is flat in the centre of the distribution, and falls off with two distinct power-laws to either side. We note the the function is not smooth at either of the breakpoints, and this can present practical difficulties in achieving convergence when this function is used for curve-fitting. These problems are resolved when two of the four parameters $a$, $b$, $p_a$ and $p_b$ are held fixed. We know that the MCS distribution must eventually vary as $\theta^{-3}$ so we can fix $p_b$=3. We found that fixing the two breakpoints $a$, and $b$ allowed the fitting algorithm to easily converge in all cases.

As a first test of the ability of Equation 2.4 to describe track impact parameter resolution distributions, we used it to fit the results of a Toy Monte-Carlo generated by the method described in Section 2.1. One hundred thousand events were generated with increasing numbers of scatters (N), ranging from N=2 up to N=20,000. All of the fits described in this section were performed with the two breakpoint parameters fixed at $a$ = 3.0 and $b$ = 5.0. These values were chosen based on the inspection of the tails described in the next section. The outer power-law was fixed at $p_b$ = 3.0, the same power-law dependence as the Rutherford differential cross-section. Figure 2.4 is a plot of the fit to the same distribution shown in Figure 2.1, with N=20,000. We observe reasonable agreement well out into the tails of the distribution. Figure 2.5 is a plot of the pulls of the same fit. The pulls are calculated by taking the difference between the

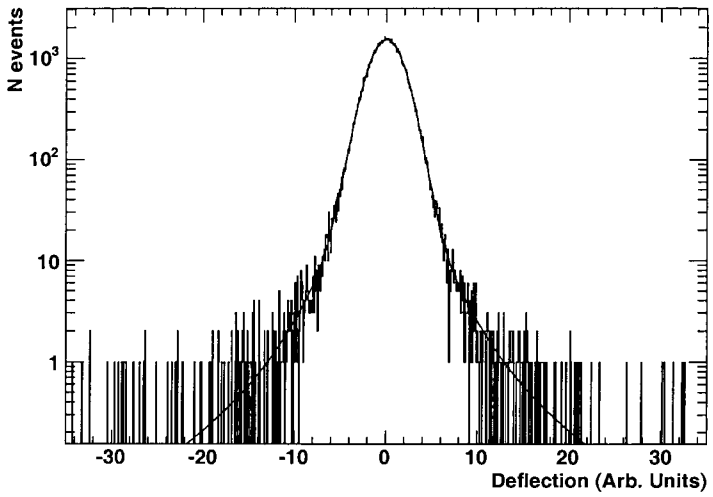


Figure 2.4: Plot of the Toy Monte Carlo distribution. The solid line is a fit to Equation 2.4.

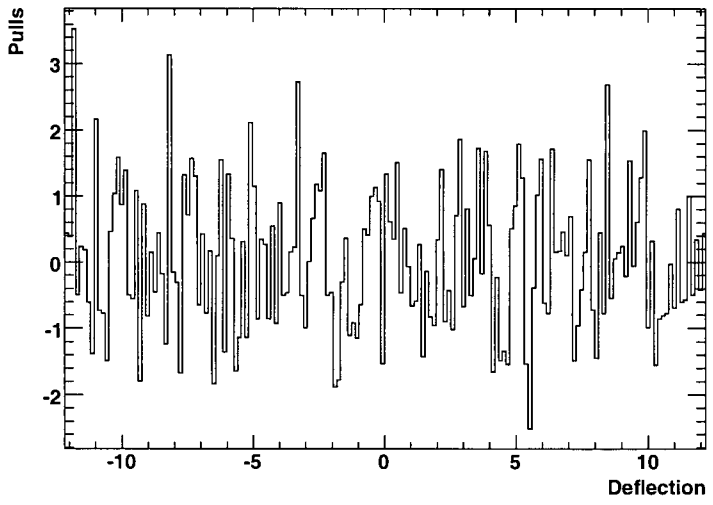


Figure 2.5: Plot of the pulls (data-fit / $\sqrt{data}$) for the fit in Figure 2.4.

actual and fitted values, and dividing by the expected statistical error of $\sqrt{n}$. We see that the data and fit function agree to within approximately 3 standard deviations over the range between -10 and +10. It is difficult, however, to verify that our fitted function accurately describes the data well into the tails by looking at a log-plot covering several orders of magnitude, such as Figure 2.4. The pulls could also contain subtle systematic variations in the tails.

## 2.4 A Closer Look at the Tails

To more closely examine the agreement in the tails of the distribution we can replot the data using a transformed variable, along with the suitably transformed fitting function.

We now consider the transformed variable $u = (x/\sigma)^{-2}$, where $x$ is the displacement generated by the method outlined above, and $\sigma$ is the width of the Gaussian core. If the distribution of $x$ follows the power-law $x^{-3}$ then $u$ will be flat. Any function transformed from $f(x)$ to $f(u)$ will be multiplied by a Jacobian factor of $u^{-3/2}/2$. We know that as $x$ goes to infinity the power-law goes to -3. This means that $u$ will be flat as it approaches zero. Figure 2.6 shows a histogram of $u$ when $x$ has been generated according to the method described in the previous Section, as well as the transformed fit-function (solid line), transformed Gaussian core (dotted line) and transformed power-law tails (dashed line). We see that in terms of the transformed variable, $u$, the agreement between the Toy MC and fitting function is quite good over almost the entire range. We can see that there is more than one power describing the data between $u$=0 and $u$=0.1, or, equivalently, between $x = \infty$ and $x$ =3. The graph is nearly flat between $u$=0 and $u$=0.04, meaning that a power-law exponent of -3 between $5\sigma$ and infinity will describe the shape well. Between $3\sigma$ and $5\sigma$ we see that the data must follow a faster fall-off, so the exponent must be larger.

There is a small disagreement around $u$=0.05, corresponding to somewhere between 4 and $5\sigma$. This disagreement occurs when the tail function peaks, and disappears as the tail decreases steadily. There also appears to be a small disagreement in the region of $u < 0.01$, corresponding to greater than $10\sigma$. This discrepancy was also visible in the untransformed plot. Overall, we conclude that the parametrization given in Equation 2.4 describes the Toy MC quite well out to approximately $10\sigma$.

## 2.5 Dependence on Number of Scatters

The fitting process was repeated for different values of N, and the fitted parameters tabulated as a function of N. The number of events returned by the best fit was consistent with the actual number N=100,000. Figure 2.7 is a plot of the fit results for the mean of the distribution ($\mu$) versus the number of scatters (N). The mean of the distribution was generally consistent with zero, but varied between -0.007 and +0.004. This suggests that we can expect some small

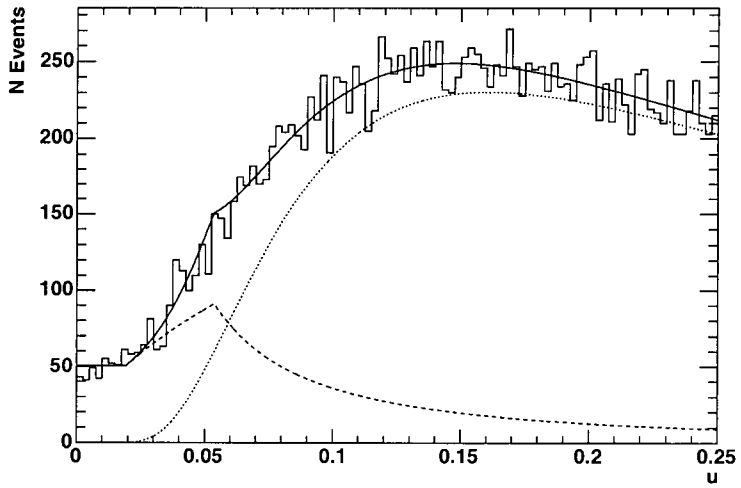


Figure 2.6: Histogram of $u = x^{-2}$ for $x$ generated by the MCS distribution, and the transformed version of the fitted function to the data (solid line). The Gaussian core (dashed) and power-law tail (dotted) components are also shown.

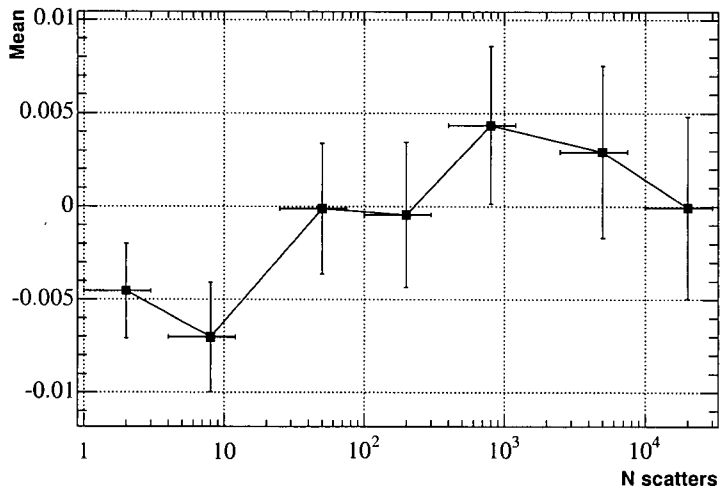


Figure 2.7: Plot of the mean of the Multiple Coulomb Scattering distribution, $\mu$, as a function of the number of scatters, N.

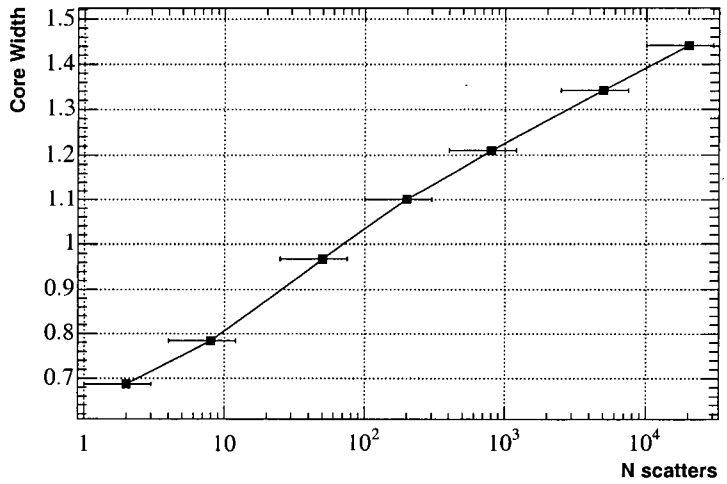


Figure 2.8: Plot of the fitted parameter representing the width of the core Gaussian, $\sigma$, as a function of the number of scatters, N.

variation of the mean to occur simply as a result of the statistical fluctuations in the fitting procedure when we apply this model to experimental data.

Figure 2.8 is a plot of the fit results for the width of the central Gaussian ($\sigma$) versus the number of scatters (N). We can clearly see a logarithmic dependence on the number of scatters. This is in general agreement with the dependence of the core width given earlier in Equation 2.3. We don't expect to see as much change in the experimental data since the thickness of material traversed in the detector doesn't vary by as many orders of magnitude.

Figure 2.9 is a plot of the fraction of the events in the tail function, $f$, as a function of N. When we only have 2 scatters, the purported tail fraction is very high because the distribution is not at all Gaussian. By the time we have increased to $10^5$ scatters, the tail fraction has dropped to approximately 2%. We can compare these fractions to the results found when we fit to the data, however, we note that the value of $f$ is not really the number of events beyond $3\sigma$. It is largely determined by the area of the flat tail function $T(x)$ under the core Gaussian. A change in the width of the core Gaussian will therefore change the value of $f$ substantially even if the other parameters describing the tail shape are unchanged. This behaviour must be borne in mind when we examine the value of $f$ in our experimental data.

Figure 2.10 is a plot of the exponent in the inner-portion of the power law tail, $p_a$, as a function of N. It ranges between 3.0 and 4.0, increasing rapidly with N. Again, when N=2 the distribution is closer to that of the original $x^{-3}$ than to the combination of a Gaussian and tail predicted by MCS theory. It appears that the value of $p_a$ asymptotically approaches a value of approximately 4.0, and

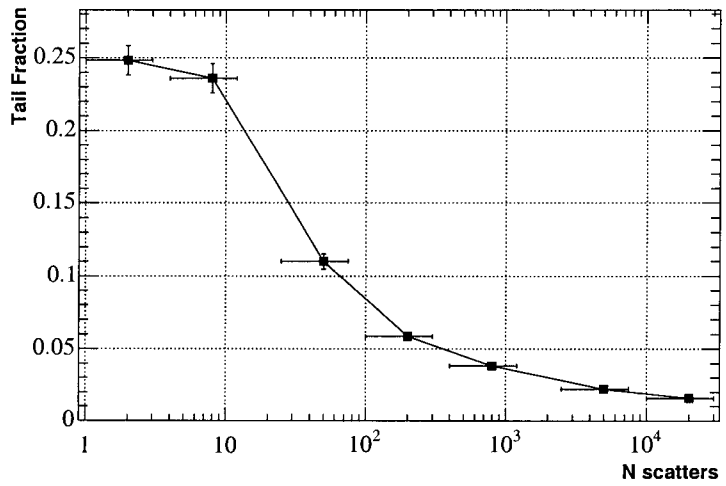


Figure 2.9: Plot of the fitted parameter representing the fraction of events in the tail, $f$, as a function of the number of scatters, N.

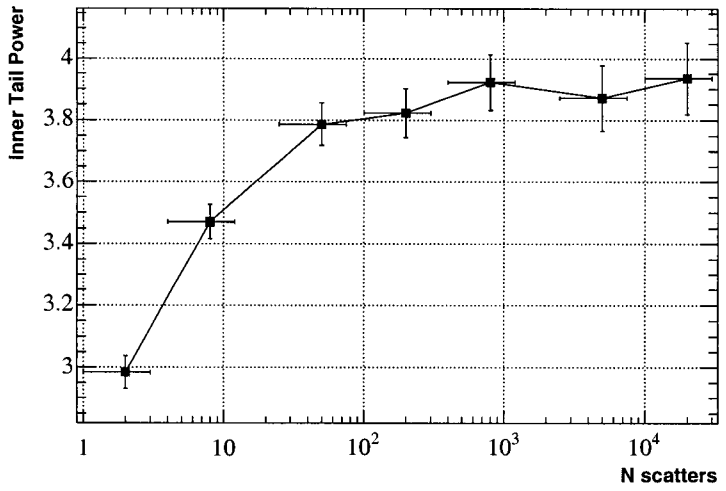


Figure 2.10: Plot of the fitted parameter representing the power in the inner power-law tail, $p_a$, as a function of the number of scatters, N.

we can check to see if the same values are obtained in our fits to experimental data. If the fitting function did not take into account the value of the core width, i.e. if it used $x^{-p_a}$ instead of $(\frac{x}{\sigma})^{-p_a}$ we would expect the inner tail power to depend strongly on the core width. As the breakpoint moved into the core it would raise the value of $p_a$ and vice-versa. If we divide the track-impact parameters by the core width in the experimental data then we should not see this effect, and the inner power-law should be approximately 4.0 if the tails in the track impact parameter resolution distributions are really due to Multiple Coulomb Scattering.

All of the behaviour seen in this Toy Monte-Carlo simulation should be clearly visible in the experimental data if the track impact parameter resolution tails are dominated by Multiple Coulomb Scattering. By dividing the deviations by the errors calculated by the tracking software we expect to obtain a distribution which closely resembles one of the Toy Monte-Carlo distributions. In real data we are unable to measure exactly the number of scattering layers a track has passed through, but we can construct a quantity that should be proportional to the amount of MCS and examine the resolution as a function of that quantity. On the other hand, if there are other significant contributions to the track impact impact parameter resolution which are not described by either the geometric detector resolution or the effects of Multiple Coulomb Scattering, then the experimental data should display markedly different behaviour than these Toy Monte-Carlo simulations.

# Chapter 3

# Lepton Pair Production Processes

In this chapter we examine the physical processes responsible for the events which we will use to study the track impact parameter resolution. In order to fully explore the tails of the impact parameter resolution functions, it is necessary to use a very large sample of dilepton events so that the distributions will be populated with a significant number at many $\sigma$ away from the central value. The easiest way to study the actual resolutions is to use the QED events that are already present in large quantities in the data to characterize the track impact parameter resolution functions. There are two main categories of events containing lepton pairs: the first is "Bhabha" scatters and the related muon pairs, and the second are "Two-Photon" events.

## 3.1 Bhabha Scattering and Muon Pair Production

This section describes the physical processes by which Bhabha scattering and muon pair-production occur. This interaction was named after H.J. Bhabha, who first described it in detail for electrons [19]. The process can be described by the two Feynman diagrams[1] in Figure 3.1a and b, known as the annihilation or $t$ diagram and exchange or $s$ diagram, respectively. The differential cross-section of the annihilation diagram is given by:

$$\frac{d\sigma}{d\Omega} = \frac{\alpha^2}{4s}(1 + \cos^2(\theta)) \tag{3.1}$$

where $s = E_{cm}^2$ is the square of the total energy in the CM frame. Muon pairs are only produced through the annihilation diagram. The angular distribution for electrons in the final state is more complicated, because it depends on the amplitude for both diagrams, including interference between them. The cross-section for electron production strongly peaks at $\theta$=0 in the CM frame, while the cross-section for muon production is more isotropic in the CM frame. The two final state leptons (either electrons or muons) will have nearly equal momentum magnitude in the CM frame. We expect these leptons should all have one-half

[1] All Feynman diagrams produced with the JaxoDraw [20] software package.

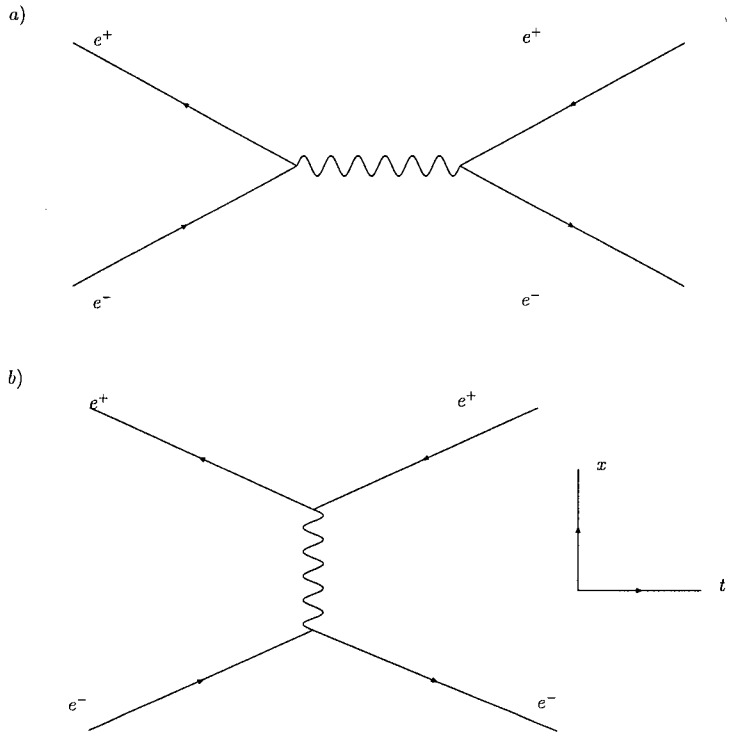


Figure 3.1: Bhabha-scattering of the incoming electron and positron to produce an outgoing lepton pair in the a) annihilation channel and b) exchange channel.

the total CM energy, or approximately 5.2 GeV. A simulated momentum spectrum for electron pairs in the CM frame is shown in Figure 3.2. The spectrum was obtained using the "BHWIDE" event generator software package [21] and the standard *BABAR* reconstruction software described in Chapter 5 of this document. The spectrum for muon pairs is virtually indistinguishable from that of the electrons, except that the peak momentum occurs about 105 MeV lower due to the muon's larger mass.

Lepton pairs scattered through the exchange diagram will still have most of their momentum along the beam axis, since the cross-section for that diagram peaks at $\theta = 0$, and their $p_T$ spectrum will fall off rapidly. Lepton pairs which interact through the annihilation diagram will have a more isotropic distribution in the CM frame and a momentum spectrum peaking at about 5 GeV. The $p_T$ spectrum for leptons produced through annihilation also peaks at roughly 5 GeV with a low-energy tail.

The Feynman diagrams shown in Figure 3.1 can be modified by the emission of real photons from either the initial or final state particles, as shown

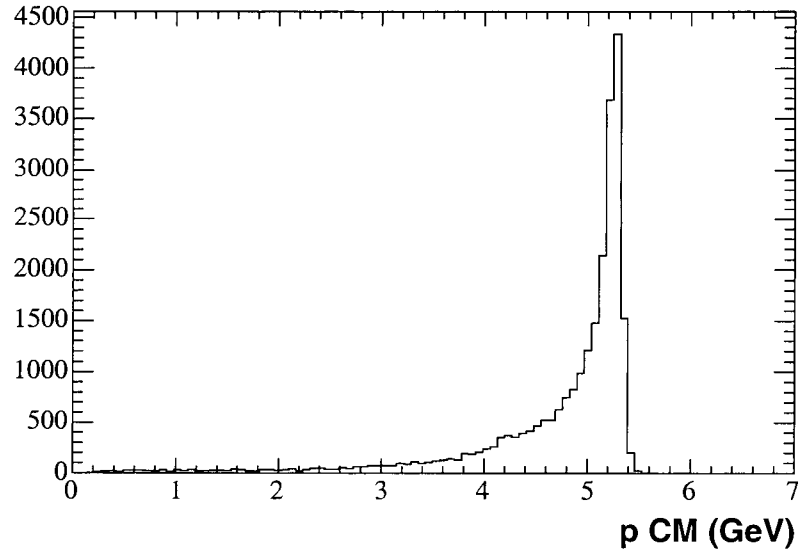


Figure 3.2: Distribution of momenta in the CM frame for Bhabha-scattered electrons produced with the PEP-II beam energies.

in Figure 3.3. We expect a low-energy tail in the lepton spectrum, made up of leptons which have lost some of their initial energy by radiating a photon. In both initial and final state radiation, these processes will create final state leptons with less than 5 GeV of momentum in the CM frame, and the tracks will not be entirely back-to-back in the CM frame either. Initial state photons will tend to be emitted parallel to the incident beams, and will therefore escape down the beampipe without detection. These events will have only two visible charged tracks in them and nearly balanced transverse momentum, but missing energy. If the final state particles emit photons then the photons will normally be detected and could be included in the event reconstruction. If they are not included in the event reconstruction the events will be rejected because the charged tracks' $p_T$ will not balance exactly.

## 3.2 Two Photon Process

In order to obtain a large number of dilepton events which have transverse momenta between 0 and 4 GeV we also consider the so-called Two-Photon events, produced via the following reaction:

$$e^+e^- \rightarrow e^+e^-\gamma^*\gamma^* \rightarrow e^+e^-l^+l^- \tag{3.2}$$

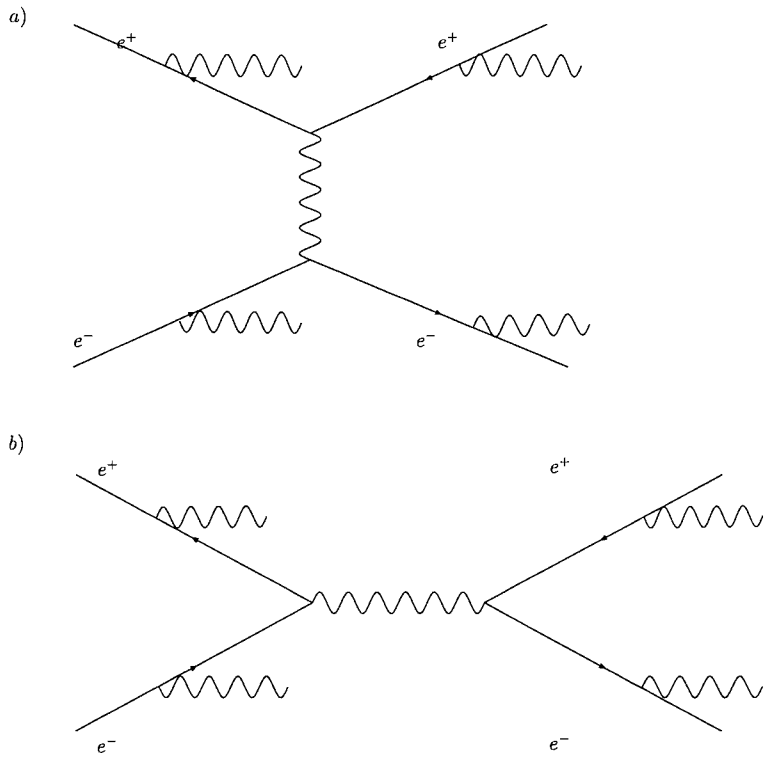


Figure 3.3: Feynman diagrams for a) exchange and b) annihilation diagrams with real photons radiated from all initial and final state particles. Normally only one of the four particles would emit a real photon.

The general two photon process producing a fermion pair is shown in the Feynman diagram of Figure 3.4a. If the final state is hadronic the vertex can only be treated approximately, but if the final state is a lepton pair, as shown in Figure 3.4b, then the process can be treated exactly through a lepton hairpin. These two photon events have momentum spectra peaking at zero and falling off steeply with energy. Their transverse momenta are basically equal and can range up to 5 GeV. They represent the vast majority of dilepton events in which the CM momenta are less than 4 GeV. In addition, any one of the photons in Figure 3.3 can also produce a fermion pair. A simulated spectrum for muon pairs produced through the two-photon process is shown in Figure 3.5. The spectrum was produced using the "GAMGAM" event generator software package which is currently the two-photon physics standard for the *BABAR* collaboration, although it was originally written for the CLEO-II experiment [22].

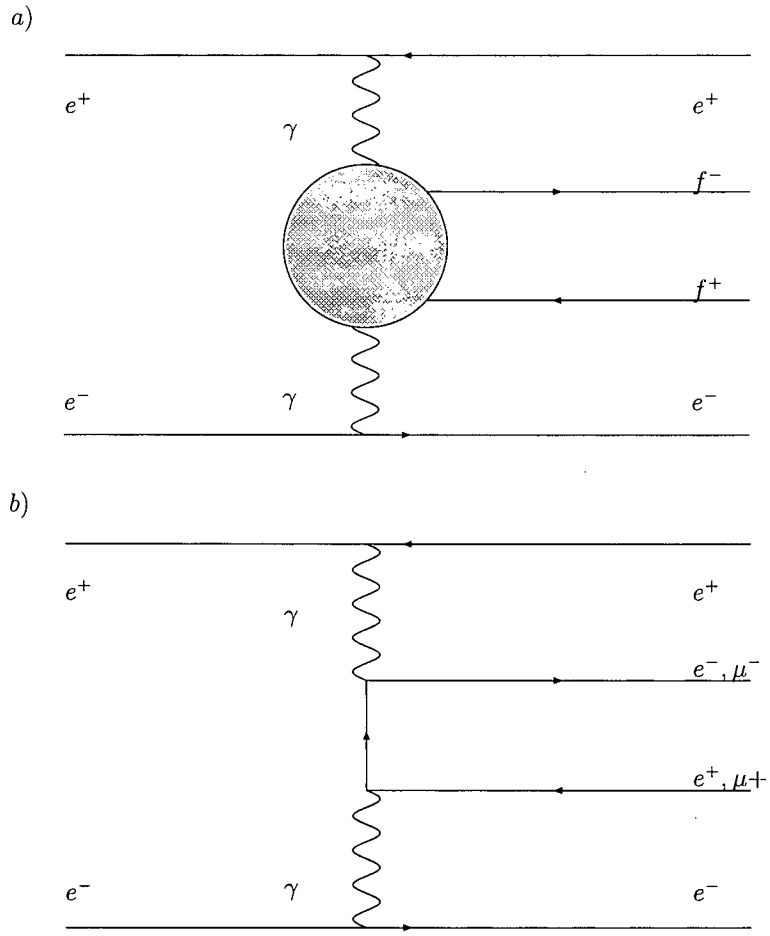


Figure 3.4: Two-Photon production of a) generic fermion pair, b) lepton pair via a lepton hairpin.

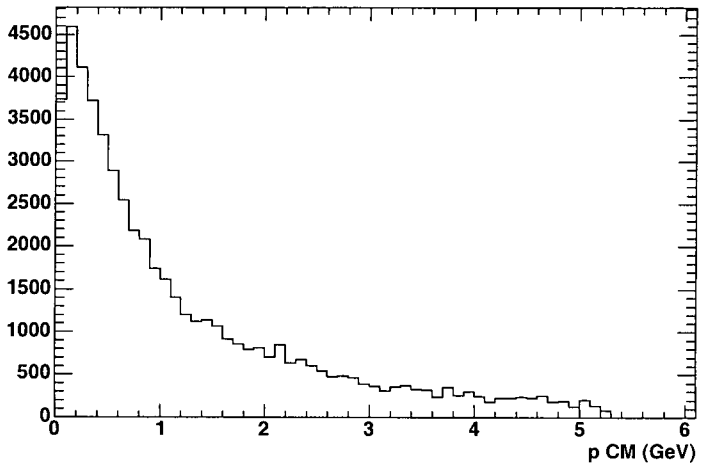


Figure 3.5: Distribution of momenta in the CM frame for muons produced in the Two-Photon process with the initial beam energies of the *BABAR* experiment.

# Chapter 4

# The *BABAR* Detector

## 4.1 Overview

The *BABAR* detector is located at the PEP-II accelerator at the Stanford Linear Accelerator Centre (SLAC), shown schematically in Figure 4.1. Electrons are accelerated to an energy of 9 GeV, and positrons are accelerated to an energy of 3.1 GeV, before they collide in the interaction region IR2. These energies create a system with a CM energy of 10.58 GeV, and a Lorentz boost in the lab frame of $\beta\gamma = 0.58$. The *BABAR* detector, shown in Figure 4.2, is comprised of

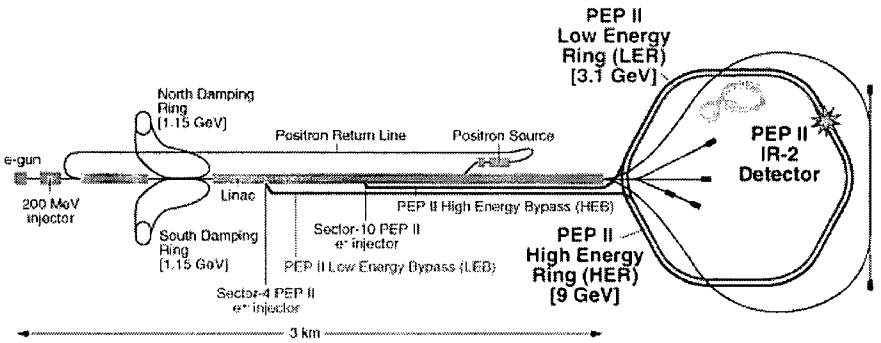


Figure 4.1: Schematic view of the PEP-II accelerator at SLAC.

five subsystems. The innermost is the Silicon Vertex Tracker, based on silicon micro-strip detectors. Next is a multi-wire drift chamber filled with an Argon-Isobutane gas mixture, followed by a detector of internally-reflected Čerenkov light used for particle identification. An electromagnetic calorimeter, composed of CsI(Tl) crystals, measures the photon energies and angles. A 1.5T superconducting magnet encloses the inner four detector layers and the axial magnetic field forces charged particles to follow curved trajectories in the detector. The magnetic flux return is instrumented with resistive plate chambers to detect neutral hadrons and identify muons by penetration. Measurement of the track curvature determines the track momentum and combining the momentum with the velocity measured by the DIRC allows the determination of the particle mass. Full details of the *BABAR* detector design and performance can be found in [23].

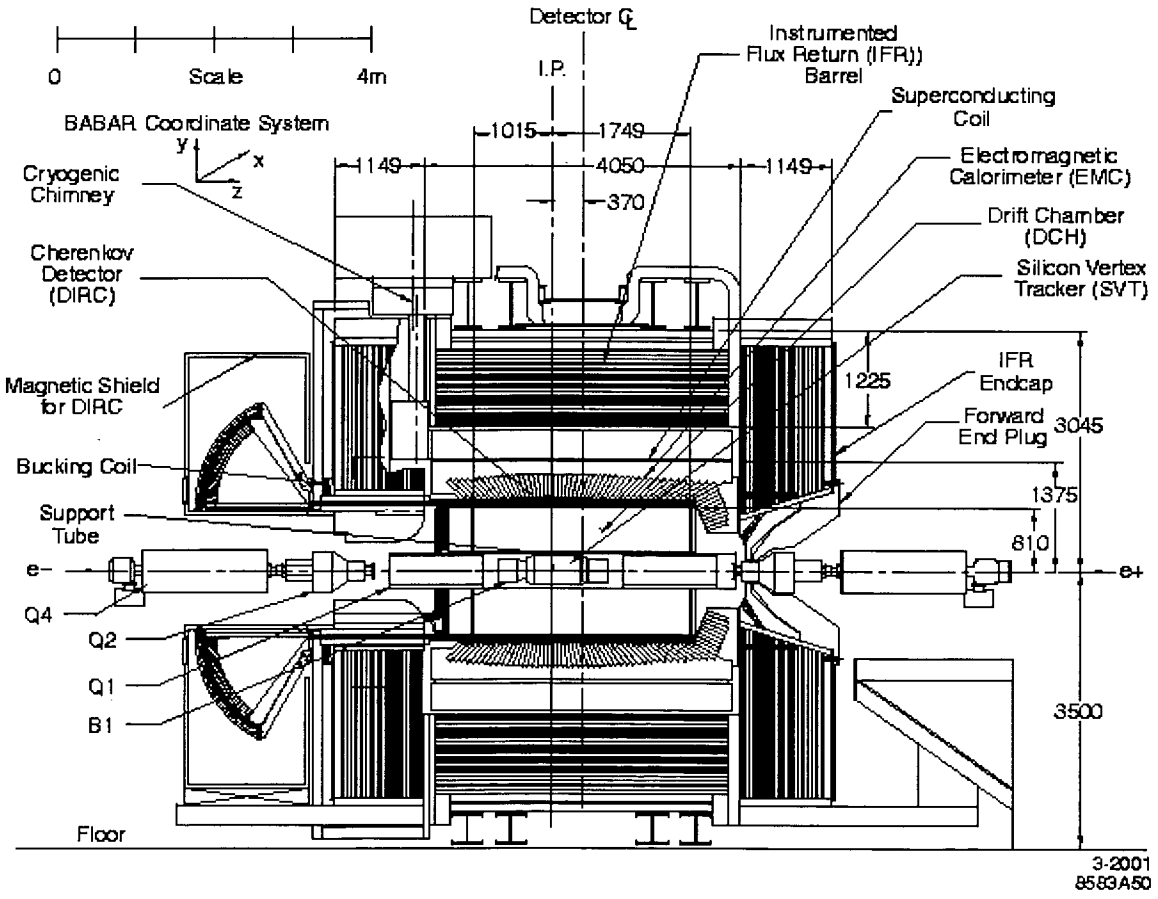


Figure 4.2: Cross-sectional view of the *BABAR* detector at the PEP-II accelerator. All dimensions are in mm.

## 4.2 Silicon Vertex Tracker

The micro-strip silicon vertex tracker (SVT) is composed of five double-sided layers. The layers are segmented into strips used to determine a passing particle's location along both the $z$ and $\phi$ axes. In total, there are roughly 150,000 individual strips read out from the SVT. When a charged particle passes through the active regions of silicon, it deposits energy which leads to the creation of electron-hole pairs. These pairs are swept apart by an applied voltage and the resulting current pulse is detected as a "hit" in one of the strips. The locations of hits are combined to infer the location of the track at each layer of the SVT.

When attempting to measure the vertex of dilepton events, the resolution is primarily determined by the SVT, since the hits in the silicon are the closest points along the track to the beamspot and their spatial resolution is the best. For tracks with high transverse momentum ($p_T$), the SVT can resolve the point of closest approach to the beamspot to within 50 $\mu$m, and sometimes as accurately as 10 $\mu$m. This resolution is primarily determined by the following factors: the strip size in the SVT, the angle at which the track traverses the SVT layers and the track momentum. Values are calculated for each track as they are reconstructed in the software, providing resolution estimates on a track by track basis. In addition, the alignment of the SVT with respect to the beams is calibrated on a continual basis, and contributes another systematic error to the vertex measurements.

## 4.3 Multi-Wire Drift Chamber

The multi-wire drift chamber (DCH) is filled with a mixture of helium and isobutane ($C_4H_{10}$) gases kept at 4 mbar above atmospheric pressure. The sense wires are kept at high-voltages ranging between 1900-2000V. There are a total of 28768 wires, and they are arranged into forty different concentric layers. Twenty-four of the forty layers are placed at a small angle relative to the $z$ axis to measure the $\theta$ angle of passing tracks.

When a charged particle passes through the DCH, some of the gas is ionized along the path of the track and the ionized gas molecules are attracted to the ground wires while the liberated electrons are drawn toward the sense wires. The electrons collide frequently with gas molecules on their way to the sense wire, resulting in a constant drift velocity. When the electrons are very close to the wires, the increased electric field gives them enough energy to knock loose additional electrons from each gas atom. This creates a large gain in the signal picked up by the sense wire, on the order of 50,000 for this particular gas mixture and voltage setting. The resulting voltage pulses on the sense wires are read out and their arrival times are converted into distances from the wire, using the constant drift velocity. The position resolution ranges between 0.1 and 0.4 mm, depending on how far away from the wire the original track was located. This resolution is ultimately the limiting factor in determining how well the track curvature parameter $\omega$, and hence the momentum, can be measured.

The other important measurement made by the DCH is of energy loss per unit distance, or $dE/dx$. The total charge deposited in each cell of the chamber is used to calculate the energy loss over the chamber width. There are a number of corrections applied to improve the measurement accuracy, including continuous updating of the gas pressure, temperature and gain, wire-by-wire geometrical constants and variation of the energy loss with the angle of the incident particle. Ultimately the accuracy of $dE/dx$ measurements is roughly 7%. The measurement of $dE/dx$ within the DCH can be used for particle identification in conjunction with the Detector of Internally Reflected Čerenkov Light (DIRC), or by itself for tracks which are within the acceptance of the DCH but miss the DIRC.

## 4.4 Detector of Internally Reflected Čerenkov Light

A charged particle travelling with velocity $\beta = v/c$ in a medium of refractive index $n$ produces Čerenkov light if $n\beta \geq 1$. For relativistic charged particles, a cone of Čerenkov radiation is emitted with a characteristic angle given by:

$$\cos(\theta_c) = 1/(n\beta) \tag{4.1}$$

Measurement of the Čerenkov angle, in conjunction with knowing the particle momentum from the drift chamber, allows a determination of the particle mass and hence, the particle type.

The DIRC sub-detector is a novel device used for the first time in the *BABAR* experiment. It is a ring imaging Čerenkov detector based on total internal reflection and uses quartz bars as both the radiator and the light guide. The DIRC Čerenkov radiators are 4.9 m long rectangular quartz bars oriented parallel to the $z$ axis of the detector. The quartz has an index of refraction $n$=1.473. Through internal reflections, the Čerenkov light from the passage of a particle through the DIRC is carried to the ends of the bar, as shown in Figure 4.3. This radiation is captured by internal reflection in the bar and transmitted to the photon detector array located at the backward end of the detector (forward-going light is reflected by a mirror located on the end of the bar). The high optical quality of the quartz preserves the angle of the emitted Čerenkov light during total internal reflection.

An advantage of the DIRC for an asymmetric collider, like PEP-II, is that the high momentum tracks are boosted forward, causing a much higher light yield than for particles at normal incidence. This is due to two effects: the longer path length in the quartz and a larger fraction of the produced light being internally reflected in the bar.

The photon detector array consists of about 11,000 conventional 2.5 cm-diameter photomultiplier tubes. They are organized in a close-packed array at a distance of about 120 cm from the end of the radiator bars. The photo-tubes, together with modular bases, are located in a gas-tight volume as protection against helium leaks from the drift chamber.

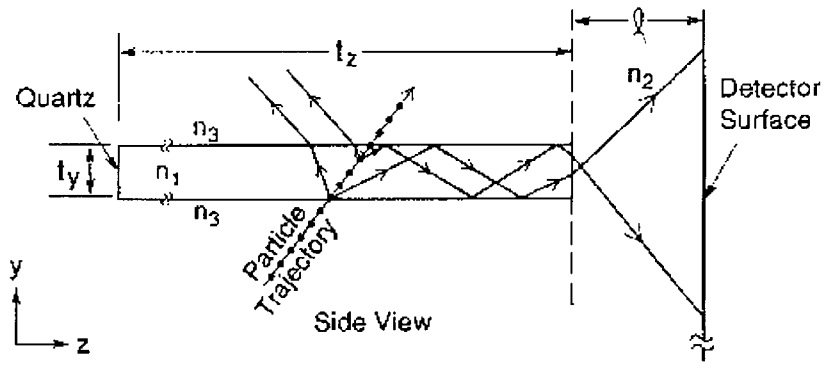


Figure 4.3: Cross-sectional view of a quartz radiator in the DIRC, showing the internal reflections of the Čerenkov photons.

To maintain good photon transmission for all track dip angles, the standoff region is filled with water to minimize the change in index of refraction. The water seal occurs at a quartz window that is glued to the quartz wedges. The standoff box is surrounded by a steel box which provides adequate magnetic shielding for the photo-tubes.

The main design goal for the DIRC was to be able to distinguish pions and kaons at momenta greater than 2 GeV/c. The statistical separation between the two species ranges from about $10\sigma$ at 2 GeV/c to approximately $3\sigma$ at 4 GeV/c, easily meeting the specified design requirements.

## 4.5 Electro-Magnetic Calorimeter

The Electromagnetic Calorimeter (EMC) was designed to measure electromagnetic showers with high efficiency, high angular resolution, and high energy resolution over the range from 20 MeV to 9 GeV. The lower energy limit is determined by the need to reconstruct $\pi^0$'s resulting from $B$ decays, and the higher energy limit is necessary to measure Bhabha-scattered electrons and muons. The EMC is also helpful in identifying electrons.

This sub-detector is divided into two parts, a cylindrical barrel surrounding the inner detector systems, and a conical forward end-cap. The barrel is composed of 5880 Thallium-doped Caesium-Iodide crystals, arranged into 280 separate modules, while the end-cap contains 20 modules of 41 crystals each. CsI(Tl) was chosen for the crystals primarily because of its high light yield and small Moliere radius which allow for excellent energy and angular resolution.

High-energy photons and electrons travelling through the material of the

calorimeter create electromagnetic showers and the resulting photons are absorbed by the crystals and re-emitted as visible light. These scintillation photons are then detected by high-speed silicon photo-diodes mounted on the outer surfaces of the crystals. Silicon photo-diodes were chosen because of their ability to function properly inside the 1.5T magnetic field of the *BABAR* solenoid and because it is possible to match their absorption spectrum to that of the crystal light output.

The measured energy resolution of the EMC ranges from 5% with a 6.13 MeV radioactive source, down to 1.9% for Bhabha-scattered electrons at 7.5 GeV. The angular resolution varies from 12 mrad at low energies to 3 mrad at high energies. Finally, the energy measured in the EMC is used with the momentum determined by the drift chamber in order to identify electrons with an efficiency of between 88-94%, and a pion misidentification probability ranging from 0.15-0.3%.

## 4.6 Instrumented Flux Return

The Instrumented Flux Return (IFR) was designed to identify muons with high efficiency and low contamination, as well as to detect long-lived neutral hadrons over a wide range of angles and momenta. The main objectives for the IFR are large coverage angles, good efficiency and good rejection of muon background down to momenta lower than 1 GeV/c. For the neutral hadrons, high efficiency of detection and good angular resolution are the most important criteria.

The IFR is divided into three separate sections: a cylindrical barrel and forward and backward end-caps. Each section is composed of layers of iron absorber material interspersed with active detector layers. The iron absorbs energy from highly-penetrating muons and long-lived neutrals, as well as acting as the flux return for the solenoidal superconducting magnet. The number of layers of steel, and their thickness, were chosen using simulations to optimize the detection of muons and neutral hadrons. The steel absorber consists of 18 steel plates with thicknesses ranging from 2-10 cm. The active detector layers were originally Resistive Plate Chambers (RPCs) [24], that provide two-dimensional coordinates and precise timing information for passing particles. The barrel originally contained 19 RPC layers and the end-caps had 18 active layers.

An RPC consists of two bakelite plastic plates separated by a 2 mm gap containing a gas mixture of argon, freon and isobutane. The bakelite has a volume resistivity of approximately $10^{11} - 10^{12} \Omega$cm. The inner surfaces of the gas-filled gap are coated with linseed oil in order to reduce high-voltage breakdown. A voltage of roughly 8 kV is applied between the two plates and the passage of a particle leads to the creation of a limited streamer between the plates. The plates are read capacitively with strips running along both the $z$ axis and in the $\phi$ direction. There are a total of approximately 50,000 channels.

The efficiency of individual RPC modules can be determined using cosmic rays. Initially more than 75% of the modules had an efficiency greater than 90%, but at least 50 modules had already failed by the summer of 1999. Between 1999

and 2004 the overall efficiency of this detector system continued to degrade from 98% to roughly 75%. The angular resolution of the system continued to meet the design criteria.

Due to the continuing problems with RPCs, the *BABAR* collaboration decided in 2004 to undertake their replacement with another technology known as Limited Streamer Tubes (LSTs) [25]. These use extruded plastic tubes with wires inside, instead of the flat gaps. They have a long successful history, and are manufactured with a high degree of quality and reliability. The first two sextants of the IFR were disassembled and the LSTs were installed during the summer shutdown of 2004. The rest of the RPC modules will be replaced during the summer shutdown of 2006.

The IFR is primarily used for particle identification of high energy muons and $K_L^0$s. The efficiency of muon ID has continually decreased due over the past 5 years due to the degradation of the RPCs, but this does not affect this analysis in any way. This analysis studies the vertex resolution of tracks identified as muons and is not concerned with the absolute number of muons, or the efficiency of their detection.

# Chapter 5

# Data Acquisition and Event Reconstruction

## 5.1 Overview

There are three distinct stages of reconstruction between the raw electronic pulses in the detector elements and the calculation of physics quantities of interest such as branching fractions and resonance masses. A schematic diagram of the *BABAR* Data-Acquisition system (Figure 5.1) depicts the main stages of the data reconstruction and storage process. Full details on the *BABAR* Data-Acquisition system can be found in Reference [23]. There are two levels of

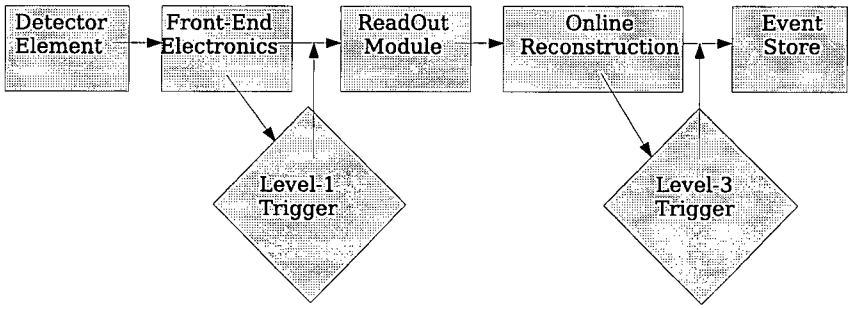


Figure 5.1: Schematic view of *BABAR* Data-Acquisition system.

triggering in the *BABAR* experiment. They are commonly referred to as the Level-1 (L1) Trigger and the Level-3 (L3) Trigger. The Level-2 Trigger was not implemented. The Level-1 Trigger uses fast electronics along with a pipeline buffer in order to accept or reject events within 11 $\mu$secs. The Level-3 Trigger is implemented in software and utilizes calculated physics values to decide whether to accept events for storage in the database, or reject them.

## 5.2 Hardware System

The Front-End Electronics and Level 1 trigger system of the *BABAR* detector are shown schematically in Figure 5.2. In Step 1 of the process shown in Figure 5.2,

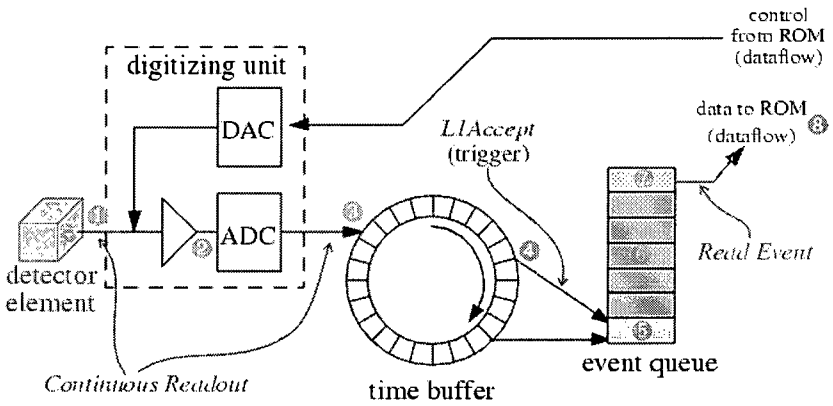


Figure 5.2: Schematic view of *BABAR* Front-End Electronics and Level-1 Trigger system.

events are initially just voltage pulses in various detector elements. In Step 2, these voltage pulses are readout by attached Analog-to-Digital Converters (ADCs) which digitize the voltage, and in some cases, the waveform of the raw detector pulses. In Step 3, these digital signals are then passed into a circular buffer, which is being continually overwritten. This buffer is necessary to allow time for the L1 trigger to consider a group of signals, and if desired, pass them along, before processing the next signals. In Step 4, the L1 trigger fires within a window of 11-12 $\mu$s after an $e^+e^-$ crossing. If an event of interest is detected, all of the data channels are transferred from the detector to output buffers in Step 5. In Step 6, the detector signals make their way through the buffer, until reaching the top in Step 7. Once at the top of the buffer they are sent from the buffer to the ReadOut Modules (ROMs) in Step 8. The Readout Modules are responsible for sending information from the detector electronics to the *BABAR* computing system.

The ADC and buffer are both part of the Front End Electronics (FEEs) that accompany each detector subsystem. Typically a single FEE card is designed to handle many detector elements in parallel, and ROMs are designed to gather the information from several FEE cards in parallel. The maximum rate for L1 acceptance is approximately 2.5 kHz, and *BABAR* has normally operated at approximately 1 kHz, well within the available bandwidth.

The standard L1 trigger decision is based on three signal types: charged tracks in the DCH which have higher $p_T$ than a threshold value, clusters in the

EMC which have more than a minimum amount of energy, and muon tracks detected by the IFR. In order to calculate these quantities, a series of Field-Programmable-Gate-Arrays (FPGAs) are used to perform basic reconstruction tasks like constructing track segments from DCH hits, adding energy in adjacent crystals of the EMC and determining where in the IFR muons have passed. The output of the FPGAs are then combined in hardware to generate the overall Level 1 Trigger signals. An implementation of the same algorithms in software would not be fast enough to process events within the 12 $\mu$s window.

If an L1 accept is issued, then the data is passed on to the next stage, the Level-3 Trigger.

## 5.3 L3 Trigger

From the ROMs, the digital data representing signals in the detector elements pass through an Ethernet connection to a farm of 32 computers running the Level-3 Trigger software. The purpose of the Level-3 Trigger (L3) is to determine whether or not the "event", made up of a collection of detector signals, represents an $e^+e^-$ collision, or a collection of random hits. The L3 trigger is essentially a refined and augmented software implementation of the L1 trigger logic.

For example, in the L3 DCH algorithm the track segments identified in the L1 system are refined and refit, adding and subtracting adjacent hits and track segments in order to improve the quality of the fit. This allows a much better resolution on track parameters, and better rejection of tracks resulting from beam-gas or beam-wall interactions. The tracks are combined and averaged by the L3 software to determine an event time, $t_0$.

The L3 EMC algorithm forms clusters of EMC hits just as the L1 system did, but with added filters applied. The time at which the hit occurred is required to be within 1 $\mu$s of $t_0$, and the energy deposited in the crystal is required to be greater than or equal to 20 MeV. In addition to simply forming clusters, the centroid and lateral moment of each cluster is calculated and used later for particle identification.

The event stream at this stage is dominated by Bhabha events. To economize on data storage costs, only a fraction of the Bhabha events are retained. Events are rejected based on one-prong and two-prong topologies, in which either only the positron, or both the positron and electron are seen in the detector. The rejection is scaled to produce a flat distribution in polar angle. Even after this rejection, approximately 30% of the stored events are either radiative Bhabhas passing the filter or Bhabhas stored for use in calibration. This analysis will focus on these "background" events and ignore events containing $B$ mesons.

If events pass the L3 trigger, they are stored on tape. The L3 trigger passes events at a rate of approximately 120 Hz, a rate chosen to balance the desire for completeness of the data sample and the burden of database storage and "offline" processing.

## 5.4 Reconstruction

The reconstruction software can be thought of as a bridge between the data-readout in the electronics and the end-user analysis system. One needs to reconstruct enough physics information in order to make an informed decision about whether or not we have a signal event, or just background detector hits. Besides applying some of the calibration constants (particularly for the EMC), the reconstruction also repeats the preliminary track-finding, taking individual detector hits and associating them with each other into tracks and calorimeter clusters. The software used in reconstruction is built upon some of the same C++ classes as the end-user analysis software in order to improve reliability and consistency. Essentially, raw information from the detector is reconstructed into the object-oriented events that are used in the offline analysis software.

For the purposes of the analysis in this thesis the primary task of the reconstruction software is to construct three-dimensional trajectories for charged particles out of the individual hits in the SVT and DCH. This is done by first searching for a cluster of hits located in adjacent layers of the DCH, and constructing a simple track segment from those hits. The charged particle trajectories can be described in terms of a 5-parameter helix and the measured value of the magnetic field in the detector. Figure 5.3 depicts the projection of a charged track into the x-y plane. The point-of-closest-approach (POCA) is the point along the track helix closest to the z-axis. In the *BABAR* set of helix parameters, $d_0$ is the perpendicular distance between between the POCA and the z-axis, $\phi_0$ is the angle between the track momentum at the POCA and the x-axis, $z_0$ is the z-coordinate of the POCA, $\rho$ is the radius of curvature of the track, and the curvature $\omega = 1/\rho$. The two parameters $d_0$ and $z_0$ are referred to as the track impact parameters.

Figure 5.4 depicts the projection of track momentum into the y-z plane. The momentum of the track is divided into two components, $p_T$ in the x-y plane, and $p_z$ along the z-axis. The track parameter $\tan(\lambda) = p_z/p_T$ is the "dip" of the track away from the xy-plane. For the initial track fits, the hypothesized mass is equal to that of a pion, and if particle identification later shows that the track is an electron it is necessary to repeat the helix fit with the correct mass value. Note that determining the absolute origin of a helical track is not possible; we can only locate the point-of-closest-approach to the beam crossing and assume that primary particles have been produced at or near that point. Locating the origin of secondary particles is a more difficult problem, and will not be considered in this thesis. The group of hits associated initially with a track are used to perform a $\chi^2$ fit in order to determine the best values for the track parameters. This is repeated iteratively, adding and removing hits in order to improve the fit results until convergence is achieved.

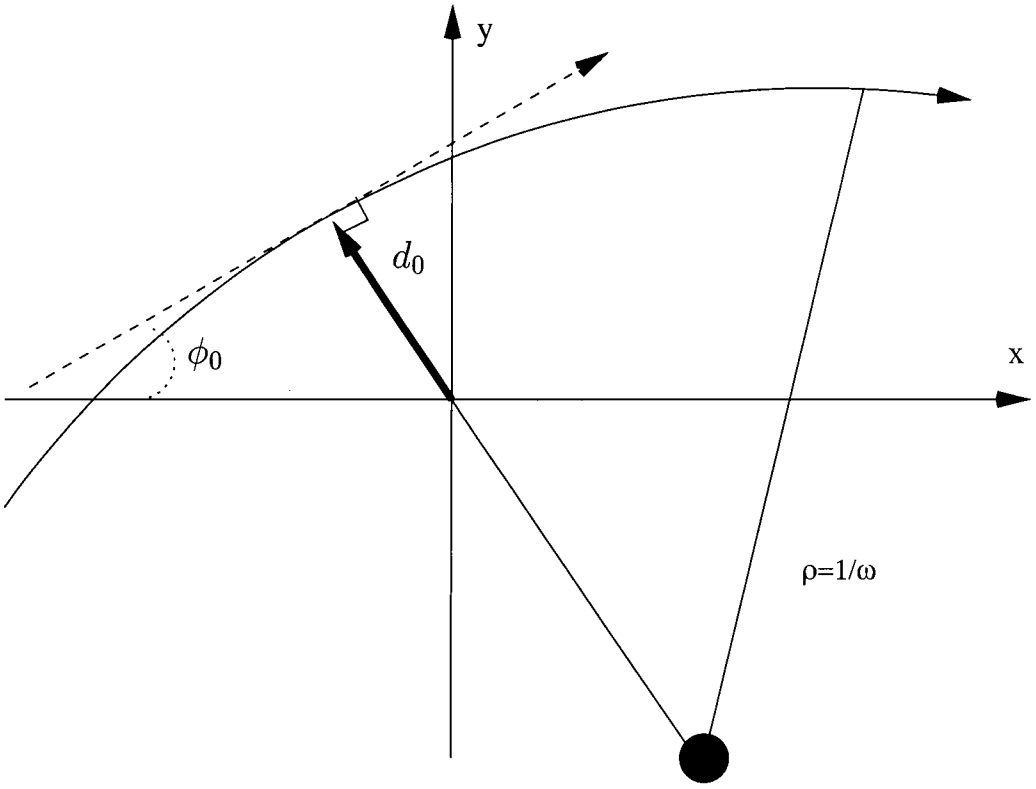


Figure 5.3: Projection of a charged track into x-y plane. Track parameters $d_0$, $\phi_0$ and $\rho = \frac{1}{\omega}$ are shown.

## 5.5 Conversion from Helix Parameters

There is one remaining task that is performed in the offline reconstruction code, the calculation of physics 4-vectors from the track helix parameters. In mathematical terms, the conversion is from five helix parameters plus the magnetic field to three position (x,y,z) and three momentum ($p_x$, $p_y$, $p_z$) values. The calculations are first performed at the point-of-closest-approach to the z-axis.

The transverse momentum, $p_T$, is directly proportional to the radius of curvature of the helix, $\rho$, and the strength of the magnetic field, $B$:

$$p_T \text{ (GeV/c)} = 0.2997 \, |B| \, \rho \text{ (Tm)} \tag{5.1}$$

with a factor of 0.2997 if the units are GeV/c for momentum, Tesla for the magnetic field and metres for the radius of curvature. From $p_T$ we can obtain

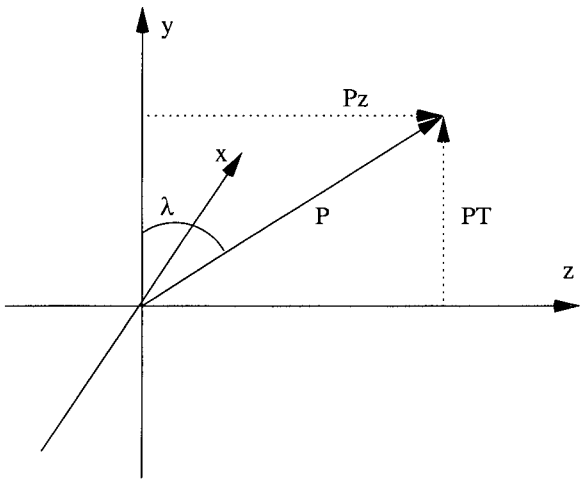


Figure 5.4: Projection of track momentum into y-z plane. Track parameters $p_T$, $p_z$ and $\lambda$ are shown.

the x and y components of momentum:

$$p_x = p_T \cos(\phi_0) \tag{5.2}$$

$$p_y = p_T \sin(\phi_0) \tag{5.3}$$

The z component of momentum can be calculated using the relation:

$$p_z = p_T \tan(\lambda) \tag{5.4}$$

The (x,y,z) coordinates of any point along the track can be obtained from the values of $d_0$, $\phi_0$, and the distance along the helix $\psi$:

$$x = -(d_0 + \frac{1}{\omega}) \sin(\phi_0) + \frac{1}{\omega} \cos(\psi) \tag{5.5}$$

$$y = (d_0 + \frac{1}{\omega}) \cos(\phi_0) + \frac{1}{\omega} \sin(\psi) \tag{5.6}$$

$$z = z_0 + \frac{1}{\omega} \tan(\lambda)\psi \tag{5.7}$$

Once these laboratory quantities have been calculated, and the mass is known, a relativistic 4-vector can be constructed for each track. Each event also has a beam-beam CM 4-vector associated with it. These are calculated as part of the offline calibration process. The beam-beam CM 4-vector can be used to rotate and boost the track 4-vectors into the CM frame.

It is worth noting that the origin of the detector and the beamspot are not perfectly aligned. In fact the beam-crossings occur in a cigar shaped region of approximately 5 $\mu$m width in the x-direction, 100 $\mu$m width in the y-direction,

and a length of about 10 mm in the z-direction. This interaction region is located roughly at the detector coordinates of (x,y) = (-0.25, +2.8) where x and y are in mm. In addition, the z-axis of the detector is not perfectly aligned with the beam axis. It is rotated in the $\theta$ and $\phi$ directions by 20 and 10 milliradians, respectively. Tracks are reconstructed with respect to the detector origin and need to be rotated and shifted appropriately when we are calculating distances and angles with respect to the beam crossing.

# Chapter 6

# Event Selection

## 6.1 Overview

There are several fundamental requirements that our signal events must satisfy. The first is that they should contain two charged tracks emanating from the same point in space. The second is that they should contain tracks resulting from an interaction at the beamspot, and with no lifetime, meaning that the observed tracks were created at the point where the incoming beam particles collided.

We need to exclude continuum *uds* events, charm events, $B$ mesons and $\tau$ pairs because all of these have significant lifetimes. By imposing cuts on the multiplicity and $p_T$ balance of the events we can remove nearly all of these sources of background, since they tend to have more final state particles than our events of interest.

We also need to exclude events containing cosmic rays, beam-wall and beam-gas interactions. These events have the right number of tracks, but don't originate from the beam-crossing location in the center of the detector. These events can be removed by imposing cuts on the event geometry to distinguish them from our signal events.

## 6.2 NTuple Creation

To begin with, we load all recorded events which passed any of the triggers in the Data Acquisition System. These events contain tracks from $e^+e^-$ scatters, $B$ and $D$ decays, $\tau$ pairs, continuum *uds* production, cosmic rays, beam-gas, and beam-wall interactions. I used database collections representing approximately $19.2nb^{-1}$ of data acquired during the year 2003.

There are several different lists of charged tracks, photons and neutrals which are constructed from the raw data and could be used to fill an ntuple. Each list has a different set of requirements which a candidate must pass in order to be included. For this analysis I chose to use the following lists:

- Charged Tracks = "GoodTracksLoose"
- Photons = "GoodPhotonDefault"
- Neutrals = "GoodNeutralLooseAcc"

The charged tracks are selected from all candidate charged tracks, based on hits in the SVT and DCH. The photons and neutral hadrons are selected from single-peaked clusters in the EMC which don't correspond to any of the charged track candidates. EMC clusters which are multiply-peaked are used in other processes searching for $K_s$'s and $\pi_0$'s, and are ignored in my analysis. The criteria used to fill each of the lists used in this analysis are given in Table 6.1.

| GoodTracksLoose | GoodPhotonDefault | GoodNeutralLooseAcc |
|---|---|---|
| Track $p_T \geq 0.1$ GeV | Raw E $\geq 0.1$ GeV | Raw E $\geq 0.03$ GeV |
| Track $p < 10$ GeV | n Crystals $\geq 0$ | n Crystals $\geq 0$ |
| nHits DCH $\geq 12$ | Lat Moment $\leq 0.8$ | Lat Moment $\leq 1.1$ |
| DOCA in xy $\leq 1.5cm$ | | $0.41 \leq \theta \leq 2.409$ |
| DOCA along z $\leq 10cm$ | | |

Table 6.1: Criteria of the track, photon and neutral lists used in this analysis.

The first cuts we impose in our selection process are on event multiplicity:

- $N_{Tracks} = 2$
- $0 \leq N_{Photons} \leq 1$
- $0 \leq N_{Neutrals} \leq 1$

These cuts are implemented in the "*BABAR* Micro" code, before the generation of an ntuple file. This results in a considerable saving of computing resources. After these cuts were applied to the data sample, the resultant ntuple contained slightly more than 10.6 million events. Each additional cut improved the purity of the sample, and reduced it in size. The reduction in the number of events caused by each of the cuts I applied is detailed in Section 6.7 of this chapter. The resulting ntuple contains information on all charged tracks, photons and neutrals in each event satisfying the above criteria.

In Figure 6.1, a plot is shown of the correlation between the transverse momenta ($p_T$) of the two tracks in a small subset of the data. We can see a diagonal band representing events in which the transverse momentum of the two tracks balances quite exactly. We also see events which have more total energy than the beam-beam CM energy, and must be removed.

## 6.3 Cosmic Rays

The events in Figure 6.1, with two tracks both having $p_T$ above 5.5 MeV are physically impossible for the initial beams to produce. They must have an origin outside of the detector, and we identify them as cosmic rays. The events with balanced $p_T$ less than 5.5 GeV are composed of both cosmic rays AND our desired signal events, so we will need to use a measured quantity other than $p_T$ to discriminate between them. We will try to avoid using the track parameters which ultimately determine our quantities of interest $z_0$ and $d_0$.

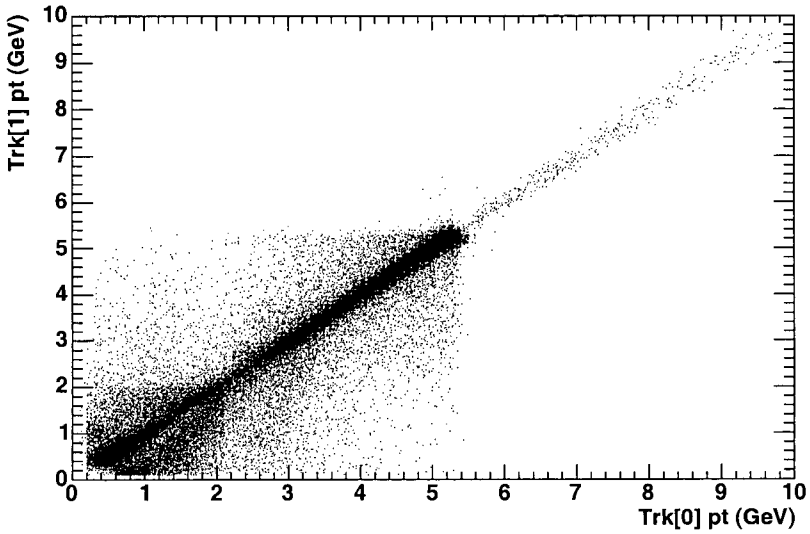


Figure 6.1: Track $p_T$ for all events with exactly two charged tracks.

Cosmic rays traverse the detector more or less vertically, and are reconstructed as two separate tracks, one for each hemisphere. These two tracks have nearly the same values of $d_0$ and $z_0$, and come from locations uniformly distributed throughout the detector. Since we expect cosmic rays to traverse the detector more or less vertically, we can use the angle between the track momentum and the x-y plane, the dip angle, to identify them. This angle is given by the helix parameter $\tan(\lambda)$, as shown in Figure 5.4. This angle will be equal and opposite in sign for the two tracks created by a cosmic ray traversing the detector. Figure 6.2 shows a plot of of the quantity $\sum \tan(\lambda)$ for a small subset of events. The dashed lines in the figure represent a cut of $|\sum \tan(\lambda)| < 0.1$. This cut will remove a relatively small fraction of signal events who happen to have balanced values of $\tan(\lambda)$. Figure 6.3 shows a plot of the transverse momenta of the two tracks with the requirement that $\sum \tan(\lambda) < 0.1$ and Figure 6.4 shows the same quantities with a cut of 0.01. As we expect, the tracks labelled as cosmic rays do indeed have balanced $p_T$, confirming our identification. In the future, I will refer to these two cuts as the Cosmic Ray Loose and Tight cuts.

Finally Figure 6.5 shows track $p_T$ for those events left after applying the Loose cosmic ray cut. This is the cut chosen for the analysis, and after applying it to the initial data sample of 10.6 million events, I was left with 9.85 million events. We can clearly see that nearly all the events with unphysically high transverse momenta ($p_T > 5.5$ GeV) have been removed simply by identifying them as cosmic ray events based on their dip-angle parameters. The few ($< 10$) remaining events with unphysically high $p_T$ will be removed by further cuts.

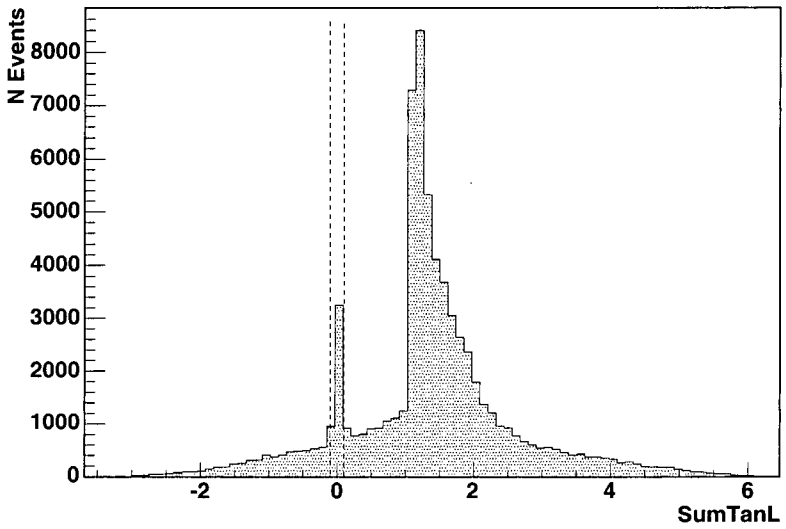


Figure 6.2: The quantity $\sum \tan(\lambda)$ for a small subset of events in the ntuple. The dashed lines indicate a cut of $|\sum \tan(\lambda)| < 0.1$

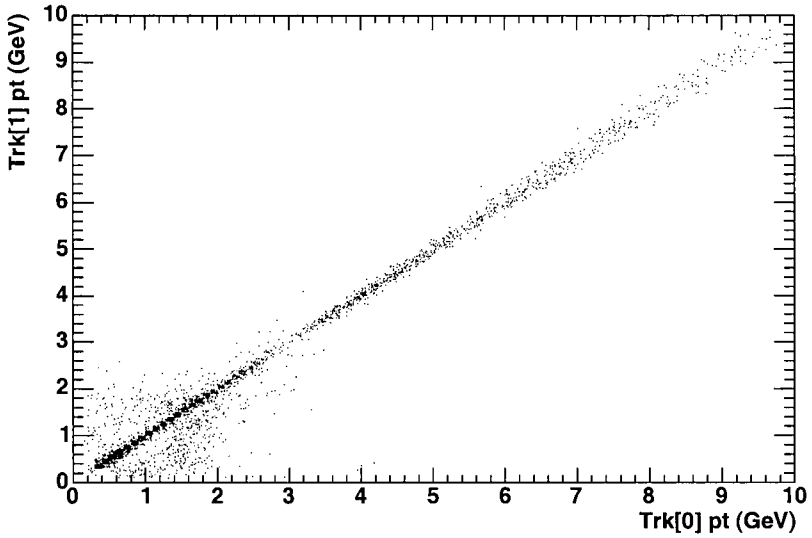


Figure 6.3: Track $p_T$ for events with exactly two charged tracks and passing the Cosmic Ray Loose selection.

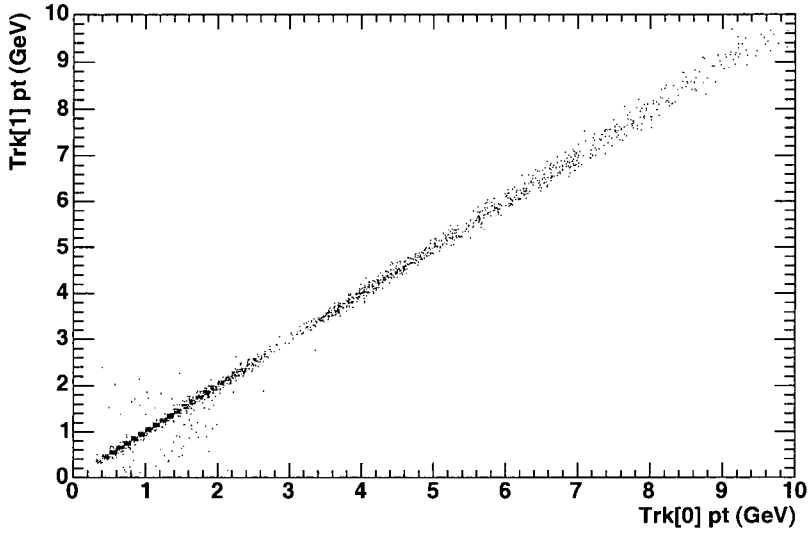


Figure 6.4: Track $p_T$ for events with exactly two charged tracks and passing the Cosmic Ray Tight selection.

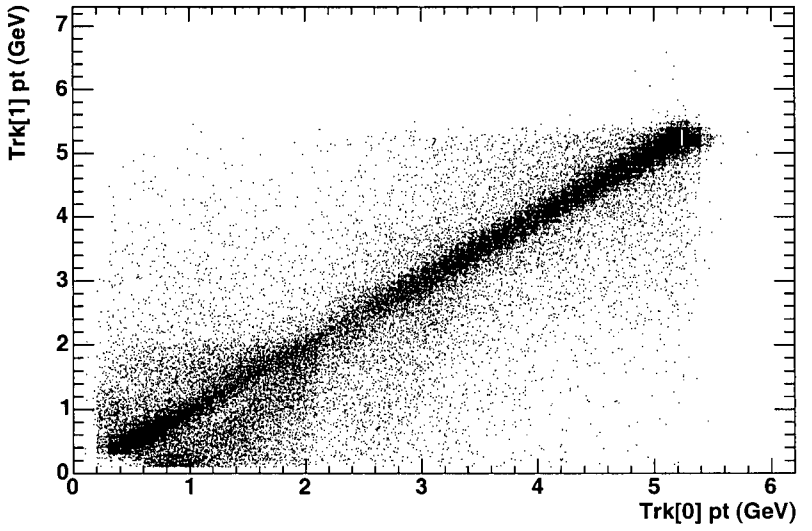


Figure 6.5: Track $p_T$ for events left with exactly two charged tracks after applying the Cosmic Ray Loose cut.

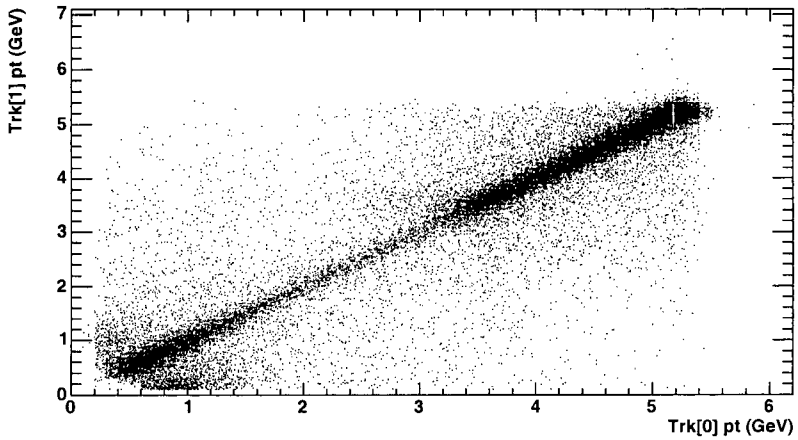


Figure 6.6: Track $p_T$ for events passing requirements for exactly 2 tracks, Cosmic Ray Loose cut, and detector acceptance cuts.

## 6.4 Detector Acceptance

In the next step, I apply a cut to my data sample to remove events which have passed through the very edges of the acceptance of the detector and may not have information associated with them from all of the subsystems. These cuts also remove some events which were very poorly reconstructed. By ensuring that the tracks actually pass through the active regions of the SVT and DCH, we can eliminate these events. The acceptance of the *BABAR* detector in $\phi$ is essentially complete, while the dip angle acceptance is restricted by the openings for the beampipe to be: $-1.0 < \tan(\lambda) < 2.2$. This cut will be referred to as the dip-angle cut. Figure 6.6 shows the effect this cut has on the $p_T$ spectra of a small sample of events. As we can see, many of the events with unbalanced $p_T$ are removed, especially for values of $p_T < 2$ GeV/c. Relatively few $p_T$ balanced events are removed.

## 6.5 Beam-Gas and Beam-Wall Tracks

Electrons or positrons which strike an atom of the residual gas in the vacuum can be measured in the detector. These beam-gas events will be $p_T$-balanced, but will not originate from the beam crossing region. They should have a relatively uniform distribution throughout the volume of the beampipe. We impose a rather loose cut on the reconstructed value of $z_0$ for each of the two tracks, requiring them to be within -3.0 cm $< z_0 <$ 3.0 cm. This cut should include 95% of all signal events, since the length of the beam bunches is roughly 1.0 cm.

The next class of events to be removed resulted from an electron or positron scattering off the material in the walls of the beam-pipe. These beam-wall events must be removed because they didn't originate from the beam crossing. Beam-wall events are clustered at two hot-spots located on the sides of the beam-pipe. By plotting the x-y coordinates of the point-of-closest-approach (POCA) of each track to the beamspot, (see Figure 6.7) we can clearly observe a cluster of tracks at the origin corresponding to the particles created at the beamspot. We also see two sinusoidal arcs in the plot which were created by the particles leaving the hot-spots on the walls. We can calculate the distance $r$ between the track

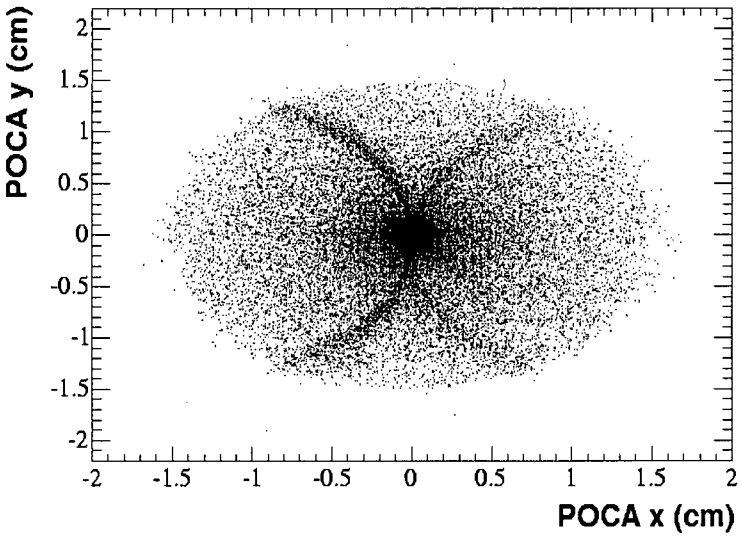


Figure 6.7: Profile of track vertices in x-y plane, the sinusoidal curves are created by events originating from the beam-pipe walls.

origin and the hot spots on the walls:

$$r = |d_0 \pm 2.7 \sin(\phi_0) - Y_{ip} \cos(\phi_0)| \tag{6.1}$$

where $Y_{ip}$ is the nominal y-coordinate of the interaction point, as determined by the *BABAR* offline analysis system (See Section 5.4) and the value of 2.7 cm is the measured distance along the x-axis from the beamspot to the hotspots on the walls. Figure 6.8 shows the distribution of $r$ for one of the hotspots, corresponding to the positive case. We can see a large peak at $r$=2.7 cm, corresponding to the beamspot, and a small peak at $r$=0, corresponding to the hotspot on the wall. A cut requiring $r \geq 0.3$ cm, as indicated by the dashed line, will clearly remove most of the tracks coming from the hotspot. The same distance is calculated individually for each of the two tracks in the event, and for both hotspots, corresponding to the positive and negative signs in Equation 6.1.

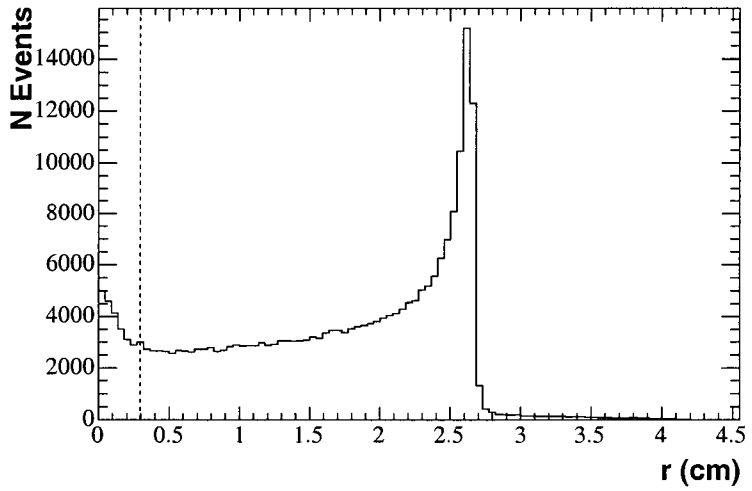


Figure 6.8: Distribution of the distance $r$ between the track origin and one of the hotspots on the wall of the beampipe. A cut at $r \geq 0.3$ cm is indicated by the dashed line.

Figure 6.9 shows the x-y locations of the POCAs for the tracks, after removing the beam-wall events using the cut $r \geq 0.3$ cm: The diffuse background is primarily due to a combination of poorly-reconstructed tracks, i.e. tracks which have been Coulomb scattered through a large angle. Since the objective is to study in detail these distribution tails, we must carefully select any further cuts so that we don't remove any signal.

## 6.6 Transverse Momentum Balance

In this section several different cuts on $p_T$ balance are explored, all using lab-frame quantities. The values of $p_T$ are slightly different in the CM frame because of the relative rotation between the beam axis and detector axis, but the effect should be less than the width of the cuts used here.

Pairs of tracks resulting from the scattering of an electron or a positron by the residual gas in the beampipe will appear to come from the beamspot location in the x-y plane, but will have a flat distribution along the z-axis. These two tracks will not have balanced $p_T$, since one energetic particle is scattering off an atomic electron. They will also not be back-to-back in the x-y plane. By requiring that the two charged tracks are back-to-back in the x-y plane of the detector, we can eliminate many of the beam-gas events from our sample. Figure 6.10 shows a plot of the angle between the two tracks in the x-y plane, $|\Delta\phi - \pi|$. All events in which the tracks are back-to-back in the x-y plane should be located near 0.

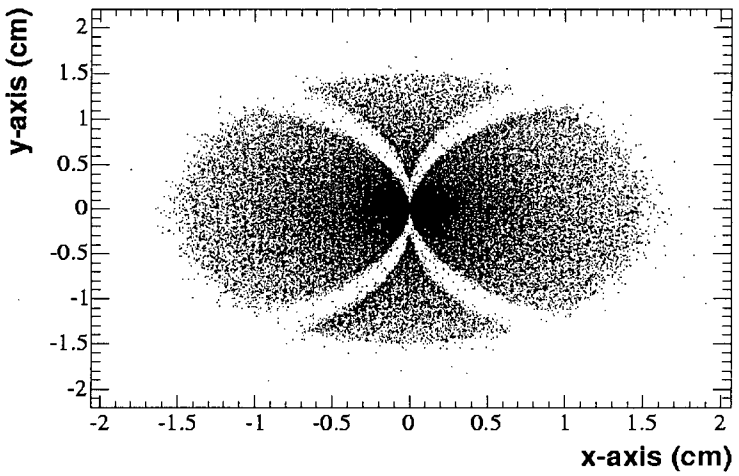


Figure 6.9: Profile of track vertices in x-y plane, after removing events originating from the beam-pipe walls.

The dashed line indicates a cut of $|\Delta\phi - \pi| < 0.2$ radians. Figure 6.11 shows the transverse momenta of the tracks after requiring that $|\Delta\phi - \pi| < 0.2$ for each event. This cut doesn't remove many events in the region where they are $p_T$-balanced, but it does significantly lower the number of events in which one of the two tracks has very low $p_T$ and the other is substantial.

We now make a final requirement based on transverse momentum balance. Based upon inspection of the plot in Figure 6.11, the first choice is a relatively loose cut of $|\Delta p_T| \leq 100$ MeV. This significantly cuts into the signal region, but likely will still include events with an unobserved photon in the final state. This cut removed approximately 40% of the events in the sample. A second, tighter cut was tested on the same sample of data, requiring $|\Delta p_T| \leq 10$ MeV. This cut is stringent enough to eliminate virtually all events with unobserved photons in the final state, but by reducing the number of events in the sample by about 85%, it would severely limit the statistics available for analysis, particularly in the regime of $2 < p_T < 4$ GeV, between the peaks due to the Bhabha and Two-Photon processes. For the rest of the analysis, the looser cut on $p_T$ balance is used.

Two-Photon Events are $p_T$ balanced and have low momenta for the two tracks, while the Bhabhas and muon pairs are also $p_T$ balanced but have higher momenta. A theoretical spectrum for the momentum of muons was shown in Figure 3.5. The lab momentum spectrum for all data tracks is shown in Figure 6.12. The Two-Photon peak is clearly visible just below 1 GeV in the data. Bhabhas and mu-pairs created through the annihilation diagram have momenta equal to one half the initial CM energy of the beams. Initial and

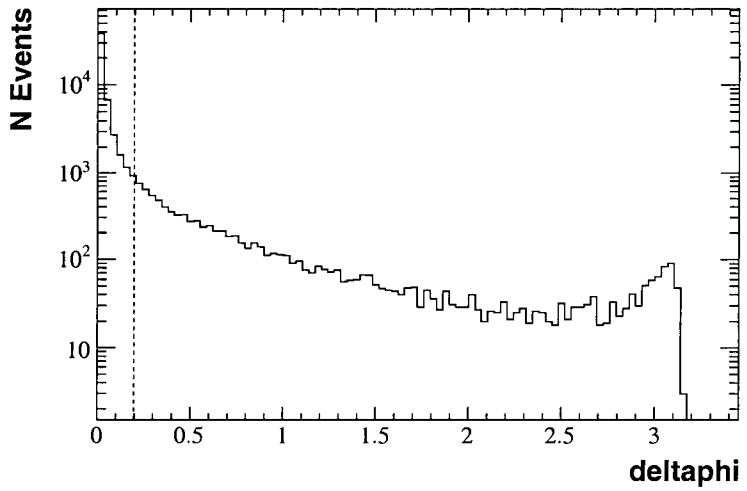


Figure 6.10: Angle between the two tracks in the x-y plane $|\Delta\phi - \pi|$. The dashed line represents a cut at 0.2 radians.

final-state radiation produces a low-energy tail in the spectrum of electron and muon energies, as shown in the theoretical plot Figure 3.2. These events are clearly seen in the region of 3-5 GeV in the data plotted in Figure 6.12.

For the purposes of this analysis, it is not necessary to separate the two contributions in the data; instead we will use samples of Monte-Carlo events produced by both processes. This will allow us to compare data to simulation over the full momentum range from 50 MeV to 5.5 GeV.

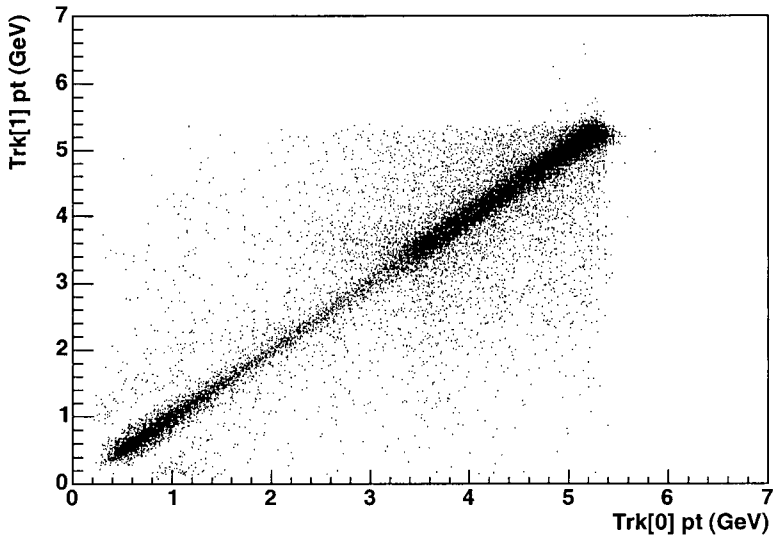


Figure 6.11: Track $p_T$, after requiring they be back-to-back in the x-y plane.

## 6.7 Cut Selection Efficiency

A summary of the selection performance of the applied cuts is listed in Table 6.2. The relative efficiency of each cut is obtained by dividing the number of events

| Cut Description | $N_{events}$ Remaining | Relative Efficiency $\epsilon$ |
|---|---|---|
| AllEvents | 1.0e9 | |
| Only2Trks | 1.05e7 | 0.01 |
| CosmicLoose | 9.85e6 | 0.94 |
| Acceptance | 6.48e6 | 0.66 |
| Hot Spots | 5.87e6 | 0.90 |
| back2back | 5.18e6 | 0.88 |
| pt lab loose | 3.00e6 | 0.58 |
| pt lab tight | 4.50e5 | 0.15 |

Table 6.2: Event selection statistics of the cuts used in this analysis.

passing that cut, by the number of events passing the previous series of cuts. We can see that there are two cuts which remove the most events, the initial requirement on the numbers of different particles in the event, and the tightest requirement on transverse momentum balance. By placing the requirements on particle counts into the first step of my analysis procedure (the creation of an ntuple file), the use of local computing resources is much more efficient. The

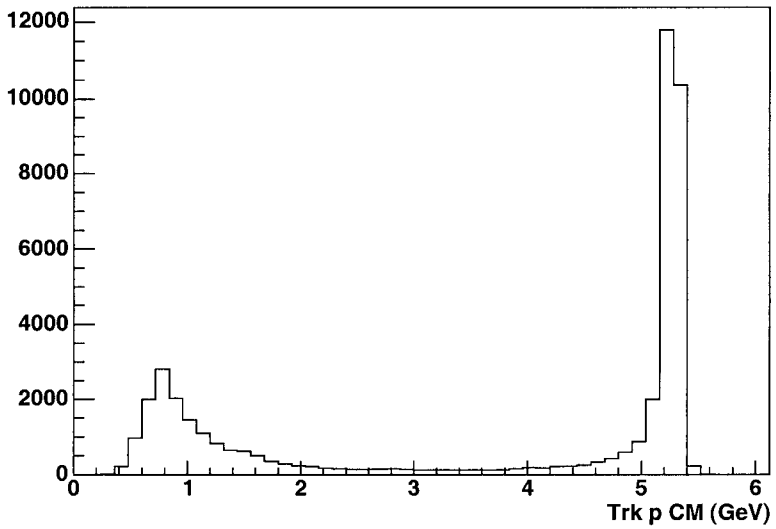


Figure 6.12: Track momenta for all events remaining at loose $p_T$ balance cut.

final requirement on transverse momentum balance is too restrictive at 10 MeV, and so the requirement was set at 100 MeV, to keep a good level of statistics.

## 6.8 The *BABAR* Particle ID System

In the *BABAR* experiment, particle identification is a process which is performed in high-level physics analysis code, once tracks and energy clusters have already been found. These procedures are applied to every track and cluster in an event to give them membership in the various lists of electrons, muons, pions, kaons, protons and photons. For example, a charged track might be found which passes the criteria for membership in both the "loose" and "tight" electron categories, but not for the "very tight" list. This track would be listed as a member of both the "tight" and "loose" electron samples.

In general, the identification schemes use either a series of cuts on directly observed quantities such as $dE/dx$, the lateral moment of an electromagnetic shower in the EMC, the number of layers of the IFR that the candidate traversed, the number of associated photons detected in the DIRC, and the Čerenkov angle measured in the DIRC, or the identification schemes can use a neural network, Fisher discriminant or log-likelihood ratio involving combinations of the above variables. There are also some schemes which combine cuts on variables and the use of neural networks or discriminants.

For my analysis, I have used the standard *BABAR* electron identification

system known as the PidElectronMicroSelector. There are several variations on this selector, eMicroVeryLoose, eMicroLoose, eMicroTight and eMicroVeryTight. The cuts used in each of these selectors are listed in Table 6.3

| Selector | $dE/dx$ | E/p | LAT | Efficiency | MisID |
|---|---|---|---|---|---|
| eMicroVeryLoose | 500-1000 | 0.5-5.0 | -10-10 | $> 98\%$ | $< 20\%$ |
| eMicroLoose | 500-1000 | 0.65-5.0 | -10-10 | $> 97\%$ | $< 10\%$ |
| eMicroTight | 500-1000 | 0.75-1.3 | 0-0.6 | 94-97% | $< 7\%$ |
| eMicroVeryTight | 540-860 | 0.89-1.2 | 0-0.6 | 75-95% | $< 2\%$ |

Table 6.3: Cut-based selectors available in the PidElectronMicroSelector.

The quantities used for the PID selection of electrons are:

- $dE/dx$ - the average energy loss per cm in the drift chamber
- E/p - the energy measured in the calorimeter divided by track momentum
- LAT - the lateral moment of the associated cluster in the calorimeter
- Efficiency - percentage of electrons in control samples passing the selector
- MisID - percentage of hadrons in control samples passing the selector

In the next chapter of this analysis I use the "tight" electron selector. It has very good discrimination against pion contamination and is highly efficient for electrons with moderate momentum. The efficiency drops and MisID fraction rises for very low momentum electrons. In an analysis to determine absolute efficiency, the variations as a function of polar angle and momentum need to be taken into account on a track-by-track basis, but no such corrections are required for the present work.

The muon selectors are applied in an identical way in software, though the criteria used for the cuts are somewhat different. In particular, information from the IFR was not used for electrons, but is crucial for good muon identification. The cuts used in each of the muon selectors are given in Table 6.4.

| Selector | $E_{CAL}$ | $\lambda$ | $\chi^2$ Track | Efficiency | MisID |
|---|---|---|---|---|---|
| muMicroVeryLoose | $< 0.5$ | $> 2$ | NA | 90% | 20% |
| muMicroLoose | $< 0.5$ | $> 2$ | $< 7$ | 85% | 10% |
| muMicroTight | 0.05-0.4 | $> 2.2$ | $< 5$ | 75% | 3% |
| muMicroVeryTight | 0.05-0.4 | $> 2.2$ | $< 5$ | 70% | 2% |

Table 6.4: Cut-based selectors available in the PidMuonMicroSelector.

The quantities used for the PID selection of muons are:

- $E_{CAL}$ - the total calibrated energy deposited in the calorimeter
- $\lambda$ - the number of interaction lengths traversed by the track

- $\chi^2$ Track - The quality of the helix fit to the hits in the IFR
- Efficiency - percentage of muons in control samples passing the selector
- MisID - percentage of hadrons in control samples passing the selector

In the next chapter of this analysis I use the loose muon selector, which has fairly good discrimination against pion and kaon contamination and is very efficient for muons with sufficient momentum. The efficiency drops and MisID fraction rises for muons with momentum less than about 1 GeV. As with the electron ID, absolute efficiency values are not important for the present work.

# Chapter 7

# Analysis

We have now selected the data sample necessary for analysing the track impact parameter resolutions and what remains is to calculate the resolution for each event in this sample. Once the resolution has been calculated it can be fit with an appropriate lineshape. Events can also be binned by relevant quantities like lab momenta and angles, to create a parametrization that is a function of track or event properties.

The resolution of the track impact parameters is made up of three contributions: the geometric resolution of the detector, the Gaussian core of the Multiple Coulomb Scattering distribution, and the tail of the Multiple Coulomb Scattering distribution. The geometric resolution depends only on detector properties and on the angle of the track. The MCS contributions to the resolution depends on both track momentum and polar angle. The errors assigned to each track by the *BABAR* tracking software include the geometric and MCS core contributions, but don't take into account the tail of the MCS distribution.

The calculated values for the difference in the track impact parameters will be divided by the errors assigned by the *BABAR* tracking software. If the software calculation of the tracking errors is correct, then we expect the distribution of differences to have a Gaussian core and tails created by MCS. The core width of the resolution distribution should be about $1\sigma$ as long as the tracking errors are accurate. If the individually assigned tracking errors are larger than they should be, then the width of the core of the resolution distribution will be less than $1\sigma$, and conversely the core will be wider than $1\sigma$ if the assigned tracking errors are too small. In this way, our data can provide a good crosscheck of the tracking system error calculations.

## 7.1 Variable for $d_0$ Studies

When considering the resolution in the x-y plane, the track impact parameter to use is $d_0$. While we know that the tracks originate within the beamspot, the horizontal size of the beam is larger than the resolution for high $p_T$ tracks. We obtain a more precise measure of the track resolution by comparing the $d_0$ values of the two tracks to each other, rather than comparing each separately to the beamspot location. Since $d_0$ is a signed quantity, two tracks which are back-to-back in the x-y plane should have $\Sigma d_0 = 0$. We take the sum of $d_0$ values for the two tracks in the event as our variable of interest.

Our two tracks are not exactly back to back in the $\phi$ angle due to the

beams being rotated relative to the $z$ axis of the detector. This makes $\Sigma d_0$ depend somewhat on the beam position relative to the detector $z$ axis. The default method of determining the track parameters for each charged track uses the detector origin as a reference point. By subtracting the location of the beamspot from the track-impact parameter values we can obtain measurements with respect to the beamspot, rather than the detector origin.

We directly calculate $d_0$ with respect to the beamspot in the following equation:

$$d_0 = (x_{POCA} - x_{ip})\sin(\phi_0) - (y_{POCA} - y_{ip})\cos(\phi_0) \tag{7.1}$$

where $(x_{POCA}, y_{POCA})$ is the point-of-closest approach of the track to the beamspot, in the x-y plane, and $(x_{ip}, y_{ip})$ is the nominal location of the interaction point, or beamspot in the x-y plane for each event.

The error in the quantity $\Sigma d_0$, which we shall denote by $\sigma(\Sigma d_0)$ is just the quadature sum of the $d_0$ errors for each individual track. The track-impact parameter resolution in the x-y plane is now given by the expression: $\frac{\Sigma d_0}{\sigma(\Sigma d_0)}$. By dividing the separation by the error, we can determine whether or not the errors assigned by the *BABAR* tracking software are accurate and attempt to identify any tails of the distribution.

## 7.2 Variable for $z_0$ Studies

If the two tracks were exactly back to back in both $\theta$ and $\phi$, then they would have the same $z_0$ parameter, independently of the detector axes or production point. Two-photon events are typically not back to back in $\theta$. In the *BABAR* experiment, even Bhabha and $\mu$-pair events are not back to back in $\theta$ due to the beam energy asymmetry. So rather than comparing the raw $z_0$ track parameters, we need to find the apparent production point of each track in the beamspot and compare those $z$ coordinate values.

First, I perform a $\chi^2$ fit separately for each of the two tracks to locate its production point within the beampsot. The code for this fit procedure is contained in the default *BABAR* vertexing software known as *GeoKin*. I will denote this production point as $\vec{x}_i$, and it's associated covariance matrix by $\sigma_i$.

Second, in order to determine the best possible value of the production point, $\vec{x'}_i$, I take weighted averages of the two individual production points, using only the x-y information and weights $\mathbf{W_i}$ given by the inverse of the covariance matrices, as in the following equation:

$$\vec{x_1'} = \sigma_1' \left( \mathbf{W_1}\vec{\mathbf{x_1}} + \mathbf{W_2}^{\mathbf{truncated}}\vec{\mathbf{x_2}} \right) \tag{7.2}$$

$$\vec{x_2'} = \sigma_2' \left( \mathbf{W_2}\vec{\mathbf{x_2}} + \mathbf{W_1}^{\mathbf{truncated}}\vec{\mathbf{x_1}} \right) \tag{7.3}$$

where $\mathbf{W_i}^{\mathbf{truncated}}$ is given by $\begin{pmatrix} W_{xx} & W_{xy} & 0 \\ W_{yx} & W_{yy} & 0 \\ 0 & 0 & 0 \end{pmatrix}$ so that the x-y coordinates of the two points are averaged and the z coordinate is recalculated at the position

of the x-y average.

Applying this transformation yields the best possible estimate of the true production points, while still retaining the freedom for drastically different locations along the z axis. Allowing this freedom along the z axis is crucial if we wish to use the results of this study to understand the resolution of the $\Delta t$ distributions in the neutral $B$ mixing analysis.

The covariance matrices for the improved vertex coordinates $\vec{x}_i'$ are now given by the following equations:

$$\sigma_1' = [\mathbf{W_1} + \mathbf{W_2^{truncated}}]^{-1} \tag{7.4}$$
$$\sigma_2' = [\mathbf{W_2} + \mathbf{W_1^{truncated}}]^{-1} \tag{7.5}$$

Finally, we use the elements of the improved covariance matrices $\sigma_i'$ to obtain the errors in the individual tracking parameters $d_0'$ and $z_0'$ through the usual expressions:

$$\sigma_{z_0'} = \sqrt{\sigma_{zz}'^2} \tag{7.6}$$

where ${\sigma_i}'^2$ is the [i,i] element of the covariance matrix $\sigma_i'$. Since the two tracks have independent sources of error, we add their errors in quadrature.

In a similar manner to the expression used for $d_0$, we construct the quantity $\frac{\Delta z_0}{\sigma(\Delta z_0)}$ where the difference is momentum-ordered, i.e. $\Delta z_0 = z_0$(high p) - $z_0$(low p). This is done to eliminate the biases associated with the order in which tracks are recorded in an event. The software algorithm tends to locate tracks in a clockwise fashion, scanning through the $r-\phi$ plane, and systematically identifies smaller track impact parameters before larger ones. The momentum-ordered quantity doesn't suffer from this systematic effect.

The error in the denominator is given by the quadrature sum of the two errors calculated with Equation 7.6. Again, by dividing the difference by the assigned error value, we expect to obtain a central Gaussian distribution of width approximately 1, and wide tails consistent with Multiple Coulomb Scattering.

## 7.3 Variable for Momentum and Angular Dependence

The track impact parameter resolution can be broken down into two components. The first is the geometric resolution of the detector which is independant of track momentum. The other component of track impact parameter resolution is the Multiple Coulomb Scattering which does depend on track momentum. Both of these contributions also depend on the track polar angle, $\theta$. By constructing a new variable which captures the momentum and angular dependence of MCS, we can use it to quantify the amount of scattering and compare the resolution distributions with the Toy MC predictions.

Looking back to Equation 2.3, the core width of the MCS distribution, $\theta_0$, is proportional to $\frac{\sqrt{X/X_0}}{p}$, where $X$ is the thickness of the material traversed,

$X_0$ is the radiation length of the material, and $p$ is the momentum. The thickness of material traversed, $X$, is proportional to $1/\sin\theta$, so the core width $\theta_0$ scales as $1/(p\sin^{1/2}\theta)$. The lever-arm, or distance from the scattering point to the beamspot is $r/\sin\theta$, so the $d_0$ resolution due to MCS is proportional to $1/(p\sin^{3/2}\theta)$. We can also use the relation $p_T = p\sin\theta$ to state that the $d_0$ resolution is proportional to $1/(p_T\sin^{1/2}\theta)$. The same scattering angle changes the measurement of $z_0$ by an additional factor of $1/\sin\theta$, so the $z_0$ resolution due to MCS varies as $1/(p\sin^{5/2}\theta)$ or $1/(p_T\sin^{3/2}\theta)$.

We can now write down the two relations governing the core width of the MCS contribution to the tracking resolutions:

$$\sigma(\Sigma d_0) \propto \frac{1}{p\sin^{3/2}(\theta)} = \frac{1}{p_T\sin^{1/2}(\theta)} \tag{7.7}$$

$$\sigma(\Delta z_0) \propto \frac{1}{p\sin^{5/2}(\theta)} = \frac{1}{p_T\sin^{3/2}(\theta)} \tag{7.8}$$

where $\sigma(\Sigma d_0)$ is the core width of the $\Sigma d_0$ resolution and $\sigma(\Delta z_0)$ is the core width of the $\Delta z_0$ resolution. If we calculate the quantity on the right-hand side for each track, we can estimate the importance of MCS to the resolution distribution.

But since the track impact parameter resolutions are calculated using two tracks, each with a different value of $\theta$, we must modify the above expressions to use the $\theta$ values from each of the two tracks. We define the following two quantities:

$$Q_d^2 = p_{T1}p_{T2}\frac{\sin\theta_1\sin\theta_2}{\sin\theta_1 + \sin\theta_2} \tag{7.9}$$

$$Q_z^2 = p_{T1}p_{T2}\frac{\sin^3\theta_1\sin^3\theta_2}{\sin^3\theta_1 + \sin^3\theta_2} \tag{7.10}$$

where the subscripts 1 and 2 refer to each of the two tracks. We can use $1/Q^2$ as a measure of the importance of the MCS contributions to the resolution in each event. Small values of $1/Q^2$ represent events which are dominated by the geometric resolution and large values of $1/Q^2$ represent events which are dominated by Multiple Coulomb Scattering.

Figure 7.1 shows the excellent results when fitting the functional form to the $\Sigma d_0$ resolution data in the bin of events with $0.0 < 1/Q^2 < 0.1$. This range of $1/Q^2$ corresponds to events with large values of $p_T$ and $\sin\theta$. This is the regime in which Multiple Coulomb Scattering is least important compared to the geometrical resolution. Higher values of $1/Q^2$ correspond to the regime in which MCS dominates the resolution. Figure 7.2 shows the results when fitting the functional form to the $\Sigma d_0$ resolution data in the bin of events with $10 < 1/Q^2 < 50$. The agreement is equally good. Figure 7.3 shows that the same functional form works equally well on the other track impact parameter, $\Delta z_0$, for data events in the low $1/Q^2$ bin; i.e. $\mu$-pairs with $0 < 1/Q^2 < 0.2$. Figure 7.4 shows the same good agreement for $\Delta z_0$ $\mu$-pair data in the high $1/Q^2$

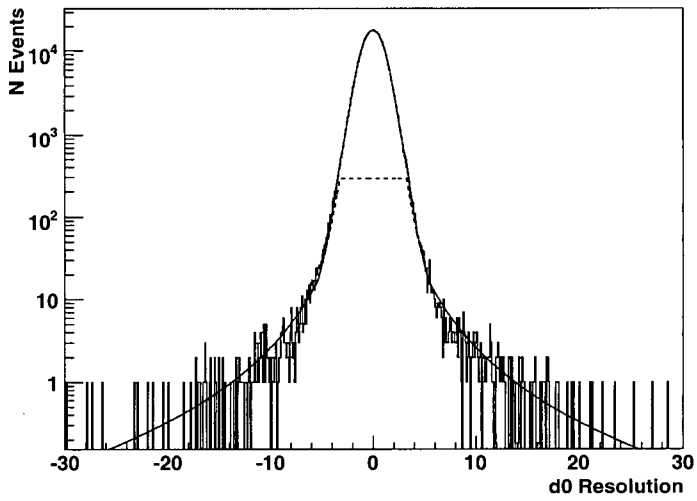


Figure 7.1: Plot of $\Sigma d_0$ resolution for muon pairs in data, with $0.0 < 1/Q^2 < 0.1$. The fit (solid line) is to the function given by Equation 2.4. The dashed line depicts the tail function.

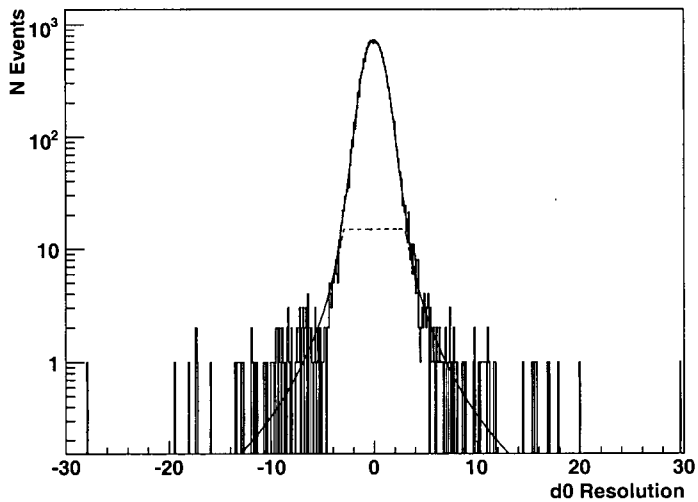


Figure 7.2: Plot of $\Sigma d_0$ resolution for muon pairs in data, with $10 < 1/Q^2 < 50$. The fit (solid line) is to the function given by Equation 2.4. The dashed line depicts the tail function.

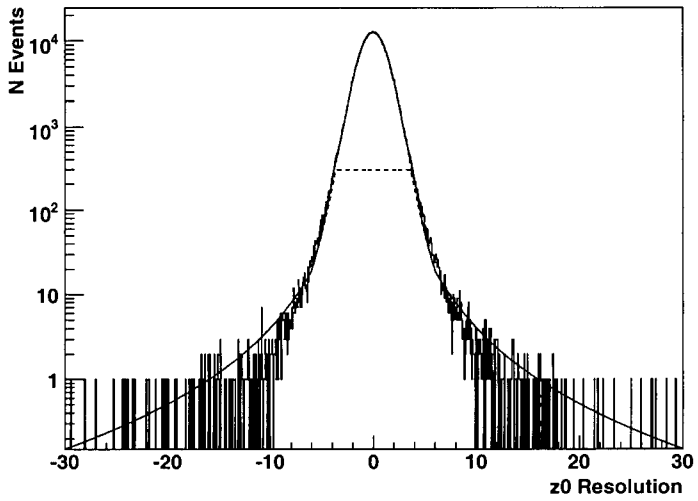


Figure 7.3: Plot of $\Delta z_0$ resolution for muon pairs in data, with $0 < 1/Q^2 < 0.2$. The fit (solid line) is to the function given by Equation 2.4. The dashed line depicts the tail function.

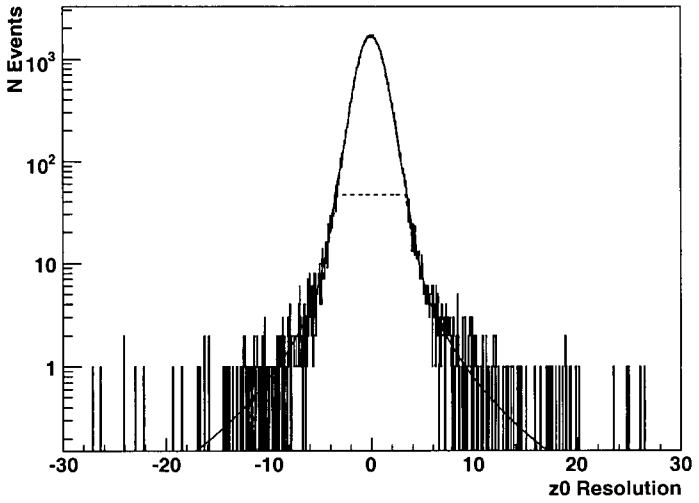


Figure 7.4: Plot of $\Delta z_0$ resolution for muon pairs in data, with $10 < 1/Q^2 < 50$. The fit (solid line) is to the function given by Equation 2.4. The dashed line depicts the tail function.

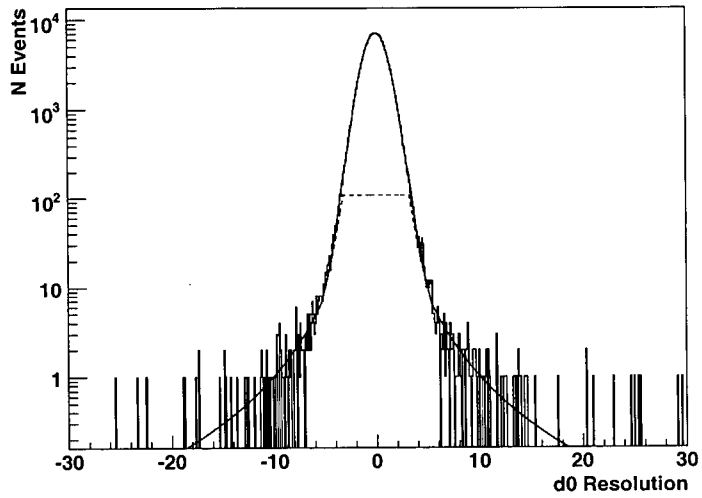


Figure 7.5: Plot of $\Sigma d_0$ resolution for electron pairs in data, with $0.0 < 1/Q^2 < 0.1$. The fit (solid line) is to the function given by Equation 2.4. The dashed line depicts the tail function.

bin, $10 < 1/Q^2 < 50$. We see that the distributions have a very similar shape for both track impact parameters. As one would expect, we also observe that the track impact parameter resolutions in data look nearly identical for both the muons and electrons.

Figure 7.5 is a plot of the fit to $e$-pair $\Sigma d_0$ data in the low $1/Q^2$ ($0.0 < 1/Q^2 < 0.2$) bin. Figure 7.6 is a plot of the fit to $e$-pair $\Sigma d_0$ data in the high $1/Q^2$ ($10 < 1/Q^2 < 50$) bin. Figure 7.7 is a plot of the fit to $e$-pair $\Delta z_0$ data in the low $1/Q^2$ ($0.0 < 1/Q^2 < 0.2$) bin. Figure 7.8 is a plot of the fit to $e$-pair $\Delta z_0$ data in the high $1/Q^2$ ($10 < 1/Q^2 < 50$) bin. The fits for other values of $1/Q^2$, which are not shown here, also gave good quality results for both electron and muon pair data events. By repeating the fitting procedure for several bins of $1/Q^2$, we can tabulate the parameterization as a function of $1/Q^2$.

We perform the same fitting procedure on the GEANT-4 based Monte-Carlo events created with the *BABAR* simulation software as a way to check whether the simulation has the correct treatment of track impact parameter resolution errors and of Multiple Coulomb Scattering. Figure 7.9 is a plot of $\Sigma d_0$ resolution for muon Monte-Carlo events, and Figure 7.10 is a plot of $\Delta z_0$ resolution for the same sample of MC events. They both look reasonable. We can fit them with the same functional form used for the data, and compare the results. Figure 7.11 is a plot of $\Sigma d_0$ resolution in electron-pair Monte-Carlo events: it is qualitatively different from the other plots, and we conclude there is a problem with the simulation of this category of events. The *BABAR* simulation software is a large,

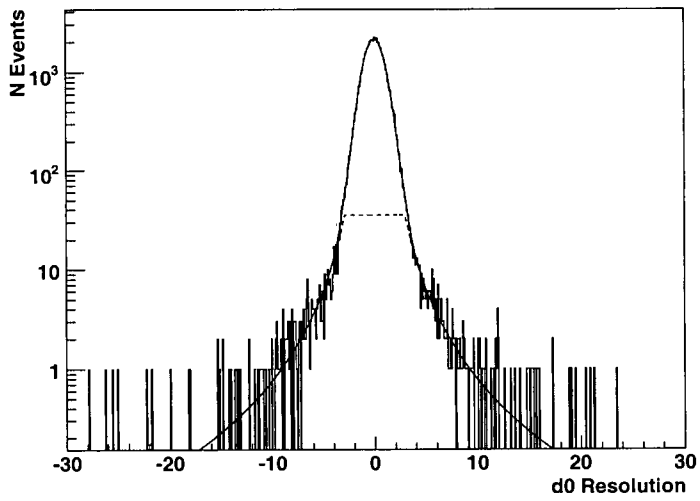


Figure 7.6: Plot of $\Sigma d_0$ resolution for electron pairs in data, with $10 < 1/Q^2 < 50$. The fit (solid line) is to the function given by Equation 2.4. The dashed line depicts the tail function.

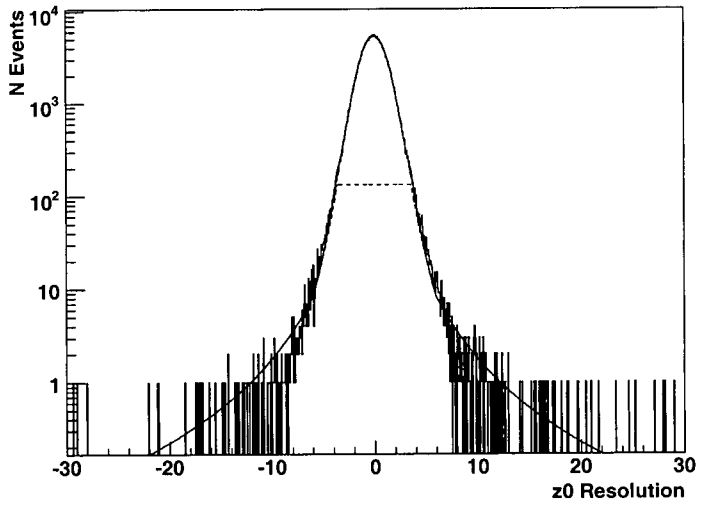


Figure 7.7: Plot of $\Delta z_0$ resolution for electron pairs in data, with $0 < 1/Q^2 < 0.2$. The fit (solid line) is to the function given by Equation 2.4. The dashed line depicts the tail function.

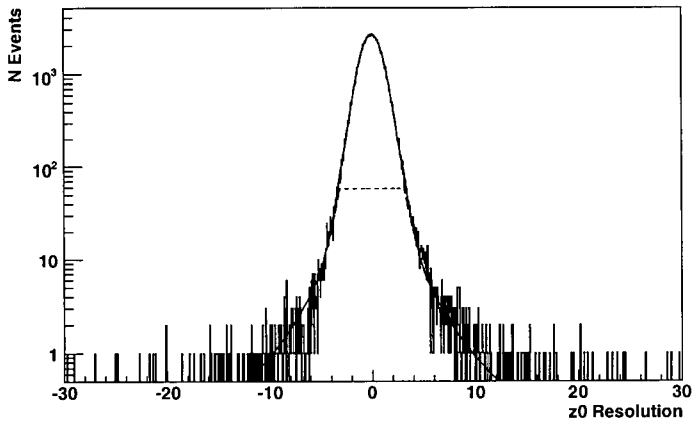


Figure 7.8: Plot of $\Delta z_0$ resolution for electron pairs in data, with $10 < 1/Q^2 < 50$. The fit (solid line) is to the function given by Equation 2.4. The dashed line depicts the tail function.

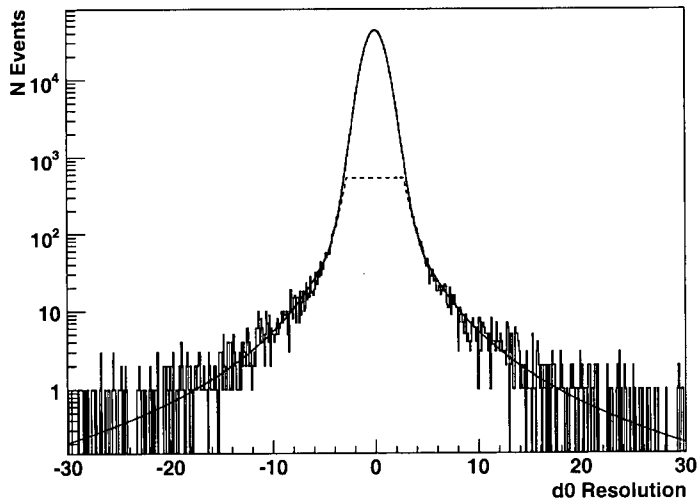


Figure 7.9: Plot of $\Sigma d_0$ resolution for muon pairs in MC simulation, with $0.25 < 1/Q^2 < 0.5$. The fit (solid line) is to the function given by Equation 2.4. The dashed line depicts the tail function.

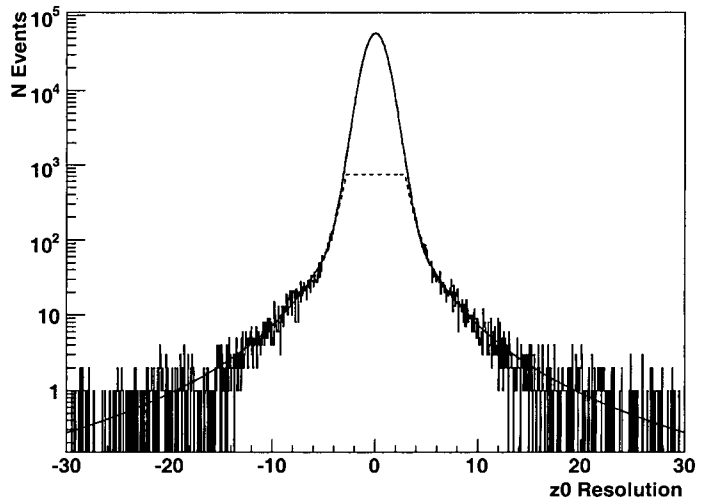


Figure 7.10: Plot of $\Delta z_0$ resolution for muon pairs in MC simulation, with $0.25 < 1/Q^2 < 0.5$. The fit (solid line) is to the function given by Equation 2.4. The dashed line depicts the tail function.

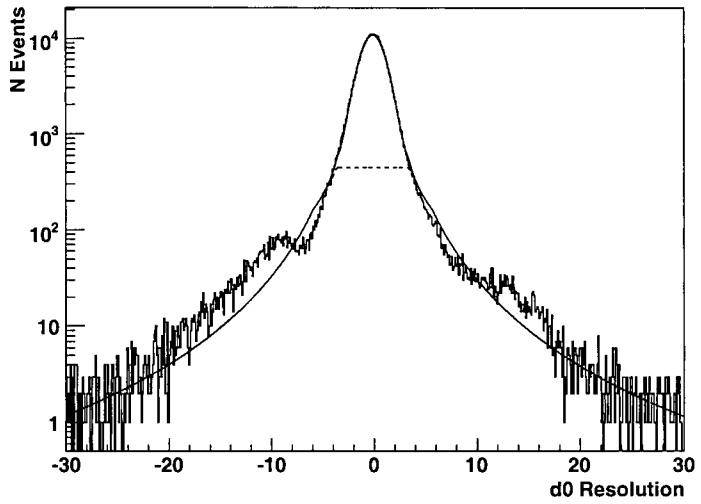


Figure 7.11: Plot of $\Sigma d_0$ resolution for electron pairs in MC simulation, with $0.25 < 1/Q^2 < 0.5$. The fit (solid line) is to the function given by Equation 2.4. The dashed line depicts the tail function.

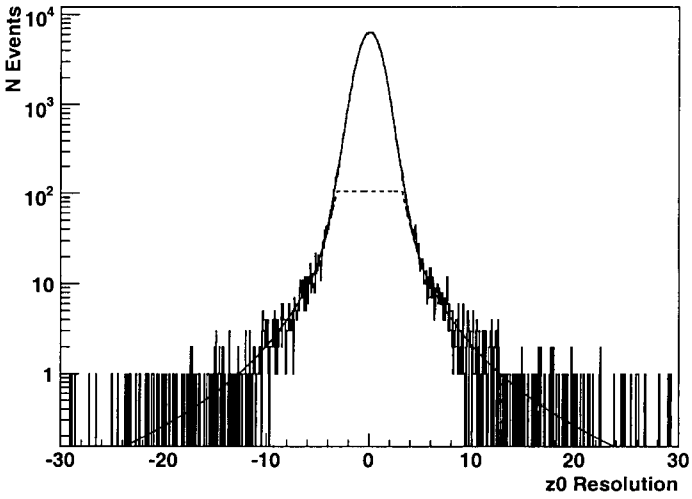


Figure 7.12: Plot of $\Delta z_0$ resolution for electron pairs in MC simulation, with $0.25 < 1/Q^2 < 0.5$. The fit (solid line) is to the function given by Equation 2.4. The dashed line depicts the tail function.

centrally administered project, so it was not possible for this problem to be corrected during the timescale of this analysis. Figure 7.12 is a plot of the $\Delta z_0$ resolution for the same electron MC events. It looks reasonable, but since there is a problem with the $\Sigma d_0$ resolution, we choose not to use the $\Delta z_0$ resolution for MC simulated electrons any further.

## 7.4 Comparison of Data and GEANT MC in Transformed Variable

To examine the agreement in the tails of the distributions more closely is difficult because the number of events in each bin decreases so rapidly as we move away from zero. By examining the inverse-square of the resolution, $u = \left(\frac{\sigma(\Sigma d_0)}{\Sigma d_0}\right)^2$ or $u = \left(\frac{\sigma(\Delta z_0)}{\Delta z_0}\right)^2$, we can look more closely at the agreement between data and Monte-Carlo simulations in the tails of the distributions. This variable transformation has the useful property of mapping the horizontal range from $1\sigma$ out to $\infty$ into the range between 1 and 0. It also rescales the height of the distribution from spanning 4 or more orders of magnitude onto a linear scale. Figure 7.13 is a plot of $u$ for $\mu$-pair $\Sigma d_0$ resolution in Data (open histogram) and Monte-Carlo (shaded histogram) in the the bin with $0.0 < 1/Q^2 < 0.2$. The

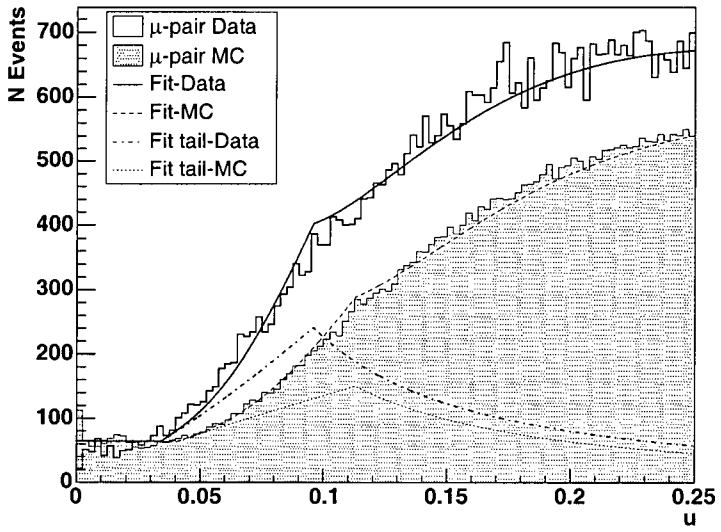


Figure 7.13: Plot of $u$ for muon-pair $\Sigma d_0$ resolution in Data (open histogram) and Monte-Carlo (shaded histogram) in the bin with $0.0 < 1/Q^2 < 0.2$. The solid curve is a transformed fit to $\mu$-pair data. The dashed curve is a transformed fit to $\mu$-pair Monte-Carlo. The dotted curve is the transformed tail function of the $\mu$-pair data, and the dot-dash curve is the transformed tail function of the $\mu$-pair Monte-Carlo.

solid curve is a transformed fit to $\mu$-pair data. The dashed curve is a transformed fit to $\mu$-pair Monte-Carlo. The dotted curve is the transformed tail function of the $\mu$-pair data, and the dot-dash curve is the transformed tail function of the $\mu$-pair Monte-Carlo. We can clearly see kinks in the fit function where the tail function changes slope between the flat inner core and the inner power-law tail, as well as between the inner and outer power-law tails. We also observe that the fit function appears to be slightly higher than the data at the inner breakpoint, and slightly lower than the data on either side of this. From this, we conclude that for this sample of events, the parametrization used to fit the data works quite well, but not perfectly.

The same plot was generated for both track impact parameters, $\Sigma d_0$ and $\Delta z_0$, and for both $\mu$-pairs and $e$-pairs, over the entire observed range of $1/Q^2$. The plots are presented in Appendices A ($\Delta z_0$) and B ($\Sigma d_0$). For $\mu$-pairs there appear to be consistently fewer events in the tails of the Monte-Carlo distributions beyond $2\sigma$ for both track impact parameters. We expect this deficit to result in lowered values for the tail-fraction parameter $f$, when fitting to the Monte Carlo events, compared to the data events.

The $e$-pair Monte-Carlo is clearly flawed in the calculation of the $d_0$ resolution, and we are therefore suspicious of the $z_0$ resolution for those events as well, even though it appears more reasonable than $d_0$. By simply inspecting these plots we determine that the parametrization used to fit the data works well for the $z_0$ track impact parameter, out to roughly $10\sigma$ or $u$=0.01.

## 7.5 Comparison of Data and MC Fitted Parameters

We now present comparisons between experimental data and *BABAR* Monte-Carlo simulation, of the fitted parameters for muon samples, in both $\Sigma d_0$ and $\Delta z_0$ resolution. The comparison is made between our data which contains Bhabhas, $\mu$-pairs and Two-Photon events, and fully-reconstructed Monte-Carlo simulations of Bhabha and $\mu$-pair events. At the time this analysis was performed, only a tiny sample of several thousand Two-Photon events had been generated and reconstructed for *BABAR* analysis. It was decided to use the tails of the Bhabha and $\mu$-pair events in the low $p_T$ regime to perform the analysis. This means that the fits to MC in the range of large $1/Q^2$ have quite large errors. The analysis could be repeated, at a future date, once a larger sample of Two-Photon lepton-pair events has been generated and reconstructed. No comparisons were made of electron-pair data and MC due to the strange shapes of the $\Sigma d_0$ distributions in MC, and the likely errors in the generation of those simulated events.

It is possible to allow all of the parameters in our model to float during the fits, but practical difficulties of convergence are often encountered in that case. If we look only at the most extreme edges of the tails we expect the power to be exactly 3.0 due to the Rutherford differential cross-section, so we fix the power in the outer tail at 3.0. By fixing the inner break-point at 3.0 we effectively assign almost all events more than $3\sigma$ away to be primarily the result of MCS. Finally, based on what we saw by looking at Toy Monte-Carlo, we also choose to fix the breakpoint between the inner and outer power-law tails at 5.0. This fitting procedure allows us to examine the behaviour of the mean, core width, tail fraction, and in inner power-law in more detail. The number of events returned by the fit were always consistent with the true number in the histogram.

Figures 7.14-7.17 depict the fitted parameters versus $1/Q^2$ for the $\Sigma d_0$ resolution in muon-pair events. Figure 7.14 is a plot of the mean of the distribution for muon-pair events in both data and Monte-Carlo. We see that the mean is consistent with zero, for both data and simulations, once $1/Q^2$ is greater than 1.0. This means that for high energy muons, in both the data and Monte-Carlo, the mean of the $\Sigma d_0$ resolution is shifted away from zero by between 2-3%. This effect cannot be explained at the present time.

Figure 7.15 is a plot of the width of the Gaussian core for the $\Sigma d_0$ resolution, in both data and Monte-Carlo muon-pair events. We see the core width steadily

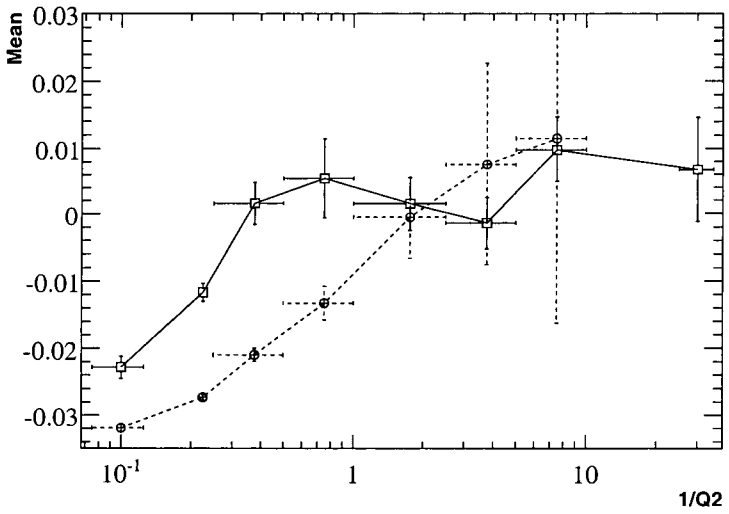


Figure 7.14: Plot of the the mean of $\Sigma d_0$ resolution for muon-pair events in the data (squares), and Monte-Carlo (circles) as a function of $1/Q^2$.

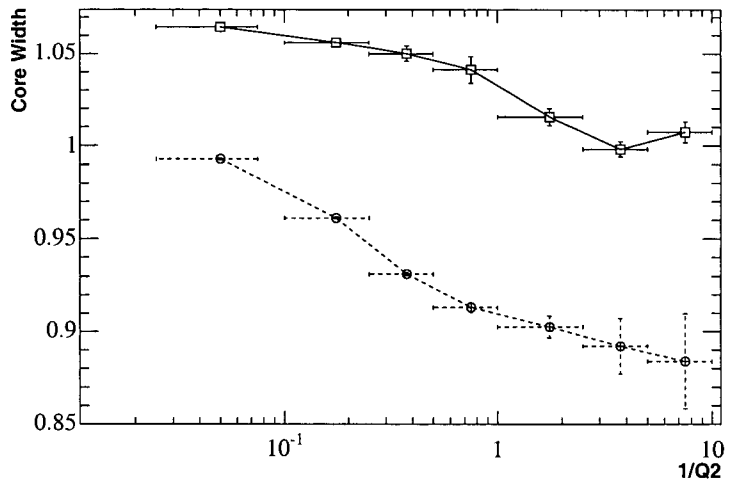


Figure 7.15: Plot of the core width of the $\Sigma d_0$ resolution for muon-pair events in the data (squares), and Monte-Carlo (circles) as a function of $1/Q^2$.

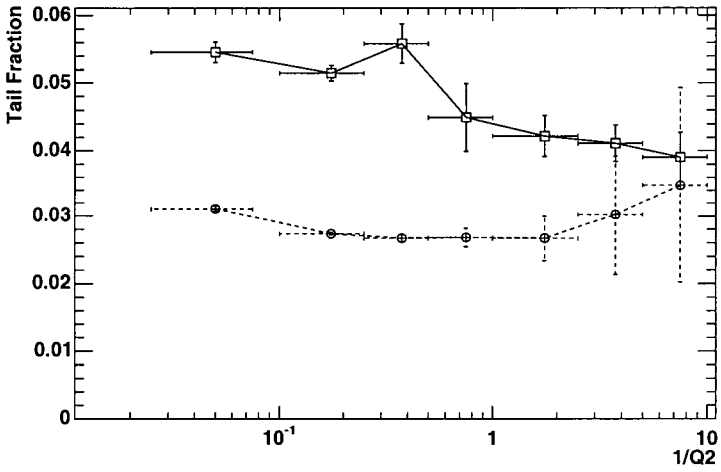


Figure 7.16: Plot of the tail fraction of the $\Sigma d_0$ resolution for muon-pair events in the data (squares), and Monte-Carlo (circles) as a function of $1/Q^2$.

decreasing as the value of $1/Q^2$ increases, in both the data and Monte-Carlo samples. This cannot be directly compared with the results we obtained fitting to Toy Monte-Carlo in Chapter 2. In that case we varied the number of scatters over several orders of magnitude, and kept everything else fixed. Here, we expect to see a fixed value of 1.0 if the tracking errors returned by the *BABAR* software are accurate. For the muon-pairs in the data, the tracking software systematically underestimates the errors by about 6% for low values of $1/Q^2$. At the other end of the spectrum in the data, the tracking software gets the errors about right when $1/Q^2$ is large. In the Monte-Carlo muon-pair events the same general trend occurs, the core width decreases as $1/Q^2$ increases. The Monte-Carlo resolution has a core width consistently less than the data. This means that at low values of $1/Q^2$, the tracking errors are estimated correctly in the Monte-Carlo, but at high values of $1/Q^2$, the tracking errors are overestimated by about 12%.

Figure 7.16 is a plot of the fraction of events assigned to the tail of the $\Sigma d_0$ resolution, in both data and Monte-Carlo muon-pair events. We see that it varies between roughly 3-6%. This is a reasonable figure based on the results of fitting the Toy MC distributions, and indicates that MCS is the dominant source of the tails in the track impact parameter resolutions. The fraction quoted here is significantly larger than the fraction of events which lie outside of the inner $3\sigma$ of the resolution distribution due to the tail function being non-zero and flat beneath the core Gaussian. We cannot simply say that 3-6% of the events will be in the tail of the distribution function, but we can use the parameter $f$ as

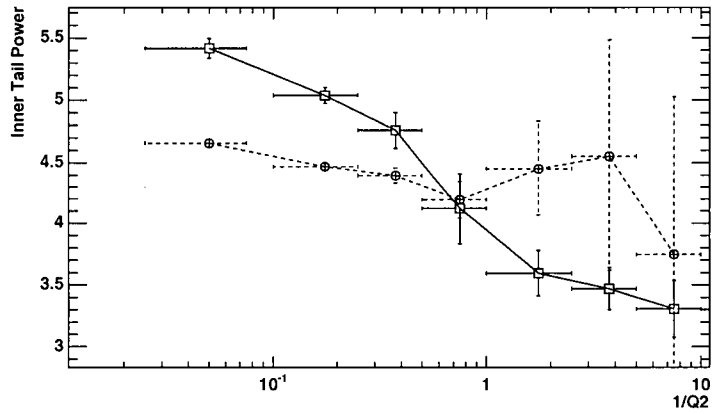


Figure 7.17: Plot of the power in the inner power-law tail ($|p_a|$) of the $\Sigma d_0$ resolution for muon-pair events in the data (squares), and Monte-Carlo (circles) as a function of $1/Q^2$.

a line-shape parameter. We note also that the Monte-Carlo appears to have significantly fewer events in the tail portion for all but the highest values of $1/Q^2$ or the lowest values of track $p_T$. This agrees with our expectation based on an examination of the transformed resolution variables.

Figure 7.17 is a plot of the absolute value of the power $p_a$ in the inner power-law of the tail of the $\Sigma d_0$ resolution, in both data and Monte-Carlo muon-pair events. In the data, the power decreases from about 5.5 down to 3.5 as $1/Q^2$ increases. There is much less change in the power in the Monte-Carlo, it remains between 4.0 and 4.5 over the entire range of $1/Q^2$.

We compare the results of fitting to the data and Monte-Carlo distributions in the other impact parameter, $z_0$, in a similar way. Figures 7.18-7.21 depict the fitted parameters versus $1/Q^2$ for the $\Delta z_0$ resolution in muon-pair events. Figure 7.18 is a plot of the mean of the distribution for muon-pair events in both data and Monte-Carlo. For both data and simulations, the mean of the $\Delta z_0$ resolution distribution is within $\pm 0.08$ from being exactly zero. The mean of the data distribution is generally negative, while that of the MC distribution is always positive. These values are not consistent within two standard deviations.

Figure 7.19 is a plot of the width of the Gaussian core for the $\Delta z_0$ resolution, in both data and Monte-Carlo muon-pair events. In the data muon-pair sample, the core width ranges between 1.07 and 1.21, consistently larger than 1.0. This indicates that the *BABAR* tracking software consistently underestimates the $z_0$ tracking errors by 7-21%. The Monte-Carlo $z_0$ resolution has a core width consistently less than the data. It ranges from approximately 0.93 (in a bin with relatively few events) to 1.08. The tracking errors in $z_0$ are generally underestimated in the Monte-Carlo simulation, except in the vicinity of very

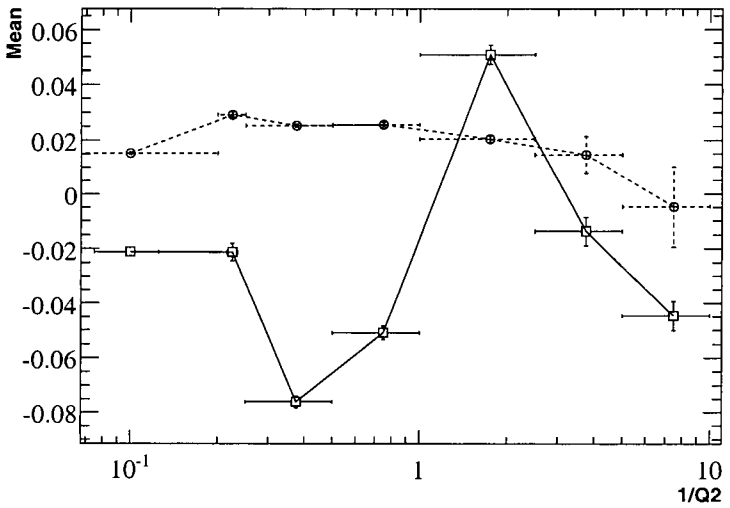


Figure 7.18: Plot of the the mean of $\Delta z_0$ resolution for muon-pair events in the data (squares), and Monte-Carlo (circles) as a function of $1/Q^2$.

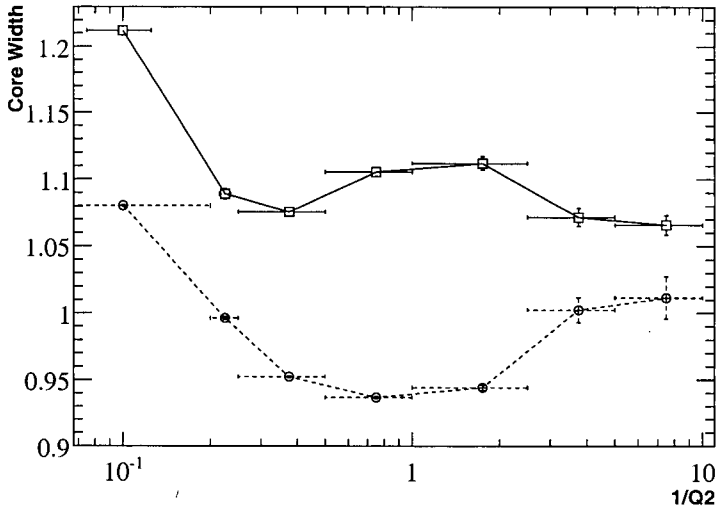


Figure 7.19: Plot of the core width of the $\Delta z_0$ resolution for muon-pair events in the data (squares), and Monte-Carlo (circles) as a function of $1/Q^2$.

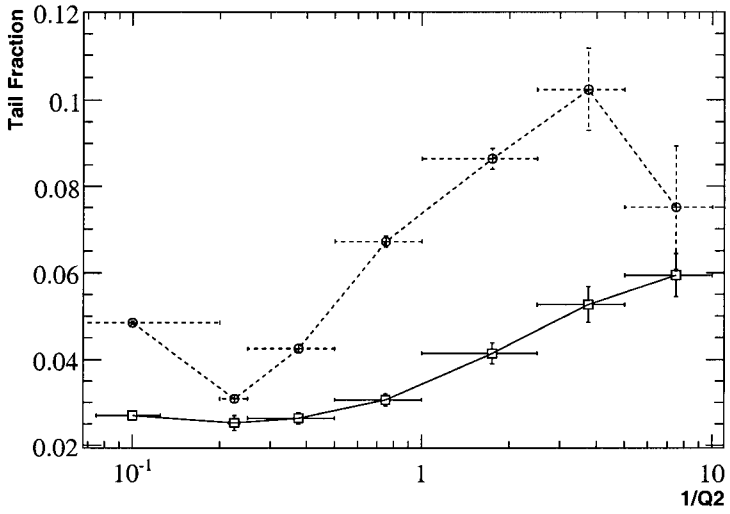


Figure 7.20: Plot of the tail fraction of the $\Delta z_0$ resolution for muon-pair events in the data (squares), and Monte-Carlo (circles) as a function of $1/Q^2$.

small values $1/Q^2$, where they are overestimated.

Figure 7.20 is a plot of the fraction of events assigned to the tail of the $\Delta z_0$ resolution, in both data and Monte-Carlo muon-pair events. We see that the tail fraction parameter $f$ varies between roughly 3-6% for the $z_0$ resolution in the $\mu$-pair data. This is essentially the same fraction seen in the $d_0$ resolution for these events. Again we note that the fraction quoted here is significantly larger than the true fraction of events which lie outside of the inner $3\sigma$ of the resolution distribution, and should mostly be interpreted as a line-shape parameter. We note that the Monte-Carlo appears to have between 3-10% of its events in the tail portion, somewhat higher than the data. This does not agree with what was expected, based on inspection of the transformed resolution variable. This disagreement illustrates the difficulty of interpreting the parameter $f$ as a true representation of the fraction of events in the tail. At the highest values of $1/Q^2$ the data and MC are consistent due to the large MC errors.

Figure 7.21 is a plot of the absolute value of the power $p_a$ in the inner power-law of the tail of the $\Delta z_0$ resolution, for both the data and Monte-Carlo muon-pair events. In the data events, the power ranges between 4.2 and 5.5, decreasing as $1/Q^2$ increases. This is the same behaviour seen in the $\Sigma d_0$ data where the power also decreased as $1/Q^2$ increases. The Monte-Carlo events yield inner tail powers that are generally consistent with the data in the range of larger values of $1/Q^2$, but are significantly smaller for the smallest values of $1/Q^2$. This indicates poor agreement between the tail shape in data and MC

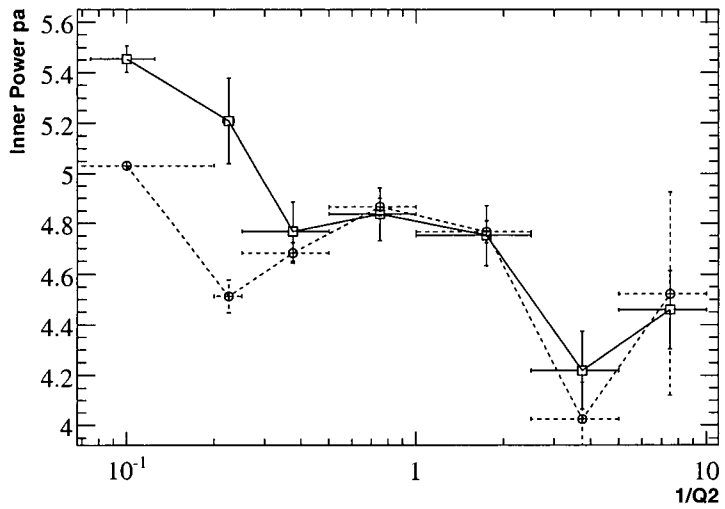


Figure 7.21: Plot of the power in the inner power-law tail ($p_a$) of the $\Delta z_0$ resolution for muon-pair events in the data (squares), and Monte-Carlo (circles) as a function of $1/Q^2$.

for tracks with high $p_T$.

The poor statistics in the Monte-Carlo sample of high $1/Q^2$ events lead to some large errors in the estimated parameters. These estimates should not be considered reliable until samples of Monte Carlo events with large numbers of low $p_T$, Two-Photon $e$-pairs and $\mu$-pairs can be generated.

## 7.6 Correlation of Track Impact Parameters

If the large displacements of events in the track impact parameter resolution tails really are due to Multiple Coulomb Scattering, then the quantities $\Sigma d_0$ and $\Delta z_0$ will be strongly correlated in each event. If an event is in the tail of the distribution of one track-impact parameter, it is more likely to be in the tail of the other as well. This is consistent with what we expect from Multiple Coulomb Scattering, that if a track is deflected through a large angle in the x-y plane, it is likely also deflected through a large angle with respect to the z-axis. Other potential sources of large track impact parameters, such as detector misalignment, or errors in the tracking software, should mostly be uncorrelated in the two track impact parameters.

Figure 7.22 (solid-line histogram) is a plot of the $\Sigma d_0$ resolution for all muon pair events in the data. The dashed-line histogram represents all muon pair events in which $\Delta z_0$ is greater than $3\sigma$. The dotted-line histogram represents

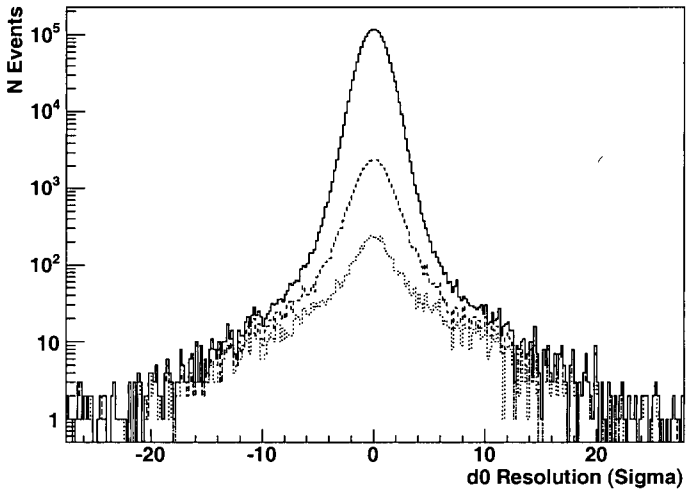


Figure 7.22: Histogram of $\frac{\Sigma d_0}{\sigma(\Sigma d_0)}$ for muon events in data. Solid line is all muon-pair events. Dashed line is muon-pair events with $\Delta z_0 > 3\sigma$. Dotted line is muon-pair events with $\Delta z_0 > 5\sigma$.

all muon pair events in which $\Delta z_0$ is greater than $5\sigma$. We can see that as we cut out the events in the core of the $\Delta z_0$ distribution we also remove events from the core of the $\Sigma d_0$ distribution. Equivalently, events which are in the tails of the $\Delta z_0$ distribution are much more likely to also be in the tails of the $\Sigma d_0$ distribution.

Figure 7.23 (solid-line histogram) is a plot of the $\Delta z_0$ resolution for all muon pair events in the data. Again, the dashed-line histogram represents all muon pair events in which $\Sigma d_0$ is greater than $3\sigma$. The dotted-line histogram represents all muon pair events in which $\Sigma d_0$ is greater than $5\sigma$. We see that as we cut out the events in the core of the $\Sigma d_0$ distribution we also remove events from the core of the $\Delta z_0$ distribution. Events which are in the tails of the $\Sigma d_0$ distribution are more likely to also be in the tails of the $\Delta z_0$ distribution. These correlations provide additional evidence to suggest that the tails of the track impact parameter resolutions really are due to Multiple Coulomb Scattering.

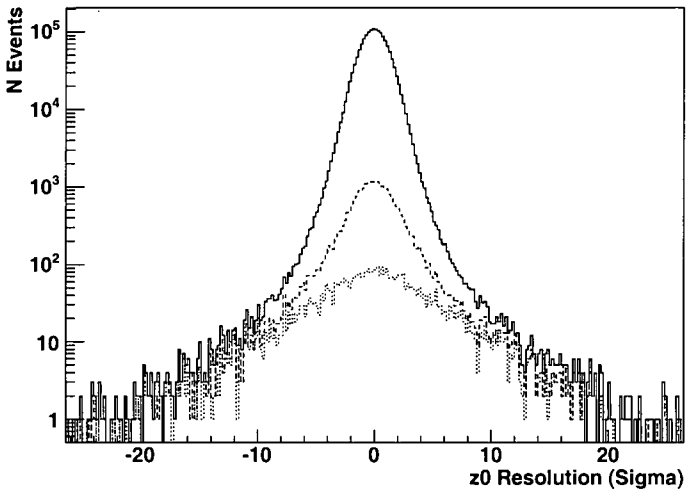


Figure 7.23: Histogram of $\frac{\Delta z_0}{\sigma(\Delta z_0)}$ for muon events in data. Solid line is all muon-pair events. Dashed line is muon-pair events with $\Sigma d_0 > 3\sigma$. Dotted line is muon-pair events with $\Sigma d_0 > 5\sigma$.

# Chapter 8

# Conclusions

## 8.1 Results of this Study

After analyzing the resolution distributions of the track impact parameters for both data and Monte-Carlo events of the *BABAR* experiment, there are a number of conclusions we can draw.

Firstly, the parameterization of Equation 2.4, using two power-law tails, describes Toy Monte-Carlo events generated with the Multiple Coulomb Scattering distribution quite well. The same parameterization also describes both of the track impact parameter distributions in *BABAR* data quite well out to values of approximately $20\sigma$. The Monte-Carlo simulated sample of muon-pair events is fit well by the functional form of Equation 2.4 for both track impact parameters. The sample of Monte-Carlo simulated electron-pair events has a distinctly different distribution in the $\Sigma d_0$ parameter, and we therefore conclude that there was an error somewhere in the simulation process for those events.

For both data and Monte-Carlo muon-pair events, the width of the Gaussian core determined through fitting to Equation 2.4 is within 20% percent of being equal to the errors assigned by the *BABAR* tracking software. This demonstrates that the tracking software correctly models the contributions to the resolution from detector geometry and from the Gaussian core of the Multiple Coulomb Scattering distribution to the level of 20%, but that significant corrections between 5-20% need to be applied to improve the level of agreement. The core widths in the experimental data and Monte-Carlo simulations are also systematically different, with the Monte-Carlo distributions tending to have smaller widths by about 10% in both $d_0$ and $z_0$.

Results of the fits to track impact parameter resolution show that the power-law of the inner tail ranges between $x^{-3.5}$ and $x^{-5.5}$. This agrees reasonably well with what we observed in the MCS Toy Monte-Carlo. In Section 2.3 we saw that by fitting Equation 2.4 to Toy Monte-Carlo events generated with the exact multiple scattering distribution we obtained inner tail powers $p_a$ of approximately 4.0. This leads us to conclude that the tails in the track impact parameter resolution are dominated by Multiple Coulomb Scattering and not by effects like misalignment or failures of the track-fitting software. This also provides a physical motivation for the shape of our parameterization.

We found additional evidence that the tails are mostly due to Multiple Coulomb Scattering by looking at the distribution of $\Sigma d_0$ for events with large values of $\Delta z_0$ and vice-versa. When tracks are widely displaced in one parameter due to a large angle scatter, we expect them on average to be widely

displaced in the other parameter as well. Other possible sources of poor impact parameter agreement, like misalignment or software errors should be largely independent in $d_0$ and $z_0$. We do indeed see a strong correlation between the two track impact parameters, as shown in Section 7.6. This correlation provides more direct evidence that MCS is the dominant source of the tails in the track impact parameter resolution.

## 8.2 Future Plans

Any experiments which require highly precise knowledge of track impact parameter resolution will need to take into account the effects of Multiple Coulomb Scattering, especially the long tails. The parameterization developed here may prove useful for other researchers, but most importantly it helps increase awareness of the importance of Multiple Coulomb Scattering for track impact parameter resolutions, by including the tails explicitly in the formulation.

More directly, we see the possibility of using these results in several time-dependent analyses in the *BABAR* collaboration. We may be able use this technique to reduce the systematic uncertainty due to the track impact parameter resolution in future measurements of neutral $B$-mixing at *BABAR* . The additional effects of particle misidentification and confusion between direct and cascade leptons also contribute to the $\Delta t$ resolution. This means any improvement in the measured results will ultimately depend on the relative importance of the tracking compared to the other contributions to the $\Delta t$ resolution.

In order to use the results more directly in other studies, it would be more convenient if the analysis were performed in terms of the variables $p_T$ and $\theta$ for the tracks, rather than the combined quantity $1/Q^2$. This would make it easier to apply the parameterization on a track-by-track basis to the chosen data set. The problem with this approach is that the two tracks don't have the same values of $\theta$, and we don't know which one of the two to blame for a large-angle scatter. The results of this thesis will have to be used in a less direct manner.

Finally, it is clear that there are many areas in which the track impact parameter resolution in *BABAR* Monte-Carlo simulations doesn't agree with the actual data. These discrepancies will need to be either resolved or compensated for if the extensive collection of Monte-Carlo generated events is going to be used in future studies sensitive to the tails of the track impact parameter resolution.

# Appendix A

# Tail Shapes in DATA and MC Simulation: $\Delta z_0$

By using the transformed variable $u = 1/x^2$, where $x$ is either $\frac{\Sigma d_0}{\sigma(\Sigma d_0)}$ or $\frac{\Delta z_0}{\sigma(\Delta z_0)}$, we can more closely compare the shape of the tails between the data and Monte-Carlo events. Figures A.1-A.8 are plots of the quantity $u = \left(\frac{\sigma(\Delta z_0)}{\Delta z_0}\right)^2$ for the muon-selected data and Monte-Carlo events. Figures A.9-A.14 are plots of the same quantity $u$ for the electron-selected data and Monte-Carlo events. There are insufficient electron Monte-Carlo events at higher values of $1/Q^2$ to make comparison possible. We don't trust the resolution for the electron MC in $z_0$ because it is obviously incorrect in $d_0$. See Section 7.5 for more details.

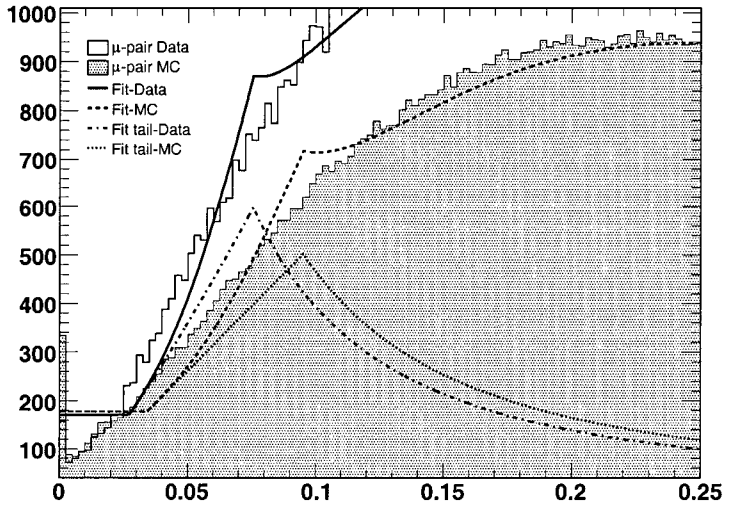


Figure A.1: Plot of $u = \left(\frac{\sigma(\Delta z_0)}{\Delta z_0}\right)^2$ for $\mu$-pair events with $0 < 1/Q^2 < 0.2$.

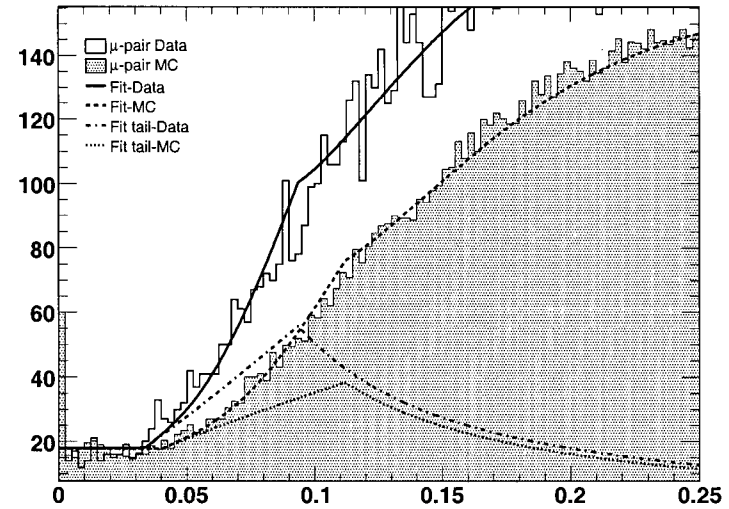


Figure A.2: Plot of $u = \left(\frac{\sigma(\Delta z_0)}{\Delta z_0}\right)^2$ for $\mu$-pair events with $0.2 < 1/Q^2 < 0.25$.

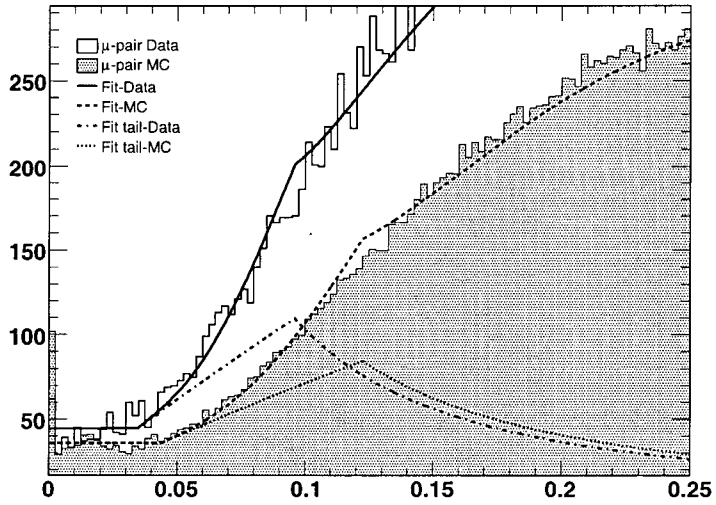


Figure A.3: Plot of $u = \left(\frac{\sigma(\Delta z_0)}{\Delta z_0}\right)^2$ for $\mu$-pair events with $0.25 < 1/Q^2 < 0.5$.

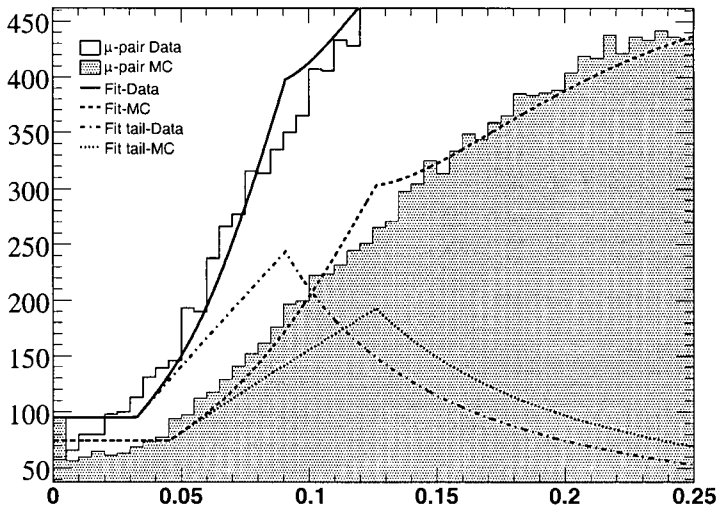


Figure A.4: Plot of $u = \left(\frac{\sigma(\Delta z_0)}{\Delta z_0}\right)^2$ for $\mu$-pair events with $0.5 < 1/Q^2 < 1.0$.

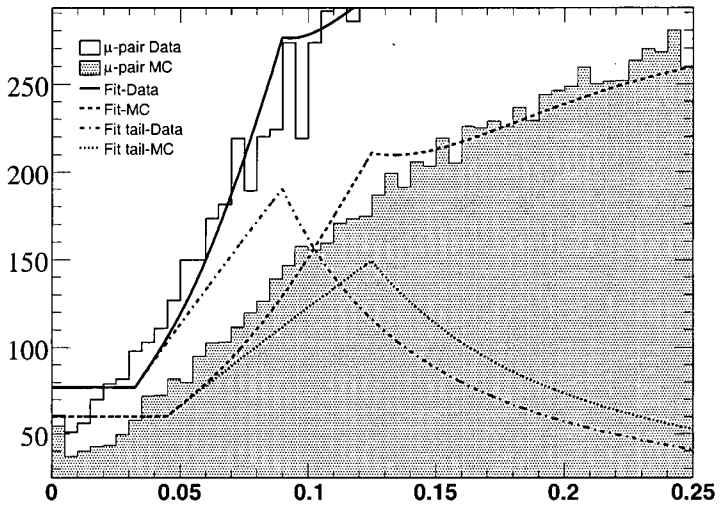


Figure A.5: Plot of $u = \left(\frac{\sigma(\Delta z_0)}{\Delta z_0}\right)^2$ for $\mu$-pair events with $1.0 < 1/Q^2 < 2.5$.

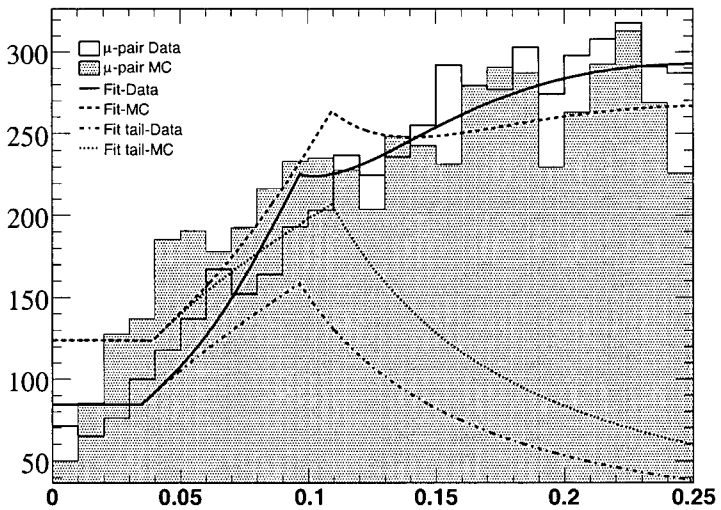


Figure A.6: Plot of $u = \left(\frac{\sigma(\Delta z_0)}{\Delta z_0}\right)^2$ for $\mu$-pair events with $2.5 < 1/Q^2 < 5.0$.

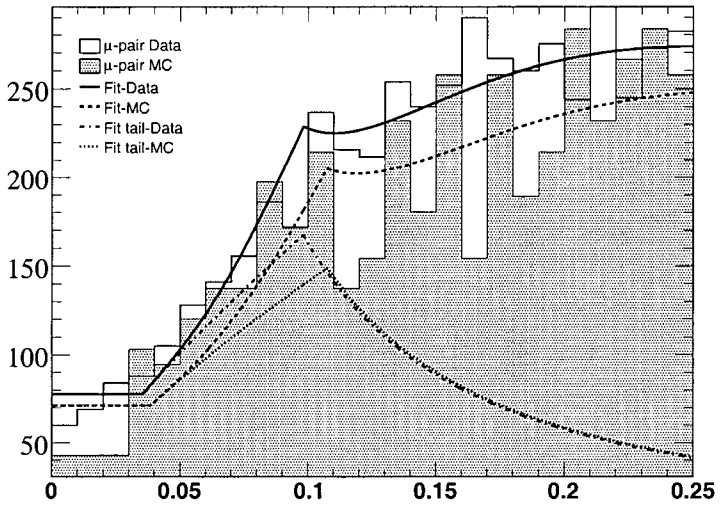


Figure A.7: Plot of $u = \left(\frac{\sigma(\Delta z_0)}{\Delta z_0}\right)^2$ for $\mu$-pair events with $5 < 1/Q^2 < 10$.

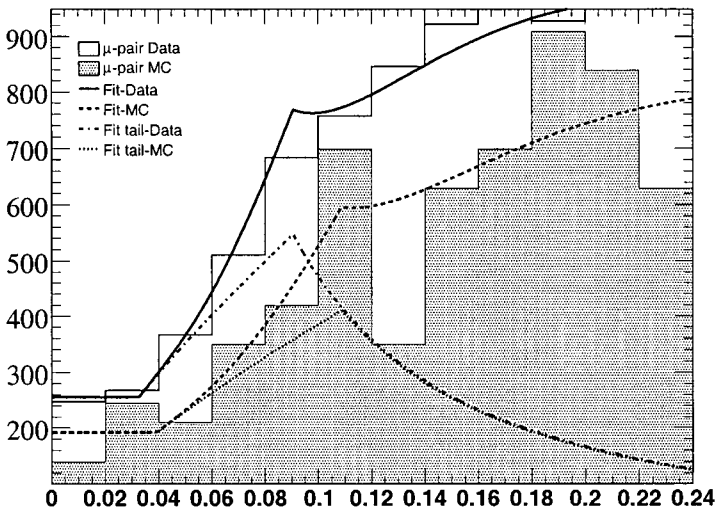


Figure A.8: Plot of $u = \left(\frac{\sigma(\Delta z_0)}{\Delta z_0}\right)^2$ for $\mu$-pair events with $10 < 1/Q^2 < 50$.

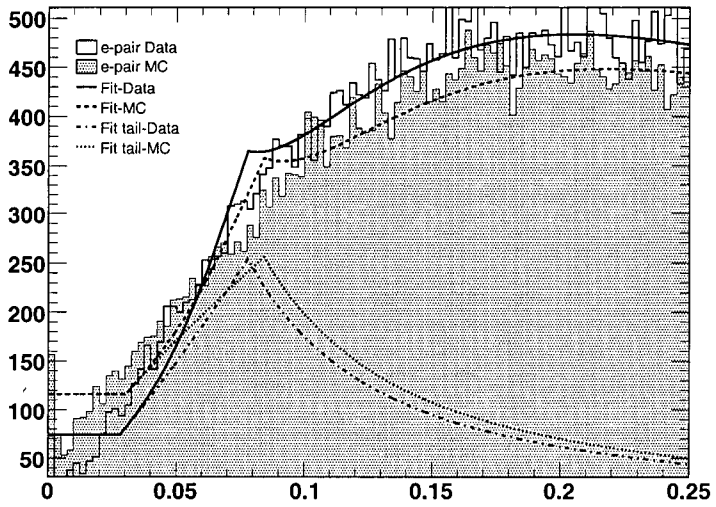


Figure A.9: Plot of $u = \left(\frac{\sigma(\Delta z_0)}{\Delta z_0}\right)^2$ for $e$-pair events with $0 < 1/Q^2 < 0.2$.

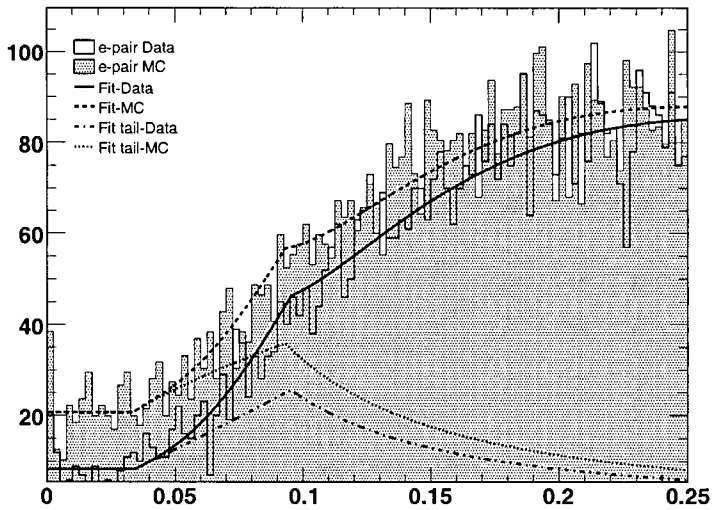


Figure A.10: Plot of $u = \left(\frac{\sigma(\Delta z_0)}{\Delta z_0}\right)^2$ for $e$-pair events with $0.2 < 1/Q^2 < 0.25$.

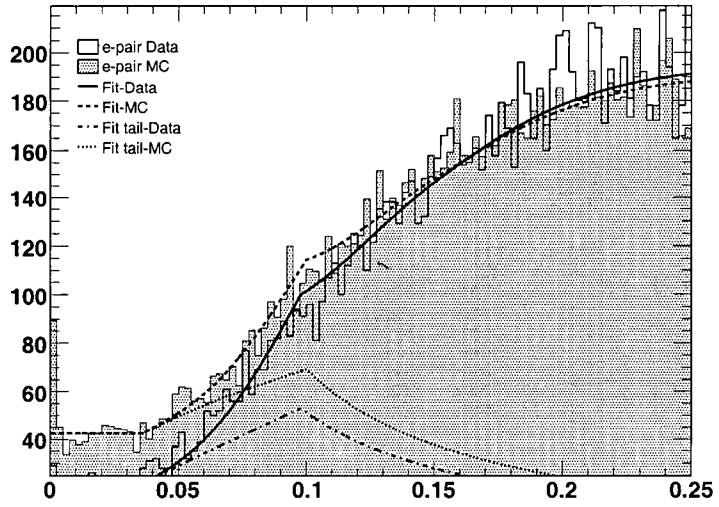


Figure A.11: Plot of $u = \left(\frac{\sigma(\Delta z_0)}{\Delta z_0}\right)^2$ for $e$-pair events with $0.25 < 1/Q^2 < 0.5$.

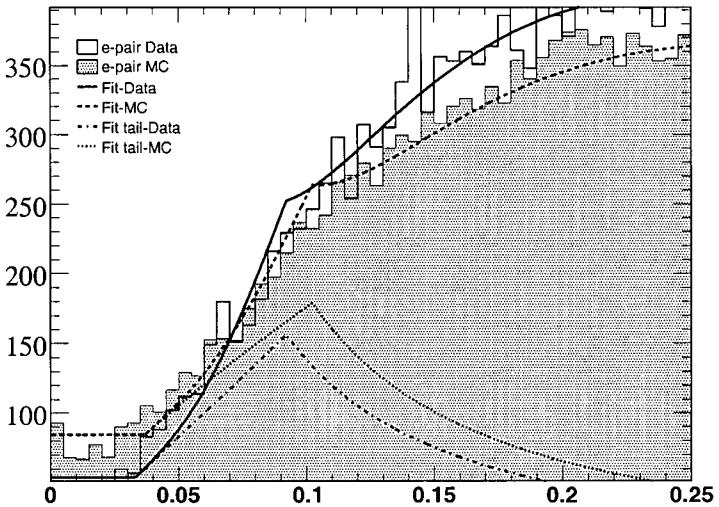


Figure A.12: Plot of $u = \left(\frac{\sigma(\Delta z_0)}{\Delta z_0}\right)^2$ for $e$-pair events with $0.5 < 1/Q^2 < 1.0$.

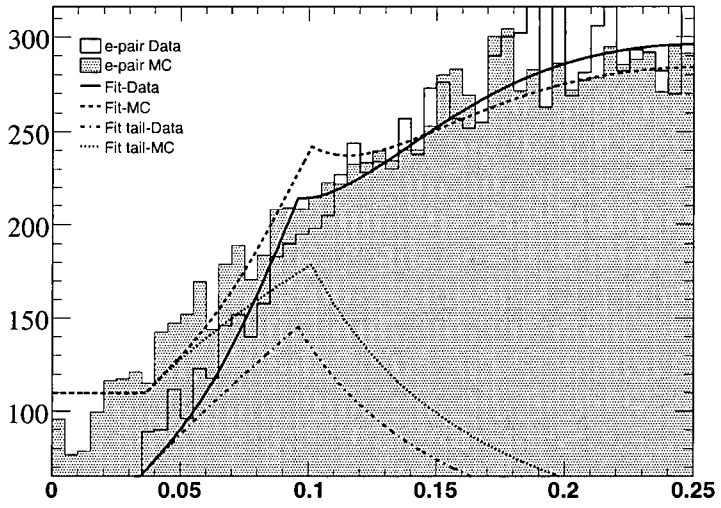


Figure A.13: Plot of $u = \left(\frac{\sigma(\Delta z_0)}{\Delta z_0}\right)^2$ for $e$-pair events with $1.0 < 1/Q^2 < 2.5$.

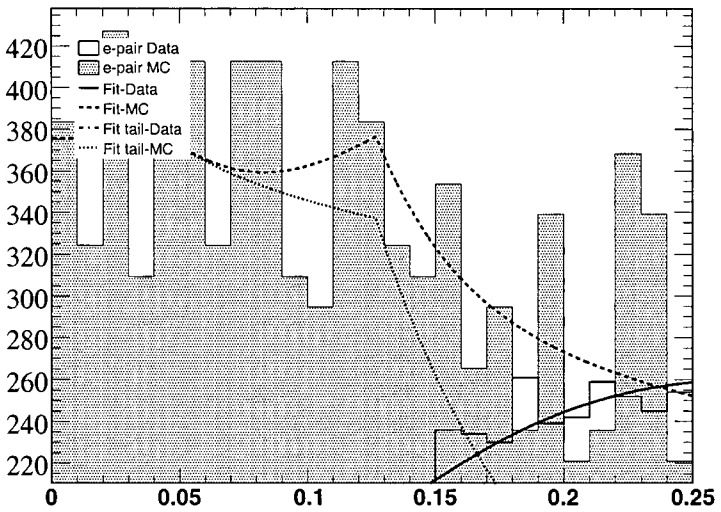


Figure A.14: Plot of $u = \left(\frac{\sigma(\Delta z_0)}{\Delta z_0}\right)^2$ for $e$-pair events with $2.5 < 1/Q^2 < 5.0$.

# Appendix B

# Tail Shapes in DATA and MC Simulation: $\Sigma d_0$

Figures B.1-B.8 are plots of the quantity $u = \left(\frac{\sigma(\Sigma d_0)}{\Sigma d_0}\right)^2$ for the $\mu$-pair data and Monte-Carlo events. Figures B.9-B.14 are plots of the same quantity $u$ for the $e$-pair data and Monte-Carlo events. Note that the $e$-pair MC resolution is obviously seriously flawed. The large spike at $u$=0 corresponds to a significant surplus of MC events at greater than $10\sigma$.

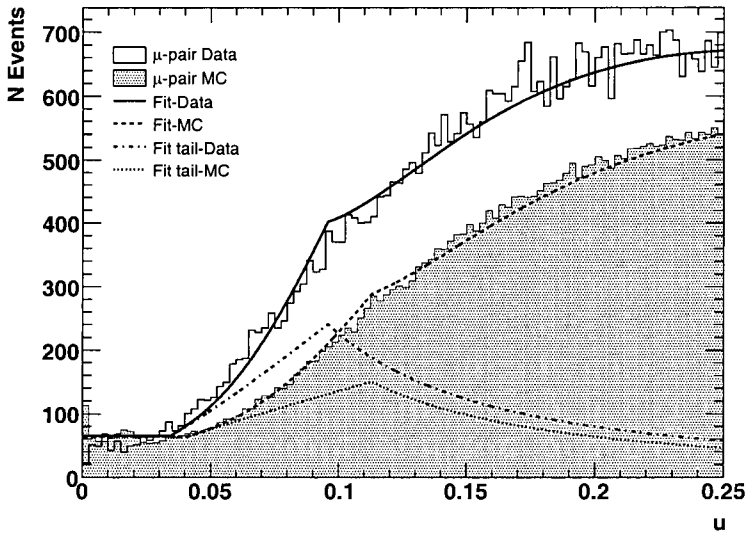


Figure B.1: Plot of $u = \left(\frac{\sigma(\Sigma d_0)}{\Sigma d_0}\right)^2$ for $\mu$-pair events with $0 < 1/Q^2 < 0.1$.

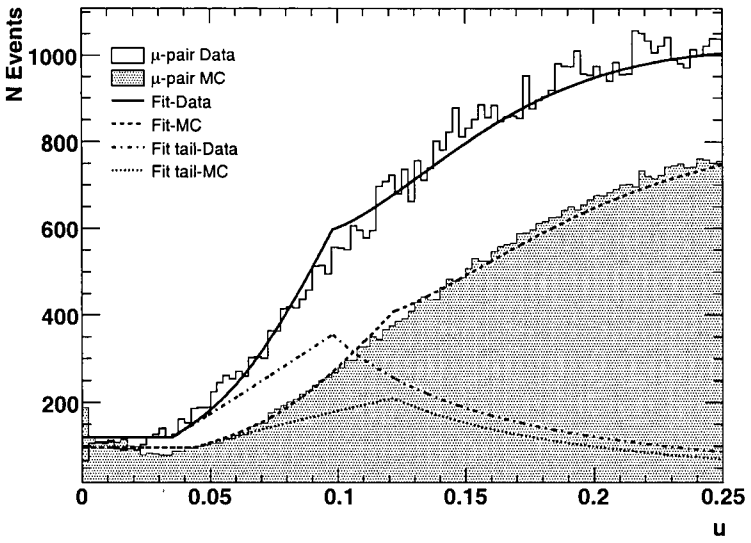


Figure B.2: Plot of $u = \left(\frac{\sigma(\Sigma d_0)}{\Sigma d_0}\right)^2$ for $\mu$-pair events with $0.1 < 1/Q^2 < 0.25$.

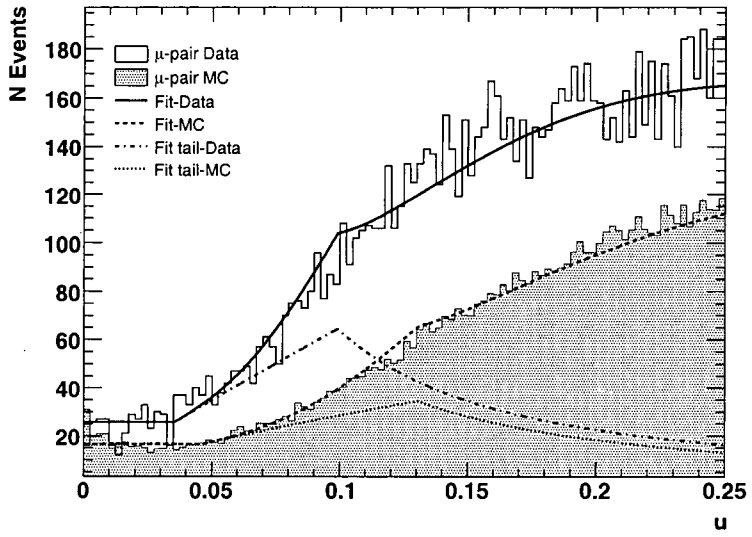


Figure B.3: Plot of $u = \left(\frac{\sigma(\Sigma d_0)}{\Sigma d_0}\right)^2$ for $\mu$-pair events with $0.25 < 1/Q^2 < 0.5$.

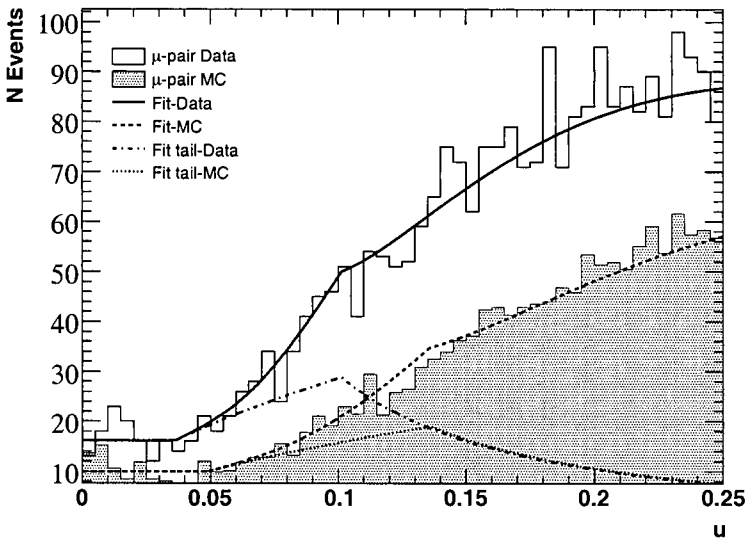


Figure B.4: Plot of $u = \left(\frac{\sigma(\Sigma d_0)}{\Sigma d_0}\right)^2$ for $\mu$-pair events with $0.5 < 1/Q^2 < 1.0$.

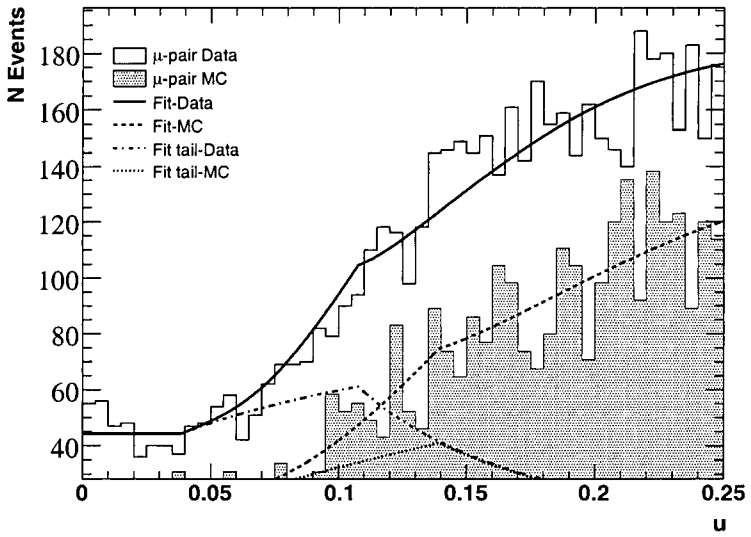


Figure B.5: Plot of $u = \left(\frac{\sigma(\Sigma d_0)}{\Sigma d_0}\right)^2$ for $\mu$-pair events with $1.0 < 1/Q^2 < 2.5$.

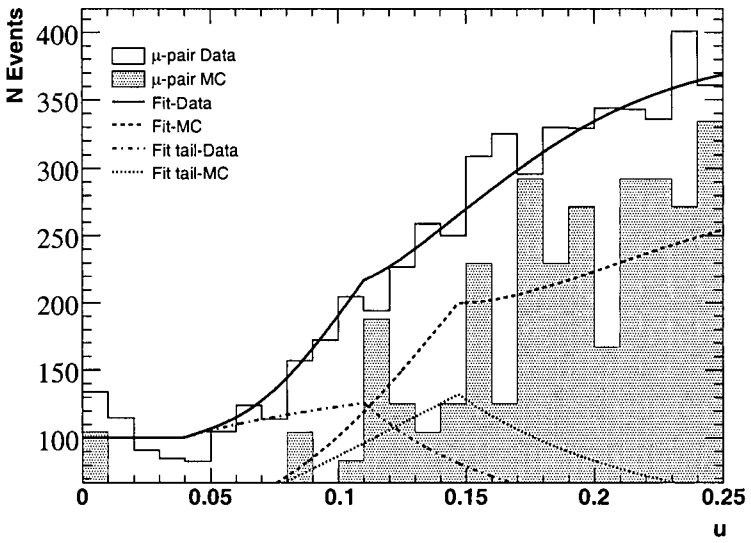


Figure B.6: Plot of $u = \left(\frac{\sigma(\Sigma d_0)}{\Sigma d_0}\right)^2$ for $\mu$-pair events with $2.5 < 1/Q^2 < 5.0$.

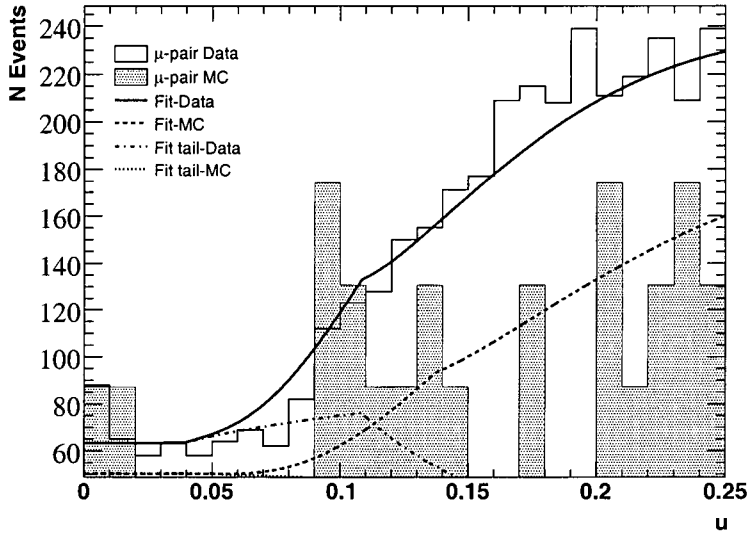


Figure B.7: Plot of $u = \left(\frac{\sigma(\Sigma d_0)}{\Sigma d_0}\right)^2$ for $\mu$-pair events with $5 < 1/Q^2 < 10$.

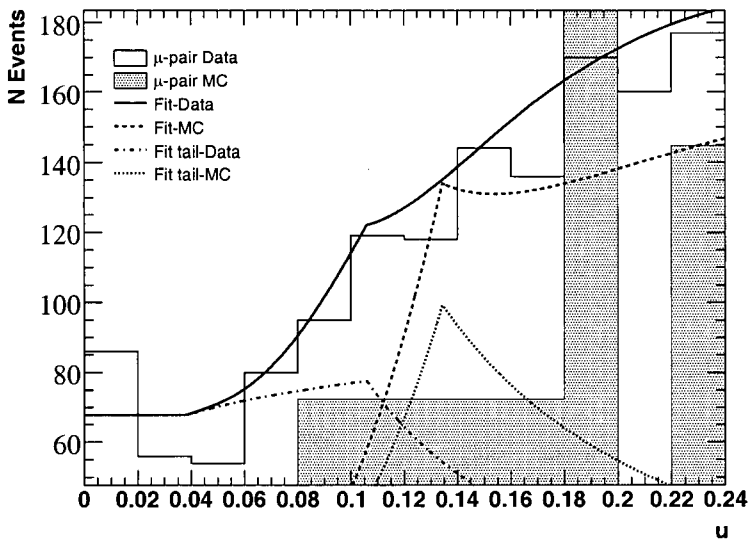


Figure B.8: Plot of $u = \left(\frac{\sigma(\Sigma d_0)}{\Sigma d_0}\right)^2$ for $\mu$-pair events with $10 < 1/Q^2 < 50$.

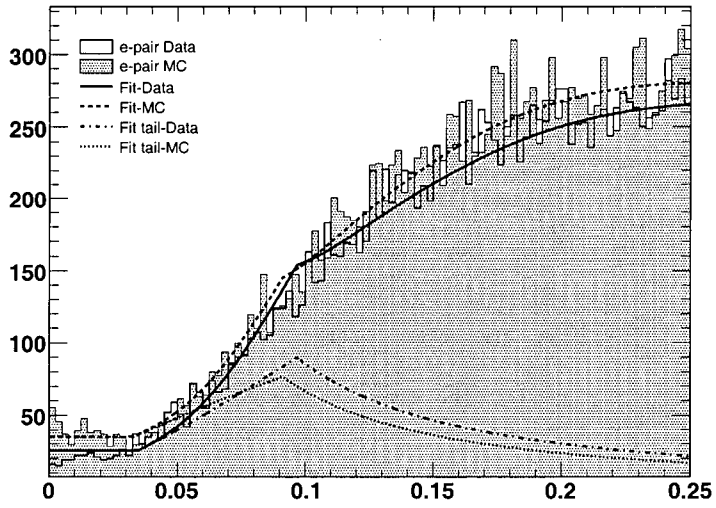


Figure B.9: Plot of $u = \left(\frac{\sigma(\Sigma d_0)}{\Sigma d_0}\right)^2$ for $e$-pair events with $0 < 1/Q^2 < 0.1$.

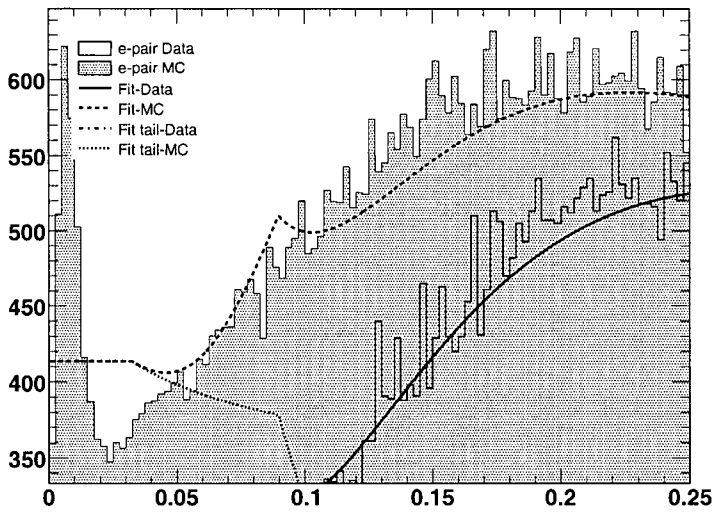


Figure B.10: Plot of $u = \left(\frac{\sigma(\Sigma d_0)}{\Sigma d_0}\right)^2$ for $e$-pair events with $0.1 < 1/Q^2 < 0.25$.

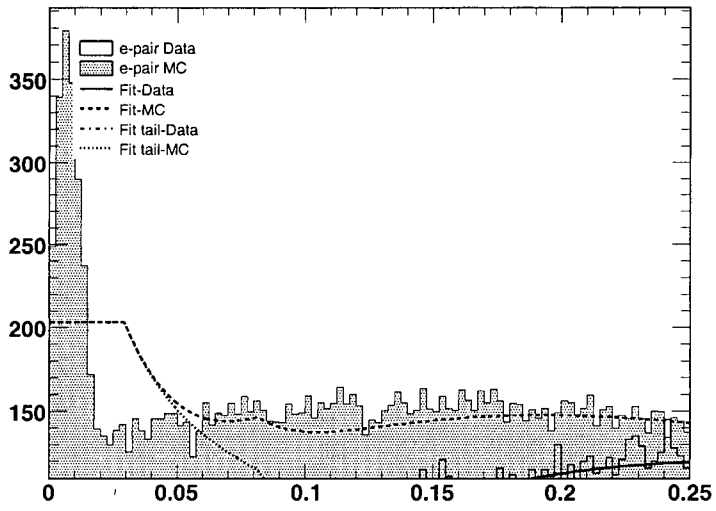


Figure B.11: Plot of $u = \left(\frac{\sigma(\Sigma d_0)}{\Sigma d_0}\right)^2$ for $e$-pair events with $0.25 < 1/Q^2 < 0.5$.

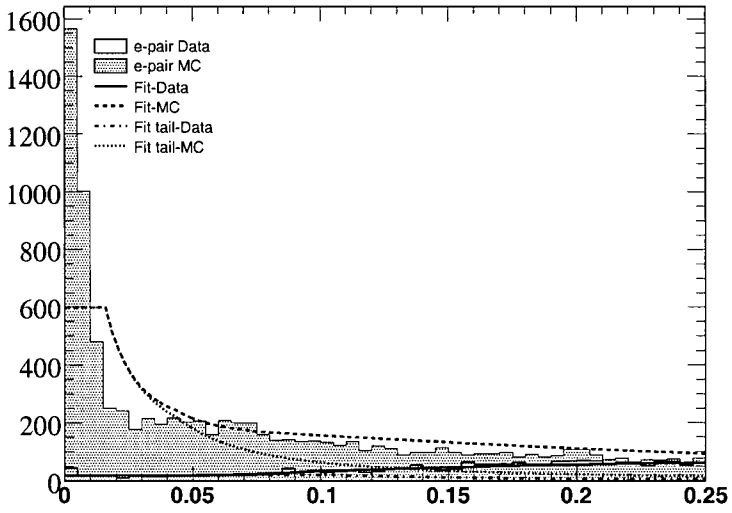


Figure B.12: Plot of $u = \left(\frac{\sigma(\Sigma d_0)}{\Sigma d_0}\right)^2$ for $e$-pair events with $0.5 < 1/Q^2 < 1.0$.

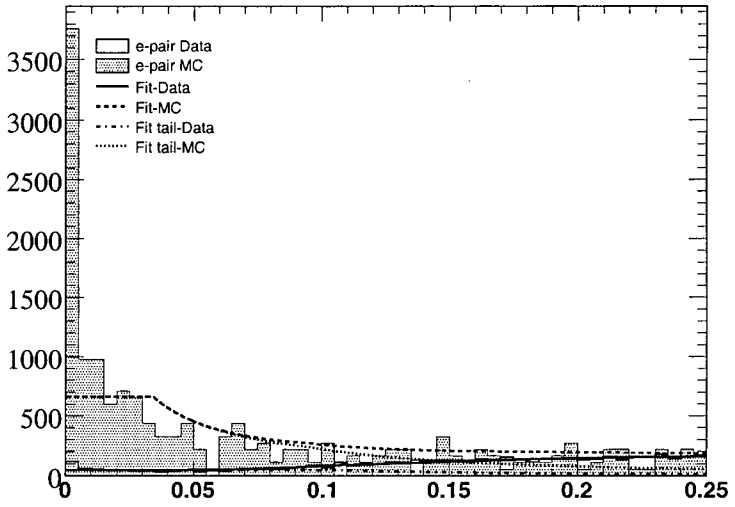


Figure B.13: Plot of $u = \left(\frac{\sigma(\Sigma d_0)}{\Sigma d_0}\right)^2$ for $e$-pair events with $1.0 < 1/Q^2 < 2.5$.

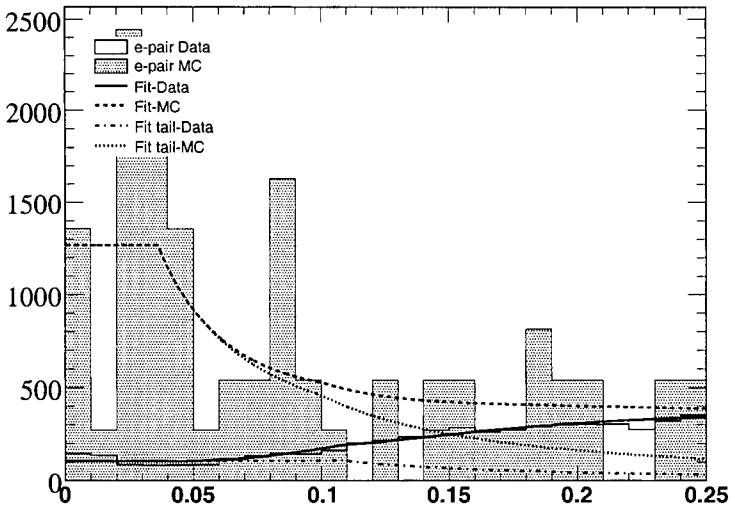


Figure B.14: Plot of $u = \left(\frac{\sigma(\Sigma d_0)}{\Sigma d_0}\right)^2$ for $e$-pair events with $2.5 < 1/Q^2 < 5.0$.

# Bibliography


[1] P. F. Harrison, H. R. . Quinn [*BABAR* Collaboration], "The BaBar physics book: Physics at an asymmetric B factory," SLAC-R-0504, (1998)

[2] E. Noether, Nachr. v.d. Ges.d.Wiss.zu Gottingen, 235 (1918).

[3] C. S. Wu, *et al.* , Phys. Rev. **105**, 1413 (1957).

[4] J. H. Christenson, J. W. Cronin, V. L. Fitch and R. Turlay, Phys. Rev. Lett. **13**, 138 (1964).

[5] A. D. Sakharov, Sov. Phys. Usp. **34**, 417 (1991).

[6] M. Kobayashi and T. Maskawa, Prog. Theor. Phys. **49**, 652 (1973).

[7] L. Wolfenstein, Phys. Rev. Lett. **51**, 1945 (1983).

[8] C. Gay, Ann. Rev. Nucl. Part. Sci. **50**, 577 (2000)

[9] S. Eidelman *et al.* [Particle Data Group], Phys. Lett. B **592**, 1 (2004).

[10] K. Abe *et al.* [Belle Collaboration], Phys. Rev. Lett. **87**, 091802 (2001)

[11] B. Aubert *et al.* [*BABAR* collaboration], Phys. Rev. Lett. **88**, 221803 (2002)

[12] E. J. Williams, Proc. Roy. Soc. A **169**, 531 (1939)

[13] E. J. Williams, Phys. Rev. **58**, 292 (1940)

[14] G. Moliere, Z. Naturforsch. **3a**, 78 (1948)

[15] H. A. Bethe, Phys. Rev. **89**, 1256 (1953)

[16] R. Brun, *et al.* , CERN-DD-78-2-REV

[17] S. Agostinelli *et al.* [GEANT4 Collaboration], Nucl. Instrum. Meth. A **506**, 250 (2003).

[18] H. W. Lewis, Phys.Rev. **78**, 526 (1950)

[19] H. J. Bhabha, Proc. Roy. Soc. **A154**, 195 (1936)

[20] D. Binosi and L. Theussl, Comput. Phys. Commun. **161**, 76 (2004)

[21] S. Jadach, W. Placzek and B. Ward, Phys. Lett. B **390**, 298 (1997)

[22] Y. Kubota *et al.* [CLEO Collaboration], Nucl. Instrum. Meth. A **320**, 66 (1992).

[23] B. Aubert *et al.* [*BABAR* Collaboration], Nucl. Instrum. Meth. A **479**, 1 (2002)

[24] R. Santonico and R. Cardarelli, Nucl. Instrum. Meth. **187**, 377 (1981).

[25] G. Battistoni *et al.* Nucl. Instrum. Meth. **164**, 57 (1979).